BIPEDAL IMPACT WITH GRANULAR MATTER

by

Eliza A. Banu

A dissertation submitted to the Graduate Faculty of
Auburn University
in partial fulfillment of the
requirements for the Degree of
Doctor of Philosophy

Auburn, Alabama
December 13, 2014

Keywords: impact, granular matter, human

Approved by

Dan B. Marghitu, Chair, Professor, Mechanical Engineering, Auburn University
P.K. Raju, Co-Chair, Thomas Walter Distinguished Professor, Mechanical Engineering, Auburn University
Robert L. Jackson, Associate Professor, Mechanical Engineering, Auburn University
Amnon J. Meir, Professor, Mathematics, Auburn University
Ram Gudavalli, Professor, Associate Professor, Director of Biomechanics Core, Palmer Center for Chiropractic Research
Alexandru Morega, Professor, MMAE, Electrical Engineering, University Politehnica of Bucharest
George Flowers, Dean, Graduate School

Abstract

Impact with granular matter has been of great interest to researchers for decades, mainly because the material, as a conglomeration of discrete solids, behaves as a fluid until a solid like behavior becomes established. As a result, a resistance force that would account for these characteristics during impact has been difficult to model. For this study, the resistance force is modeled as a linear superposition of a static (depth-dependent) resistance force and a dynamic (velocity-dependent) frictional force. Impact is defined from the moment the end point of the system comes in contact with the granular matter surface until the moment when the vertical linear velocity of the end point is zero. The variables of interest are the final depth at the end of the penetration phase and the stopping time. The results for two experimental designs: a free round-ended link and a two-link kinematic chain with two points of contact were compared to the results obtained by applying the resistance force formulation developed to corresponding CAD simulation models. The simulation and experimental results revealed that the final displacement increases with initial velocity, while the stopping time decreases for all models. The sensitivity to impact angle and initial velocity were studied and as a result an improvement to the resistance force was formulated. A series of expressions are proposed for the resistance force coefficients to test the dependency of the impact of the free round-ended link on the initial conditions, specifically impact angle and initial velocity. The resistance force and its components were studied as they reacted during impact. The outcomes of this study have a potentially great significance in robotic design, military applications, and prosthetics.

Acknowledgments

My graduate program has definitely been an adventure. There are many people in my life that have made it an experience and an amazing journey that I will never forget.

First and foremost, I would like to express my deepest gratitude to my major advisor Dr. Dan Marghitu for his guidance, caring nature and patience during the course of my doctoral program. I am extremely grateful to him for his trust in allowing me to play a full role in his research activities. I would especially like to thank both him and Dr. Daniela Marghitu for being there when life got hard with falling off horses and surgery or me just being stubborn.

To the co-advisor in my graduate program, Dr. P.K. Raju, I have no words to say thank you for all the support, encouragement, and invaluable guidance he has provided, as well as for his wisdom and for believing in me. I would also like to say a huge thank you for allowing me to join the LITEE (Laboratory for Innovative Technology and Engineering Education) team. It was during this time that I learned how my passion for teaching can be expressed not only in the classroom, but through engineering education research as well. It has been an honor, sir!

I also want to thank Dr. Robert Jackson and Dr. Amnon Meir for the valuable knowledge I gained in their classrooms that has been immensely useful throughout this research. I loved every moment in their classes. I would also like to thank Dr. Ram Gudavalli for his support, to both him and National University of Health Sciences for loaning the OPTOTRAK motion system used in this research. I particularly wish to acknowledge and express my immense gratitude to Dr. Alexandru Morega for his trust in my abilities, when I didn't know I had them. Thank you all for serving on my committee, and for your support. I would also like to thank Dr. Cheryl Seals for serving as the outside reader on my committee.

I would like to express my gratitude to Dr. Nels Madsen for graciously permitting me to use the motion capture lab and set-up for experiments with humans, and Joseph McIntyre for helping with the equipment every time I got stuck. I would also like to thank Dr. Joe Ragan for his invaluable input regarding the SolidWorks models. This research would not have been possible without the

friends who volunteered to participate as subjects in experiments: Cristian Cira, Shahadat Hussain, Yang Xu, Mike Wang, Ozdes Cermik, and Pramod Rajan. To Pramod I would also like to say thank you for his amazing friendship during the last eight years. The office would have been boring and lonely without you! To my beautiful friend and study partner Safina Hussain I would like to thank for her invaluable friendship, support and encouragement.

I would also like to thank my parents Adrian and Cornelia Banu and my brother Dorin Banu for their unconditional support, prayers, love, scolding and encouragement, without which this work would not have been completed. I love you all! Many thanks to my extended family on the North American continent: Laurentiu and Claudia Banu, Petrus and Emilia Pindic, Paul and Simona Banu, Alina and Todd Oldham, Persida and Josh Farkas, and Beti Pindic. They helped me and provided all kind of support and love during my graduate program and for that I am immensely grateful.

I am also grateful for my friends: Heather Donaldson, Betsy and Drew Carlisle, Jill and Brock Armstrong, Donna Layton, Jordan Roberts, Josiah Roberts, Danielle Hudson, Joy Weiman, Eloise Dabbs and Kristina Bruno who infected me with the Auburn spirit, helped making Auburn my home, introduced me to Auburn football and accepted me, so the frustrating moments of graduate school were forgotten with their support, prayers and laughter. Particularly I am immensely grateful for my roommate Kristina Bruno who was there for me through thick and thin and always found creative ways to encourage me, make sure I was safe and so I was able to finish writing my dissertation. I am also so grateful for the many prayers, the support and understanding of my Sunday School Class: Cindy and Jim Wilkerson, Marion Hocutt, Daniel Williams, Josh Barnett, Eric Dooley, Charles and Mackie Woosley.

Finally I would like to give thanks to my Best friend, my Confident, my Inspiration for life, my Helper, my Strength, my Rock, my King, my Savior, the Lover of my heart, Jesus Christ for His grace, for fulfilling His promises and being faithful even when I wasn't.

Table of Contents

List of Figures

List of Tables

Chapter 1

Introduction

The dynamics associated with the motion and interaction of rigid bodies with Newtonian fluids is a classical problem in fluid mechanics. In recent years, however, non-Newtonian fluids and the dynamics of the interaction of an object with such fluids have captured the attention of researchers. Granular media in particular stand out due to their poorly understood dynamics and static behavior. Granular materials are collections of polydisperse grains and exhibit complex fluid behaviors. This means that the rheology of the medium is comparable to that of a solid under a critical shear stress, although it performs like a fluid above it. Granular materials have been studied for potential applications in multiple areas. In earth science, for example, problems such as avalanches involve the flow of granular matter [12, 13, 43] and a better understanding of their behavior would greatly facilitate those seeking to model the effects of earthquakes [38], meteorite impact cratering and low-speed impact cratering [28, 49, 50]. Industrial processes such as mixing, stirring and drilling would also benefit [22, 23], as would biologists studying animal locomotion in sand [33, 35, 37, 39] and the associated biomechanical studies related to the design of robots [33, 34, 48] that can travel on granular ground. For human locomotion alone, granular matter studies are contributing to numerous applications in sport, robots, prosthetics and the formation of footprints.

To appreciate the larger perspective that is involved in these applications, the impact of an object with granular matter is being explored through experiment, simulation and theory. However because of the solid-fluid like behavior of the granular matter, a great deal remains to be explored, especially from a theoretical perspective. The focus of much of the current research on the impact of a rigid body on granular matter is on describing the force experienced due to the reorganization of the grains that are opposing the motion of the intruder. A good understanding of these forces can aid in the design of tools and the design and control of robots designed to maneuver in granular environments. Due to the lack of a universal accepted theoretical model, experiments have generally

sought to demonstrate the variation of the drag force in terms of a number of different parameters: impact velocity [2], the diameter of the penetrating object [12, 13, 2], the packing volume [6], and the shape [7] of the penetrating object, for example cylinders [2, 11, 22, 35, 36] or spheres [24, 20, 38, 42]. Others have adopted a slightly different approach by performing their analysis using discrete element methods (DEM) for the same purpose [12, 13, 21, 52].

The penetration of granular matter at high speeds and low speeds has been studied in recent years [4, 20, 25, 49, 50]. In particular, studies of impact cratering have looked at parameters such as the depth and size of the crater, as well as how the form of the crater is affected by the initial impact conditions of the impacting rigid body. To study the motion of a sphere through granular matter resistance force models were created that treated the problem as the sum of a velocity dependent force and a static resistance force which is depth dependent [49]. For example, Ambroso *et al.* [4] suggested that the stopping time of a projectile in granular matter depends on the geometry and density of the rigid body, and the initial impact velocity.

Lee and Marghitu [29] extended the work of Katsuragi and Durian [28] to provide the first mathematical model for an oblique impact. They demonstrated that for an oblique impact of a compound pendulum the stopping time in the granular matter increases with decreasing initial impact velocity using a force model that consists of a linear superposition of the static resistance force and drag force. Their results are consistent for a two link chain [31], which indicates that the time it takes for a rigid body to come to rest in a granular medium becomes shorter as the impact forces increase.

The earliest study of the characteristics of the interaction of humans with granular matter was in 1972, when Soule and Goldman [44] studied how much energy was lost when humans carried loads on different types of terrain, including loose sand. They showed that the energy cost depends on a terrain factor, and that the value of this factor was highest for sand. Twenty years later, Zamparo *et al.*, [54] compared the energy cost of locomotion in terms of the oxygen uptake during running and walking on a sandy beach versus that required on a firm surface.

The work of Lejeune *et al.* [32] is widely cited by those working on the mechanics and energetics of human locomotion in sand. Through a series of experiments, these authors showed that because of the work done by the foot on sand and the resulting decrease in the muscle-tendon efficiency, there is a higher metabolic cost. Compared to the total work done while walking on sand, the

work done on sand itself is the greatest contributor to the total work done, easily surpassing the sum of the work done by the center of mass and the internal work. However, while running on sand, which represents the case of a bouncing mechanism, the work consists almost entirely of the work done on sand. Similar results have been reported more recently [19] by analyzing sprinting on sand. Though higher energy is dissipated in a granular matter environment than on other surfaces, maximum speed is not acquired but smaller impact shocks are registered. This result is significant from the point of view of training or injury prevention or rehabilitation, when higher efficiency is required but is preferably accompanied with less stress on the musculoskeletal system [3, 26, 27].

Ferris and Farley [14] determined that the total stiffness of the leg and the surface for human hopping is the same regardless of the stiffness of the surface, suggesting that there is some adjustment in leg stiffness to compensate for the surface stiffness. In 1998 Ferris *et al.* come to the same conclusion in the case of human running. Humans adjust their leg stiffness rapidly and smoothly if the transition is expected while running when there is a transition in surface stiffness [15]. These experiments also showed that the entire sole of the runner's shoe was in contact with the surface when the center of mass was at its lowest position, even though the center of pressure is usually under the head area of the metatarsal bones.

The center of mass of the human body does not change its trajectory with time in the case of a runner on sand [15] or a human hopping on the same surface [40]. This behavior is attributed to the mechanics of the leg-surface combination, which acts as a controlled spring-like mechanism. Moritz and Farley [40] used a damping force that was solely velocity dependent.

Looking at the energy expenditure, Muramatsu *et al.* found [41] that it is higher when jumping on sand than on a firm surface. The experimental outcomes for energy cost in terms of oxygen uptake is comparable to those reported in previous studies [32, 54] for running, indicating that jumping on sand is similar to running in this regard.

D'Aout *et al.* studied a footprint generated by a human while walking in sand [9], demonstrating quantitatively that the depth of a footprint does not depend on the mass of the body. During their experiments, the authors noticed that the knee flexes more while walking in sand than on hard ground, which supports the findings of previous research [40, 3] that concluded that when running/walking on sand, the subject has to adjust his or her technique. The depth of the footprint

indentation created by the fifth metatarsal head can be correlated with the velocity, but the depth of the heel depends largely on the pressure in the heel region [9].

In all these studies of human locomotion on sand, the nature of the contact force between the granular matter and the bipedal foot was not analytically addressed. Instead, the force was measured experimentally using a force plate [14].

Tsakiris *et al.* [48] advanced our understanding of undulatory motion as a result of their study of the rowing-like action of the lateral appendages of segmented marine worms in a terrestrial environment. Of the three available models (viscous damping, Coulomb model, and fluid drag model), the authors chose to use the Coulomb model as this depends only on the direction of the velocity and applied it to each individual segment of the polychaete. From experiments using a polychaete-like robotic prototype, the authors were able to extract values for the dynamic coefficient of friction. In a later study by other researchers, the results of their analysis of the data collected on the leg motion of a running zebra-tailed lizard [35] indicated that substantially more energy was lost during locomotion on granular matter, with the lizard displaying a spring-mass-like center of mass kinematics.

Maladen *et al.* [37] developed an empirical model to describe the forces on undulatory swimming animals in dense granular beds. In their simulations, the organism was approximated with a stainless steel cylindrical rod. The authors consider a "frictional fluid" in which the thrust and drag forces are given by the grain-grain flow and grain-body friction. The force was expressed in terms of the length l and radius r of the segment, its angle ψ with the velocity vector and drag material constants C_s, C_F. The normal component is $F_N = 2\,l\,r\,(C_s \sin\beta_0 + C_F \sin\psi)$, and the lateral force $F_L = 2\,l\,r\,C_F \sin\psi$. However, the normal force registered a difference that was not well approximated by the sine function; it increased faster with an angle ψ smaller than 30^o.

Because of the solidification properties of granular matter during various phases of a stance, some aspects of an organism's locomotion on sand can be comparable to that on solid surface [39]. The yield stress of the sand surface is given by the first maximum in the drag force and depends on the square of the penetration depth and linearly with the velocity of the flipper of the turtle. For an inertial force smaller than the yield stress, there is some solidification of the material at each stoke and a thrust force is generated.

These conclusions and results obtained by implementing a model based on the legged locomotion of a zebra-tailed lizard [35, 36] to a C-legged robot [33, 53] underline the importance of having a good analytical expression for the drag force in the granular medium for impacting objects, animal locomotion and human locomotion on granular matter. The new insights expected as a result of this study will provide valuable information that can be applied to future research designed to improve outcomes in applications such as sports (gymnastics landing, long jumps), training, injury recovery, prosthetics, and new robotics developments.

To the best of our knowledge the contact force incurred during the impact of a bipedal mammal with granular matter has not previously been studied. However extensive studies (both simulation and experiments) have been done on jumping [45], hopping, walking and running on hard surfaces. Until now there has been no analytical expression of the contact force between bipedal motion and granular matter. This study will develop an expression for such a force using as its foundation an analytical expression developed for the impact of rigid bodies with granular matter [29, 31] and compare the analytical results with those obtained experimentally.

Chapter 2

Problem Statement

2.1 Purpose of the Study

The focus of this study is on the oblique impact of rigid bodies and human impact with granular matter. The research outlined in the introductory chapter shows that the study of the impact of rigid bodies with granular matter is potentially of great significance. As yet, to the best of our knowledge there has been no comprehensive universally accepted expression for the penetration resistive force of a rigid projectile into a granular medium. The most important aspect of this analysis is therefore to develop an analytical expression for the resistant force that is valid for low-speed impact both vertical and at an angle. Researchers have analyzed the impact of spherical and cylindrical shaped rigid bodies through experiments and numerical simulation. It was concluded that the drag force [20] should include a quadratic velocity dependent term [28, 49], is depended on the depth of penetration [2, 7, 22, 39, 42, 43]. Research has also shown that the resistant force and depth of penetration for plunging rigid bodies into granular matter depend on other parameters as well. The resistant force during impact scales with impact velocity [20], diameter of the impacting object [1, 2, 43], and packing fraction [6, 43, 51]. Only a few studies have been reported for oblique angle impact [29], but have shown that the impact angle has an influence on the value of the resistant force [11, 13, 30, 33, 35, 52].

The first mathematical model for the impact of an object with granular matter at a specific angle was proposed by Lee and Marghitu [29] based on the force model proposed by Tsimring and Volfson [49], and verified experimentally for a sphere by Katsuragi and Durian [28]. The resistance force proposed, takes into account both the rate-dependent force (dynamic frictional force) and the displacement dependent force (static resistance force).

$$\mathbf{F}_r = \mathbf{F}_d(v) + \mathbf{F}_s(y) \tag{2.1}$$

The dynamic force $F_d(v)$ is due to the velocity of the intruder in the granular matter, which is made possible by the fluid-like characteristics of the material, up to the point at which the granular material begins to act like a solid surrounding the object, stopping its motion. Hence, the expression for this can take the same form as that for the drag force: $F_d = bv$. However, it has been shown that the rate-dependent force is proportional to the velocity squared [2, 51]: $F_d = 0.5\rho A C_d v^2$, where ρ is the density of the medium, A is the reference area, and C_d is the drag coefficient. Consequently, the dynamic force used in this work is:

$$\mathbf{F}_d = -\frac{\mathbf{v}}{|\mathbf{v}|}\,\eta_d\,A_r\,\rho_g\,\mathbf{v}\cdot\mathbf{v} \tag{2.2}$$

The force is opposing the motion of the penetrating body, therefore the force expression includes the term $-\frac{\mathbf{v}}{|\mathbf{v}|}$. The term η_d is a constant and A_r is the reference area.

The static force, F_s in Eq. (2.1) represents the force that appears due to the hydrostatic pressure [6] and is based primarily on the reorganization of the particles of matter and grain friction. Thus, this force depends on the material properties, the packing of the matter [21, 43, 51], gravitation and size and shape of the penetrating object. This will tend to lead to the stress increasing with depth according to the scaling factor in one direction, and according to a power law for depth in another direction.

The horizontal static force increases with the granular pressure [1, 2, 12, 24] that is acting on the surface of the body in the horizontal direction. From experiments conducted [2] at very low speeds of $v_0 < 5$ mm/s, the yield force is of the form $F = \eta g \rho H^2 d_c$ where η is a constant that depends on the media properties, g is the gravitation acceleration, H is the immersed dimension of the intruder and d_c is the diameter of the object. For the purposes of this study, the direction in which the force acts will be given by the ratio $-\frac{v_h}{|v_h|}$ and the immersed length of the rigid body is given by the displacement in the granular matter of the tip of the cylinder, d_{yT}. Therefore the generalized horizontal static force is

$$\mathbf{F}_{sh} = -\frac{\mathbf{v}_h}{|\mathbf{v}_h|}\,\eta_h\,g\,\rho_g\,d_c\,d_{yT}^2, \tag{2.3}$$

The vertical component of the static force is the resistant force of the granular medium to the immersion of the intruder in the vertical direction. Experiments conducted for vertical impact

[24, 38, 42] revealed a nonlinear dependency of the force on the depth of penetration and attempted to formulate a power law to describe this force. The power law form was proven to arise due to the dispersed quality of the grain size of the granular matter found in nature, so that the force chain structure between the grains and the grain-intruder exhibits a homogenous distribution. Thus, the expression for the vertical static force is

$$\mathbf{F}_{sv} = -\frac{\mathbf{v}_v}{|\mathbf{v}_v|}\,\eta_v\,(d_{yT}/L)^{\lambda}\,g\,\rho_g\,V, \tag{2.4}$$

where L is the length of the rigid body, $\mathbf{v}_v$ is the vertical term of the velocity of the center of mass of the immersed volume (V) and, as in the previous two cases, the ratio $-\frac{\mathbf{v}_v}{|\mathbf{v}_v|}$ shows how the force acts in the opposite direction to the motion.

The constants η_v and λ depend on the shape of the body, the container the medium, the volume fraction of the granular matter, and the direction of motion of the penetrating object, i.e. whether it is plunging in or withdrawing. These constants are expressed based on empirical data. These experiments [24, 38, 42] focused specifically on the vertical impact of spheres at low speed $v_0 \leq 5$ mm/s, but it is also important that the medium used for the experiments in all three studies consisted of monodisperse glass beads. The recent work of Li *et al.* [36] has shown that the grain type has a considerable influence on the error obtained for their model. For natural sand, they observed an error that was 11% higher than the results obtained in glass beads.

The power law coefficient has been shown to be independent of both the impact speed and diameter of the intruder, but it does depend on grain size and container size, and hence the density of the medium [38]. For a cylinder intruder, λ is smaller than 1.3 under the conditions described above for the plunging motion and greater than 1.7 for withdrawal [24, 42]. The work of Bruyn *et al.* [6] has shown a clear dependency of the power law on grain size, and found values for the power λ that are less than 1. The scaling coefficient for the vertical static force was measured [24] to be approximatively 10 for plunging and 0.5 for withdrawing motion, but other studies that used cylinders as probes for impacting a granular medium consisting of glass spheres [7] found the coefficient η_h to be as high as 70, while Albert *et al.* [1] recorded values as low as 2.43 for cylinders of diameter up to 11.9 mm. For the scaling of a drag force similar to the static vertical resistant force, Constantino *et al.* [8] observed a value for η_h of approximatively 2.7.

In the recent work of Wang *et al.* [52], which utilized a force similar to the one used in this study, the authors concluded that all the scaling factors involved in the expression of the resistant force depend primarily on the angle of impact. Analyses of the dependency of the resistant force exerted by granular media onto a penetrating rigid body on the impact angle [33, 52] has clearly demonstrated the existence of a critical angle. However, for low impact angles the total resistance force involved in an impact with granular matter presents more complicated features.

The purpose of this study is therefore two fold. The first objective is to examine all the characteristics of the resistance force presented above to develop a model that takes into account the influence of the impact angle and the granular properties of the medium when computing of the coefficients η_d, η_h, η_v and λ. Until now, these coefficients have been determined experimentally. A series of mathematical expressions will be proposed for each of these coefficients and then validated by comparing the simulation results for depth and stopping time for single and double impact points at different angles with the experimental results. The second objective for this study is to verify the expression for the resistance force shown in Eq. (2.1) to describe the impact of human feet with granular matter in free fall. To the best of our knowledge such an expression has not previously been proposed. The experimental results will be compared with the simulation results for depth of impact and stopping time to develop a new approach to simulating impact with granular matter. Based on an extensive review of the literature in this field, this study is the first to use a computer-aided design software package (SolidWorks 2014) that includes motion analysis capabilities.

2.2 Organization of the Study

This study is organized by the type of impact. Chapter three discusses the impact of a free round-ended rigid body with granular matter, and the analytical expressions proposed for the non-dimensional coefficients η_d, η_h, η_v and λ presented. The simulation model and results are observed and compared to the experimental results. It is expected that applying these expressions will produce a force that is decreasing with the angle. The force values will be extracted from the simulation results. Chapter four presents the simulation and experimental results for an impact with two contact points with the granular matter. New expressions for the coefficients are developed

and used for the simulation model in SolidWorks and the results obtained are compared to the experimental results. Chapter five addresses the impact of a human lower body with granular material. The same simulation software is employed and the forces used to simulate the contact are the static and dynamic resistance forces described above. The simulation results for depth and stopping time are then compared to the experimental results for the same variables. Chapter six outlines the conclusions of this study.

2.3 Significance of the Study

This study is of great importance on multiple fronts. First, a set of mathematical expressions for estimating the values of the scaling that should be used is proposed for each component of the resistance force. In this work, a resistance force is proposed for the impact of the human foot with granular matter. Until now, researchers have focused on either the rate-dependent force, by submerging an object in flowing sand, or the depth-dependent component, by performing experiments at very low speeds. The force model presented in this study shows that the two components are not independent of each other and should thus not be treated separately. The depth depends on impact velocity, therefore the static force will be influenced by the dynamic force.

This study also presents a CAD model to be used in simulating the impact of rigid bodies and the human feet with granular matter by using an equation model that will reduce computational time in comparison to other numerical models and discreet element methods. The results of this study will be of particular value in robotic design, prosthetics, sports training, and injury recovery.

Chapter 3

Impact of a Free Rigid Body

This chapter discusses the impact of a free rigid link on a volume of granular matter for several initial conditions. Experimental results regarding the depth of penetration and velocity during impact are presented, as well as simulation results for the same variables. The simulation setup will also provide numerical results for the resistance force during impact. An analysis of the dependency of the depth and stopping time with the angle of impact is also provided.

3.1 Model of the Impact of a Round-Ended Free Link

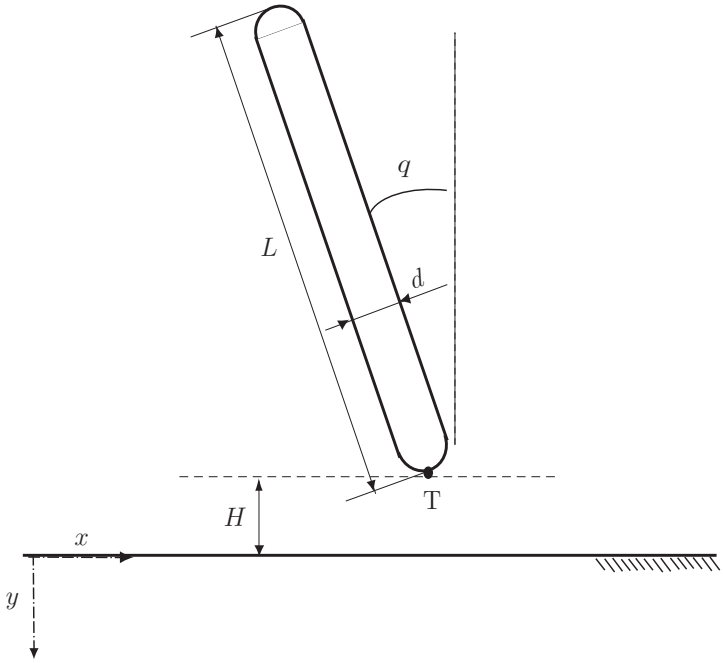

Figure 3.1: Free round-ended link

The motion of a free round-ended cylinder (Fig. 3.1) is considered in 2D (planar motion). A fixed reference frame can be used to describe the planar motion of the model. The origin of the

fixed reference frame is on the surface of the granular bed, and the model will move in the $x\,y$ plane. The impact is constrained to a plane parallel to the vertical plane defined by the x and y axes. The positive y axis is considered downward, and the positive x axis is to the right. The unit vector attached to the Cartesian 2D reference frame is $\mathbf{\imath}_0$ for the x axis and $\mathbf{J}_0$ for y axis. Therefore the yaw (rotation about the y axis) is assumed negligible.

A general representation of the round-ended free cylinder impacting the granular surface is shown in Fig. 3.2. The link is of length L and diameter d. H is the height with respect to which the initial impact velocity $v_0 = \sqrt{2gH}$ is defined according to energy conservation laws. For all the models in this study, the impact is starts when the tip of the bar T contacts the granular surface (v_T is maximum), and ends when the vertical component of the velocity of the point T is zero. The penetration depth, d_{yT} is the distance between the surface of the granular bed and the end tip of the cylinder. The initial conditions are given by the initial impact angle q and initial impact velocity v_0. Angle q is the angle of the bar with the vertical axis y, and $\alpha = \pi/2 - q$.

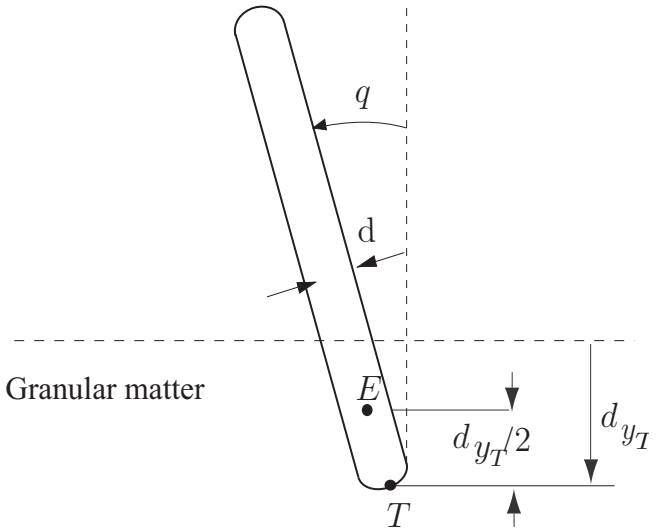

Figure 3.2: Free link penetration notations

3.2 Experimental Results for Round Ended Free Link

3.2.1 Experimental Setup

A round ended bar of length $L = 0.190$ m is considered for the study of impact with granular matter. The steel bar illustrated in Fig. 3.1 has a diameter $d_c = 0.0127$ m and mass $m = 0.184$ kg. The free link is released from rest at height H by relaxing the grab of the CRS A255 Robot (Fig. 3.4). The motion capture system used for this study is the Northern Digital Inc. OPTOTRAK 3020. The system consists of IR markers, a strober, position sensors (IR cameras), a Control Unit and a PC (Fig. 3.4). The OPTOTRAK 3020 can track up to 256 inferred markers connected through the strober to the control unit. The control unit is connected to the position sensors to measure changes in the position of the markers with time. The user has access to the data recorded through the NDI ToolBench software (Appendix A), which also controls the system hardware.

Two infrared markers are attached to the rigid link (Fig. 3.3). Marker M_1 is positioned in the center of mass of the bar, the second marker M_2 is at the top end of the bar and the third marker M_3 is located on the surface of the granular matter. The pipeline in Appendix A extracts the three position components of each marker during the fall, calculates the initial angle of the link, and provides a 3D view of the markers (Appendix B).

The motion capture system in Fig. 3.4 records the position of the markers with a RMS accuracy of 0.1 mm [5] and does not require calibration. The 3D position in time of the two markers attached to the rigid free link is captured during the free fall at a sample rate of 650 frames/s.

The granular medium utilized for the experiments in this study was "Play sand" (Quikrete 1113-51). This kind of sand was chosen over glass beads or monodisperse beads due to its properties being more appropriate for applications involving multi-legged robots that must move across many different types of terrain. Li *et al.* [36] performed tests on dry granular media with various particle sizes and properties. They reported large errors between tests on natural sand and glass beads and poppy seeds. For the purpose of this study, natural polydisperse grains represent the optimum choice. A box of dimensions $0.45 \times 0.32 \times 0.09$ m (L $\times$ W$\times$ H) was filled with the granular matter. The dimensions of the box were sufficiently larger than the intruder to ensure that no Jansen effect would to occur. In order to preserve the integrity of the results for each data collection, the sand

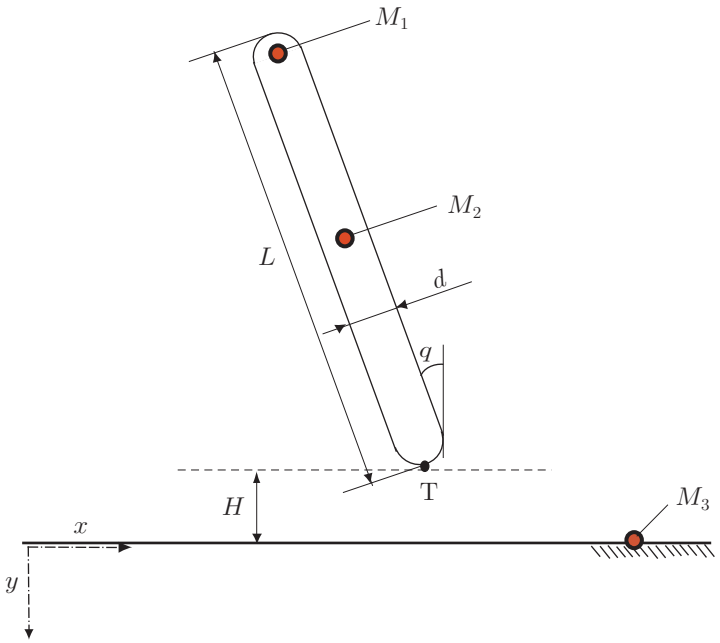

Figure 3.3: Position of the IR markers on the free link during recording

was stirred and leveled before each drop of the rigid free link. This procedure was utilized to maintain volume fraction and eliminate history effects.

3.2.2 Experimental Results

Using the set-up and procedure described in section 3.2.1, the impact with granular matter was inspected under several initial conditions. Two variables were adjusted: impact angle and initial velocity. The impact angle q is defined relative to the upward vertical axis. The initial velocity was defined as the linear velocity of the end of the bar T, v_{yT}. Four cases were considered:

- For $q(0) = 0^o$: $v_{01}(0) = 2.21$ m/s; $v_{02}(0) = 1.82$ m/s; $v_{03}(0) = 1.25$ m/s.
- For $q(0) = 45^o$: $v_{01}(0) = 2.27$ m/s; $v_{02}(0) = 1.88$ m/s; $v_{03}(0) = 1.26$ m/s.
- For $q(0) = 60^o$: $v_{01}(0) = 2.08$ m/s; $v_{02}(0) = 1.52$ m/s; $v_{03}(0) = 0.64$ m/s.
- For $q(0) = 75^o$: $v_{01}(0) = 2.21$ m/s; $v_{02}(0) = 1.74$ m/s; $v_{03}(0) = 1.08$ m/s.

For each case, five recordings were analyzed. The recordings utilized 700 frames/s for $q = 0^o$, 600 frames/s for $q = 45^o$, 650 frames/s for $q = 60^o$ and 650 frames/s for $q = 75^o$, with an expected

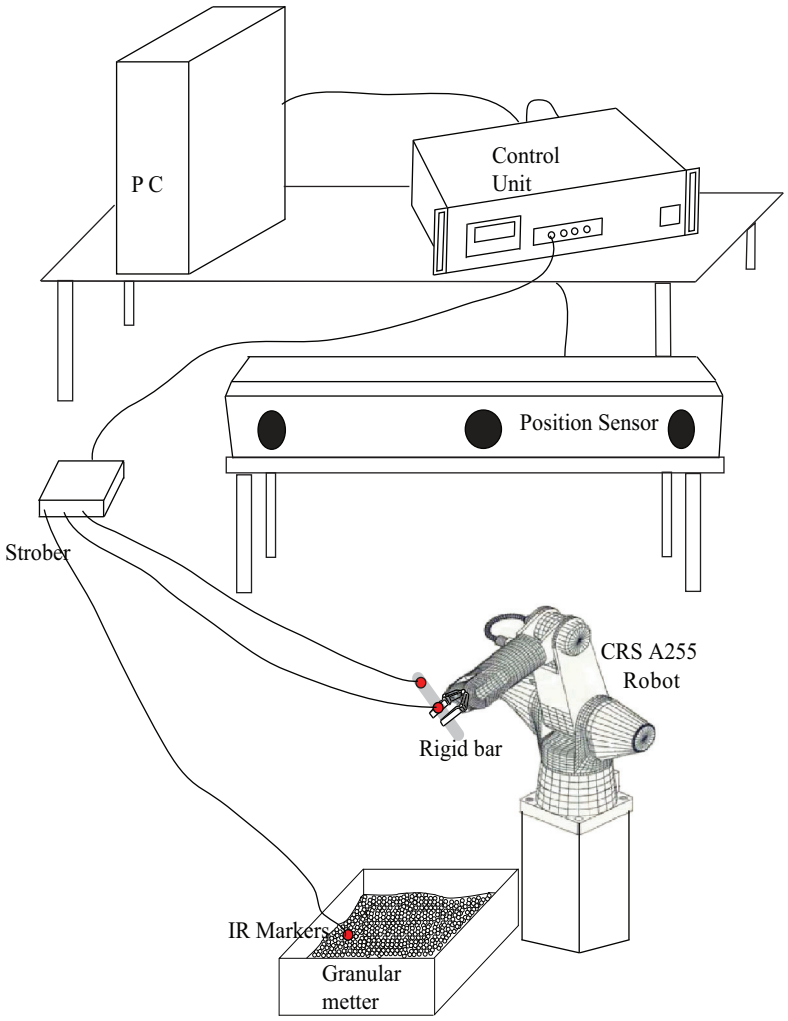

Figure 3.4: Optotrak 3020 experimental set-up for the impact of a free link

	t_s (s)	d_{yT} (m)	v_{yT_0} (m/s)
$q = 0^o$	0.040 ± 0.001	0.051 ± 0.001	2.211 ± 0.021
	0.043 ± 0.002	0.045 ± 0.002	1.817 ± 0.066
	0.047 ± 0.003	0.033 ±0.003	1.244 ± 0.046
$q = 45^o$	0.027 ± 0.004	0.030 ± 0.005	2.270± 0.045
	0.029 ± 0.003	0.026 ± 0.004	1.882 ± 0.043
	0.035 ± 0.002	0.022 ± 0.003	1.264 ± 0.035
$q = 60^o$	0.020 ± 0.001	0.030 ± 0.002	2.080 ± 0.064
	0.022 ± 0.002	0.025 ± 0.002	1.526 ± 0.021
	0.036 ± 0.003	0.021 ± 0.001	0.638 ± 0.034
$q = 75^o$	0.009 ± 0.002	0.015 ± 0.002	2.208 ± 0.024
	0.011 ± 0.001	0.014 ± 0.001	1.737 ± 0.034
	0.017 ± 0.001	0.013 ± 0.001	1.068 ± 0.043

Table 3.1: Experimental results for free round-ended link oblique impact

accuracy of 0.001s. The impact data extracted is the displacement for the end point T of the free link. The impact starts at $d_{yT}(0) = 0$ and the end of the penetration phase is taken to be the time at which the linear vertical velocity of the tip of the bar is zero, $v_{yT}(t) = 0$. The stopping time represents the time it takes the link to burrow into the granular matter volume up to the point when $v_{yT}(t_s) = 0$.

Figures 3.5, 3.7, 3.9 and 3.11 present the experimental average displacement results for impact angles $q(0) = 0^o; q(0) = 45^o; q(0) = 60^o$ and $q(0) = 75^o$ respectively, while Figures 3.6, 3.8, 3.10 and 3.12 present the corresponding experimental results for the decrease in velocity during impact for the same impact angles. The data shows that increasing of the initial impact velocity leads to a decrease in stopping time. This means that for lower impact velocities, it takes longer for the penetrating object to stop moving, even though the distance traveled is shorter. Table 3.1 shows the recorded stopping time, t_s; final displacement, $d_{yT}(t_s)$ for the impact angles; and the initial impact velocities chosen v_{yT_0}, as well as the standard deviation values for the five series of data for each initial velocity.

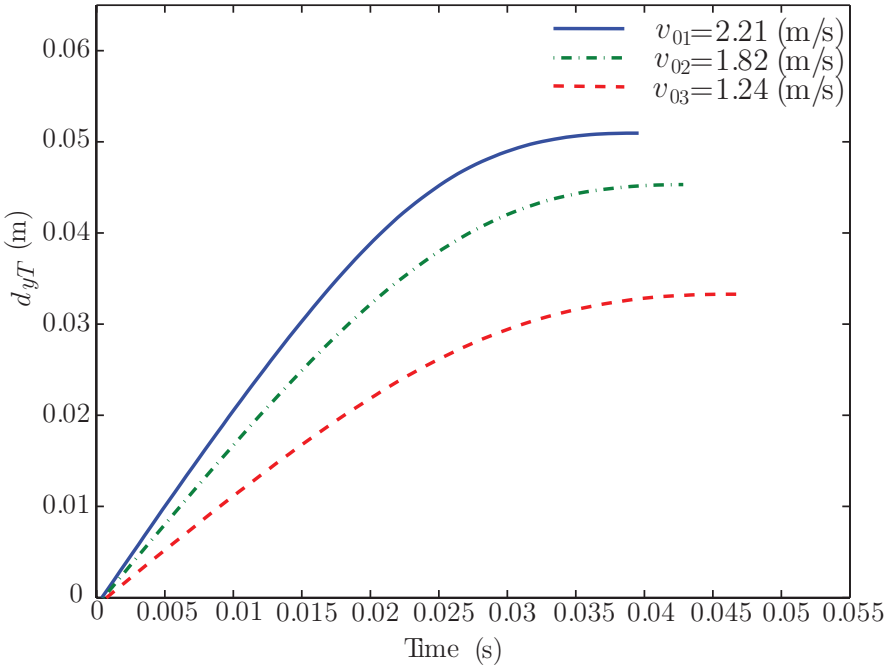

Figure 3.5: Experimental results for displacement for impact at $q = 0^o$

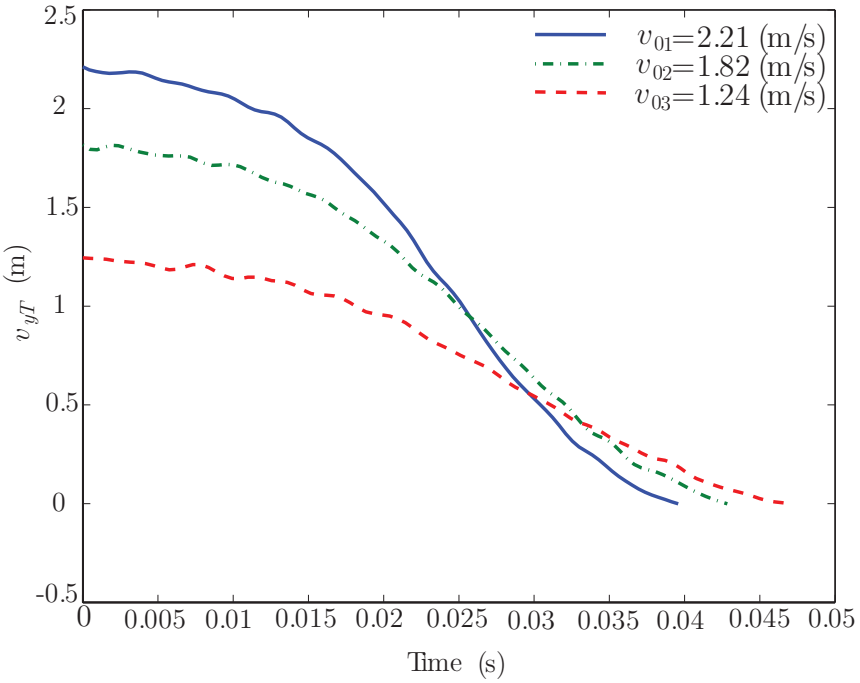

Figure 3.6: Experimental results for velocity for impact at $q = 0^o$

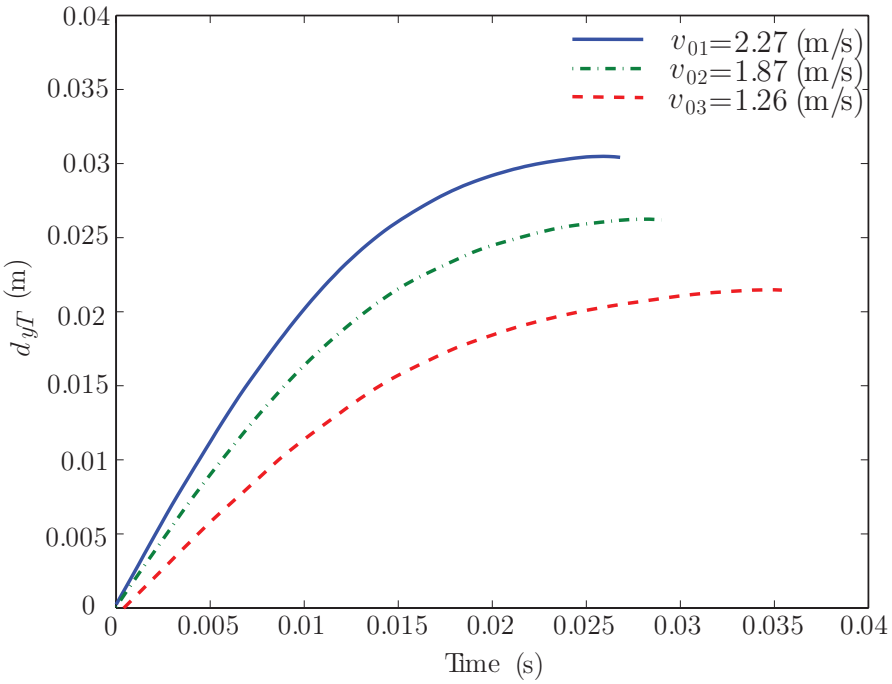

Figure 3.7: Experimental results for displacement for impact at $q = 45^o$

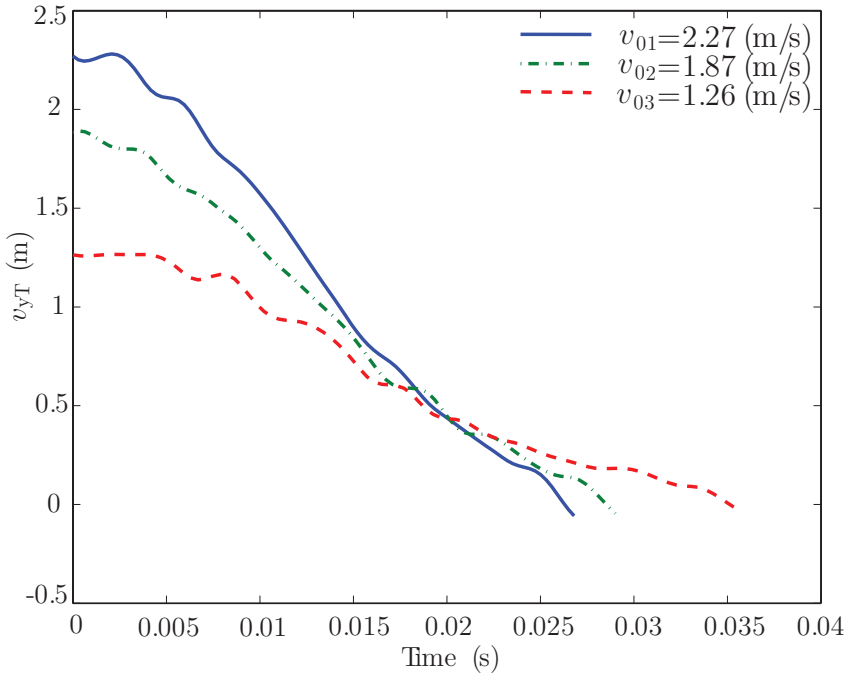

Figure 3.8: Experimental results for velocity for impact at $q = 45^o$

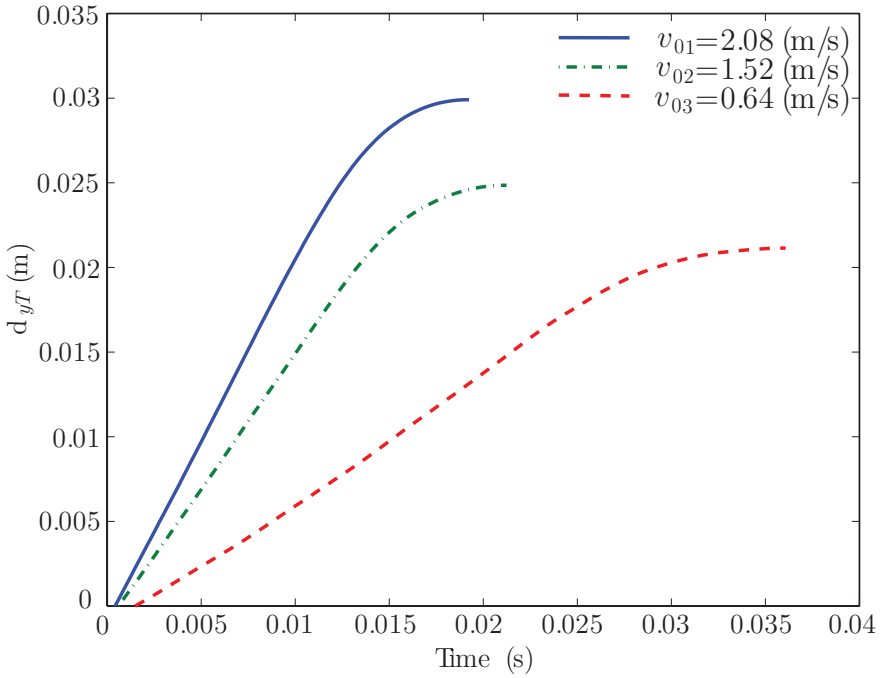

Figure 3.9: Experimental results for displacement for impact at $q = 60^o$

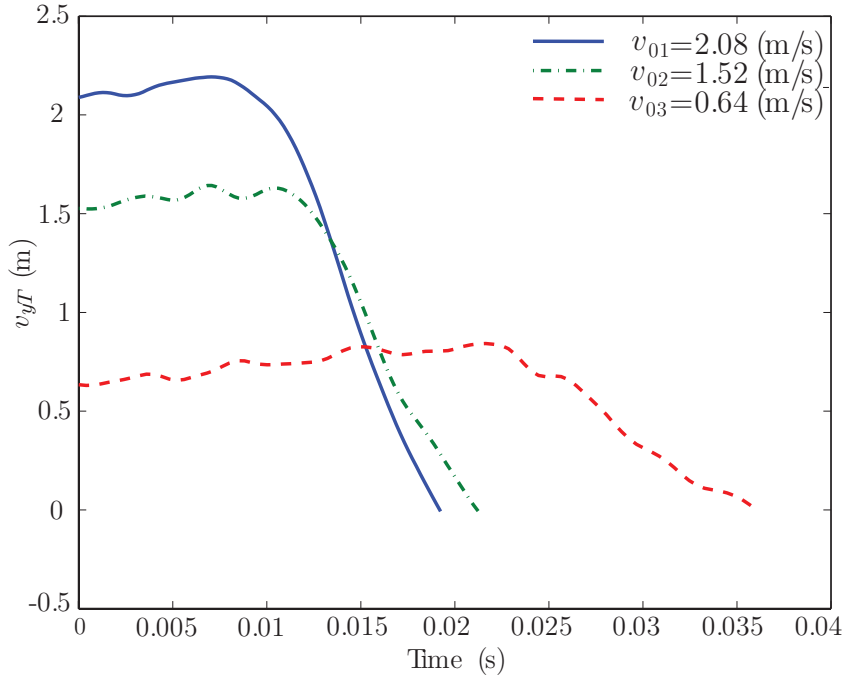

Figure 3.10: Experimental results for velocity for impact at $q = 60^o$

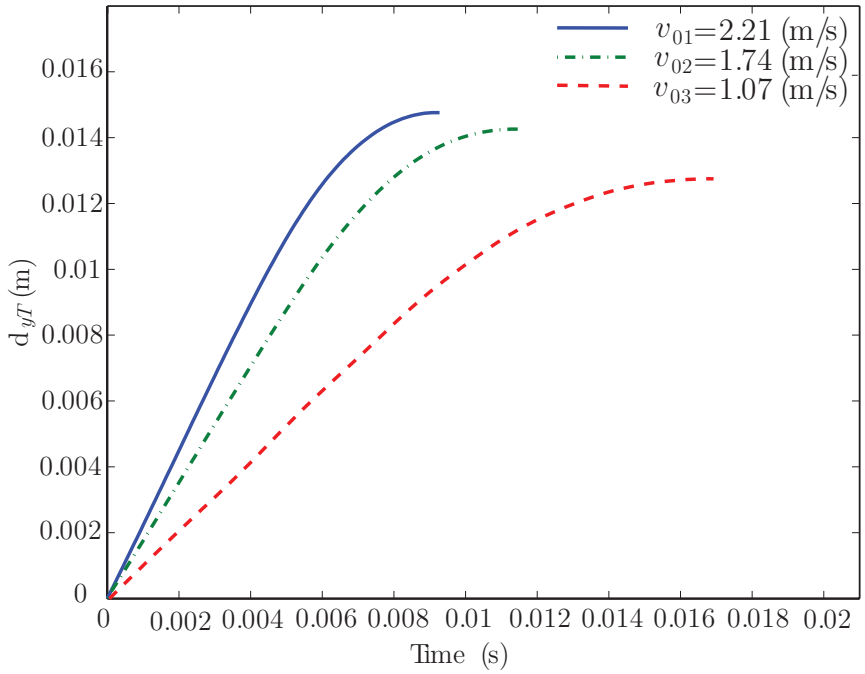

Figure 3.11: Experimental results for displacement for impact at $q = 75^o$

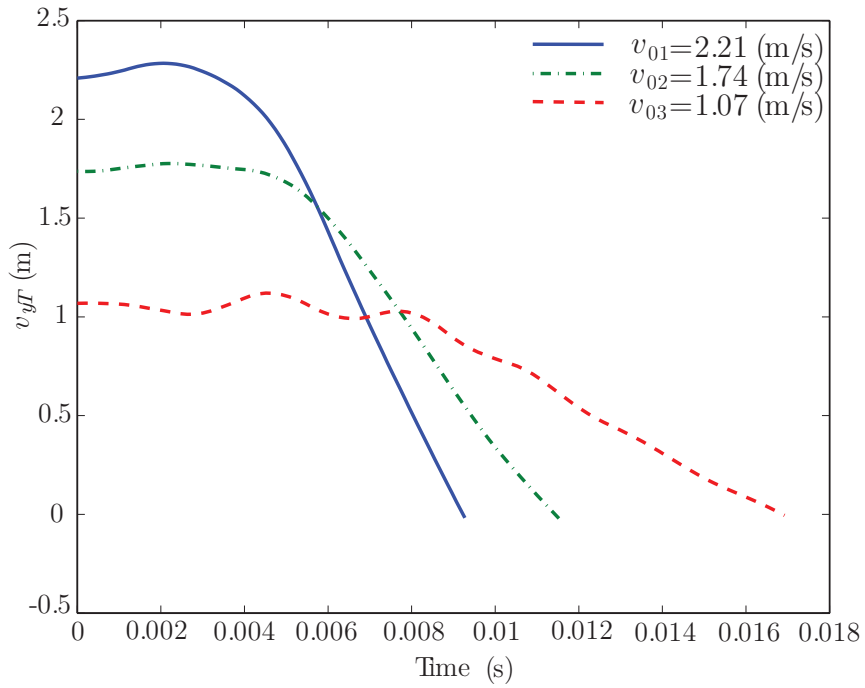

Figure 3.12: Experimental results for velocity for impact at $q = 75^o$

3.3 Simulation of the Impact of a Free Round-Ended Cylinder

3.3.1 Simulation Model

The link described in section 3.1 was modeled in the CAD software package SolidWorks ® 2014 [18] (Fig. 3.13), which incorporates motion study capabilities for accurately simulating and analyzing the effects of different motion components, including forces [17]. SolidWorks was chosen because it allows kinematic analysis with user input force expressions that use real time motion study results.

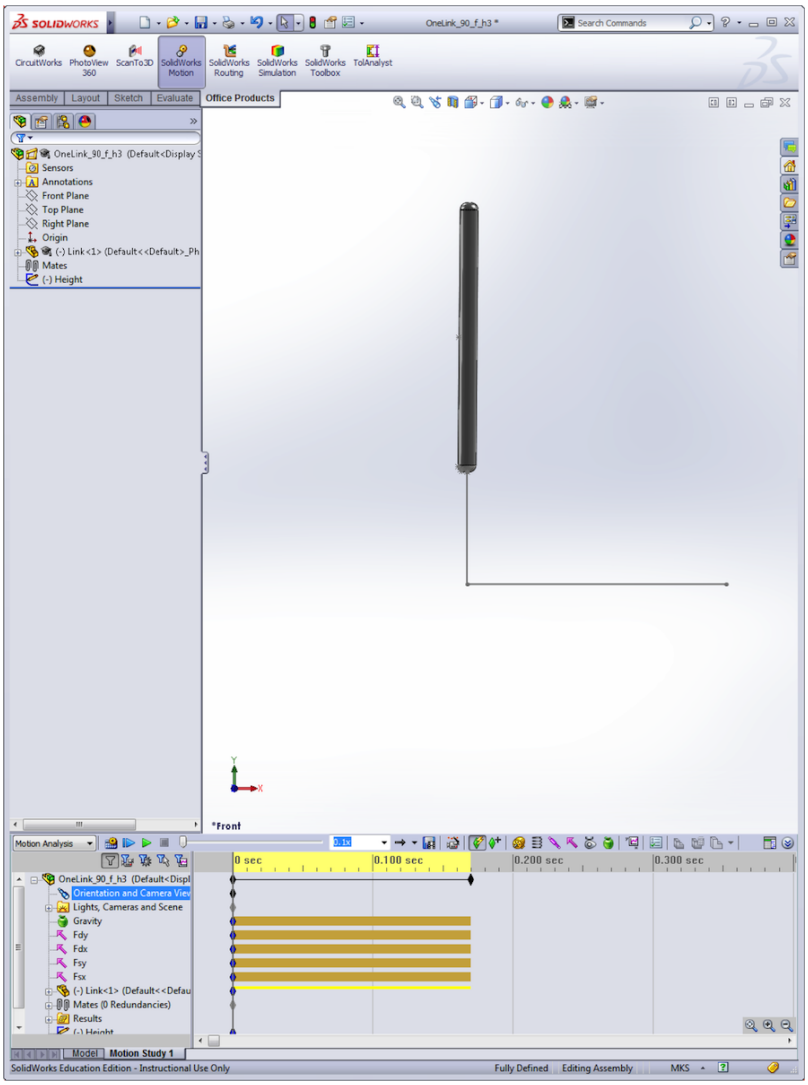

Figure 3.13: The SolidWorks model for the experimental rigid free link

The part modeled in SolidWorks has the same dimensions and material properties as the link used for the experiments. The part is allowed to move in a planar reference frame, with the positive x axis to the right and positive y upward. The results presented in this analysis are the absolute values for displacement and velocity.

The impact with sand (density $\rho_g = 1650$ kg/m^3) was simulated using the mathematical expression for the resistance force described in Chapter 2. For the model proposed, Eqs. 3.23, 2.3, 2.4 can be applied with no restrictions because the dynamic friction force and static resistance force proposed have the same point of application. The point of application is considered to be the centroid of the immersed volume. If the unit vector $\mathbf{u} = \mathbf{\imath} + \mathbf{\jmath}$ is attached to the Cartesian reference frame used, the terms of the resistance force become:

$$\mathbf{F_d} = -\frac{\mathbf{v}_E}{|\mathbf{v}_E|}\,\eta_d\,\rho_g\,A_r\,\mathbf{v}_E\cdot\mathbf{v}_E = -\mathbf{v}_E\,\eta_d\,\rho_g\,A_r\,|\mathbf{v}_E|, \tag{3.1}$$

$$\mathbf{F}_{sh} = -\frac{\mathbf{v}_{E_x}}{|\mathbf{v}_{E_x}|}\,\eta_h\,g\,\rho_g\,d_{yT}^2\,d_c = \left[-\text{sign}(v_{E_x})\,\eta_h\,g\,\rho_g\,d_{yT}^2\,d_c\right]\,\mathbf{\imath}, \tag{3.2}$$

$$\mathbf{F}_{sv} = -\frac{\mathbf{v}_{E_y}}{|\mathbf{v}_{E_y}|}\,\eta_v\,(d_{yT}/L)^\lambda\,g\,\rho_g\,V = \left[-\text{sign}(v_{E_y})\,\eta_v\,(d_{yT}/l)^\lambda\,g\,\rho_g\,V\right]\,\mathbf{\jmath}, \tag{3.3}$$

where L is the lateral dimension of the link, d_c is the diameter, and ρ_g is the density of the granular medium. Because of the proven dependency of the resistance force of the packing fraction of the granular matter, ρ_g is the density of the medium and the packing fraction is factored into the value of ρ_g. Velocity $\mathbf{v}_E$ is the linear velocity vector of the centroid of the immersed volume, with $\mathbf{v}_{E_x}$ being the horizontal component of the velocity $\mathbf{v}_E$ and $\mathbf{v}_{E_y}$ the vertical component of the velocity of the centroid $\mathbf{v}_E$.

The velocity of point E can be expressed in terms of the velocity of the end point T, v_T, angle of impact q and angular velocity of the bar, ω.

$$\mathbf{v}_E = \mathbf{v_T} + \omega \times (\mathbf{r_E} - \mathbf{r_T}), \tag{3.4}$$

where $\mathbf{r}_E$ and $\mathbf{r_T}$ are the position vectors of points E and T.

$$\mathbf{r}_T = d_{y_T}\,\mathbf{J}, \tag{3.5}$$

$$\mathbf{r}_E = \left(\frac{d_{y_T}}{2}\cdot\tan(q)\right)\,\mathbf{\imath} + \frac{d_{y_T}}{2}\,\mathbf{J}. \tag{3.6}$$

Then

$$\mathbf{r}_E - \mathbf{r}_T = \left(\frac{d_{y_T}}{2}\cdot\tan(q)\right)\,\mathbf{\imath} + \frac{d_{y_T}}{2}\mathbf{J} - d_{y_T}\mathbf{J}, \tag{3.7}$$

$$\mathbf{r}_E - \mathbf{r}_T = \frac{d_{y_T}}{2}\cdot\tan(q)\,\mathbf{\imath} - \frac{d_{y_T}}{2}\mathbf{J}. \tag{3.8}$$

Substituting Eq. 3.8 into Eq. 3.4 and with $\omega = \omega\,\mathbf{k}$, the expression for v_E becomes:

$$\mathbf{v}_E = \mathbf{v}_T + \omega\,\mathbf{k}\times\left(\frac{d_{y_T}}{2}\cdot\tan(q)\,\mathbf{\imath} - \frac{d_{y_T}}{2}\,\mathbf{J}\right) \tag{3.9}$$

$$\mathbf{v}_E = \mathbf{v}_T + \frac{d_{y_T}}{2}\,\tan(q)\,\omega\,\mathbf{J} + \frac{d_{y_T}}{2}\,\omega\,\mathbf{\imath}. \tag{3.10}$$

Therefore the expressions for v_{E_x} and v_{E_y} to be used in Eqs. 3.1, 3.2, 3.3 are:

$$v_{E_x} = v_{T_x} + \frac{d_{y_T}}{2}\,\omega, \tag{3.11}$$

$$v_{E_y} = v_{T_y} + \frac{d_{y_T}}{2}\,\tan(q)\,\omega. \tag{3.12}$$

The term A_r in Eq. 3.1 represents the reference area of the rigid body as represented in Fig. 3.14. Because the impact in this model will be express in terms of the impact angle, then the reference area will change as the angle changes during impact. The expression for the reference area is:

$$A_r = d_c\,\frac{d_{yT}}{\cos q}\,|\sin(q - q_m)|\,, \tag{3.13}$$

$$q_m = \tan^{-1}\left(\frac{v_{Ex}}{v_{Ey}}\right), \tag{3.14}$$

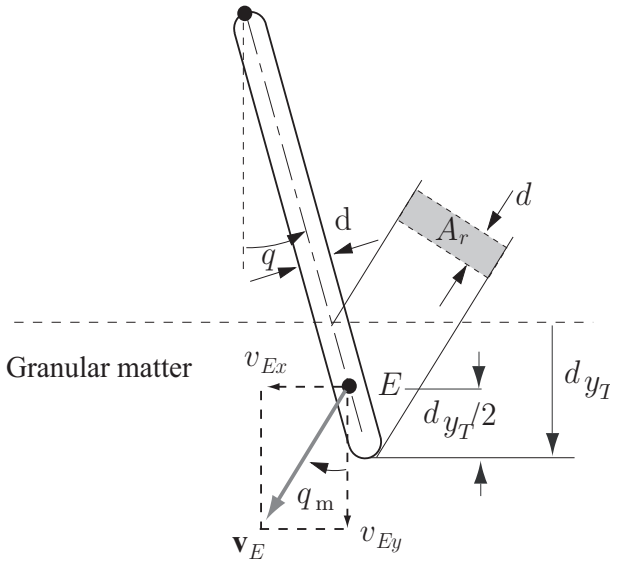

Figure 3.14: The reference area and the physical parameters of the free link

where q is the angle between the cylinder and the vertical axis and q_m is the moving angle (see Fig. 3.14) of the intruder. The volume V of the immersed rigid body can also be calculated in terms of the impact angle:

$$V = \frac{\pi\, {d_c}^2}{4}\,\frac{d_{yT}}{\cos q}. \tag{3.15}$$

Substituting Eqs. 3.1-3.15 into Eq. 2.1 and separating the components of the vectors per their respective unit vector, the resistance force during impact becomes:

$$\begin{aligned}
\mathbf{F}_R &= \mathbf{F}_d + \mathbf{F}_{sh} + \mathbf{F}_{sv} \\
&= \left[-\left(v_{T_x} + \frac{d_{y_T}}{2}\,\omega\right)\,\eta_d\,\rho_g\,d_c\,\frac{d_{yT}}{\cos q}\cdot\left|\sin\left(q - \tan^{-1}\left(\frac{v_{T_x} + \frac{d_{y_T}}{2}\,\omega}{v_{T_y} + \frac{d_{yT}}{2}\,\tan(q)\,\omega}\right)\right)\right|\cdot\right. \\
&\quad \left.\sqrt{\left(v_{T_x} + \frac{d_{y_T}}{2}\,\omega\right)^2 + \left(v_{T_y} + \frac{d_{y_T}}{2}\,\tan(q)\,\omega\right)^2} - \mathrm{sign}(v_{E_x})\,\eta_h\,g\,\rho_g\,d_{yT}^2\,d_c\right]\mathbf{i} + \\
&\quad \left[-\left(v_{T_y} + \frac{d_{y_T}}{2}\,\tan(q)\,\omega\right)\,\eta_d\,\rho_g\,d_c\,\frac{d_{yT}}{\cos q}\cdot\left|\sin\left(q - \tan^{-1}\left(\frac{v_{T_x} + \frac{d_{y_T}}{2}\,\omega}{v_{T_y} + \frac{d_{yT}}{2}\,\tan(q)\,\omega}\right)\right)\right|\cdot\right. \\
&\quad \sqrt{\left(v_{T_x} + \frac{d_{y_T}}{2}\,\omega\right)^2 + \left(v_{T_y} + \frac{d_{y_T}}{2}\,\tan(q)\,\omega\right)^2} - \\
&\quad \left.\mathrm{sign}(v_{E_y})\,\eta_v\,(d_{yT}/L)^{\lambda}\,g\,\rho_g\,\frac{\pi\,{d_c}^2}{4}\,\frac{d_{yT}}{\cos q}\right]\mathbf{j}.
\end{aligned} \tag{3.16}$$

Breaking down Eq. 3.16, the four components of the resistance force are

$$F_{d_x} = -\left(v_{T_x} + \frac{d_{y_T}}{2}\,\omega\right)\,\eta_d\,\rho_g\,d_c\,\frac{d_{yT}}{\cos q}\cdot \left|\sin\left(q - \tan^{-1}\left(\frac{v_{T_x} + \frac{d_{y_T}}{2}\,\omega}{v_{T_y} + \frac{d_{y_T}}{2}\,\tan(q)\,\omega}\right)\right)\right|\cdot \sqrt{\left(v_{T_x} + \frac{d_{y_T}}{2}\,\omega\right)^2 + \left(v_{T_y} + \frac{d_{y_T}}{2}\,\tan(q)\,\omega\right)^2}, \tag{3.17}$$

$$F_{d_y} = -\left(v_{T_y} + \frac{d_{y_T}}{2}\,\tan(q)\,\omega\right)\,\eta_d\,\rho_g\,d_c\,\frac{d_{yT}}{\cos q}\cdot \left|\sin\left(q - \tan^{-1}\left(\frac{v_{T_x} + \frac{d_{y_T}}{2}\,\omega}{v_{T_y} + \frac{d_{y_T}}{2}\,\tan(q)\,\omega}\right)\right)\right|\cdot \sqrt{\left(v_{T_x} + \frac{d_{y_T}}{2}\,\omega\right)^2 + \left(v_{T_y} + \frac{d_{y_T}}{2}\,\tan(q)\,\omega\right)^2}, \tag{3.18}$$

$$F_{s_x} = -\frac{\mathbf{v}_{E_x}}{|\mathbf{v}_{E_x}|}\,\eta_h\,g\,\rho_g\,d_{yT}^2\,d_c, \tag{3.19}$$

$$F_{s_y} = -\frac{\mathbf{v}_{E_y}}{|\mathbf{v}_{E_z}|}\,\eta_v\,(d_{yT}/L)^{\lambda}\,g\,\rho_g\,\frac{\pi\,{d_c}^2}{4}\,\frac{d_{yT}}{\cos q}. \tag{3.20}$$

It is now possible to propose a series of expressions for the impact with granular matter developed empirically, for the scaling constants and power law in the resistance force: η_d, η_h, η_v and λ. The expressions presented in Table 3.2 provide approximate values for the constants that can be implemented in the force model used in the simulations.

The changes in the expressions for the constants for angles of approximatively 30^o are consistent with the phenomena observed in recent impact investigations with respect to the impact angle [12, 33, 36, 52]. Though there is no consensus regarding the exact value for the critical angle (30^o, 15^o), it is generally agreed that at small angles the expressions for the impact forces become more complex. Note that the impact angle q or $\alpha = \pi/2 - q$ used in the expressions in Table 3.2 must be expressed in radians to ensure that the unit measure of the force remains in Newtons.

3.3.2 Comparison of Simulation and Experimental Results

For the free link model designed in SolidWorks, the impact was simulated in Motion Analysis mode. In this model the forces are applied at the contact point of the bar with the horizontal plane. The link is set to free fall so that the forces in Eq. 3.16 are active when $d_{y_T} = 0$ (Appendix C)

Angle $\alpha = \pi/2 - q$	η_h	η_d	η_v	λ
90	$\frac{\rho_g}{\alpha^2 100}$	$\frac{3}{2}\eta_h\,\alpha$	$10\eta_h\alpha^3$	$\frac{\rho_g}{\alpha}\cdot 10^{-4}$
85	$\frac{\rho_g}{\alpha^2 100}$	$\frac{3}{2}\eta_h\,\alpha$	$10\eta_h\alpha^3$	$\frac{\rho_g}{\alpha}\cdot 10^{-4}$
75	$\frac{\rho_g}{\alpha^2 100}$	$\frac{3}{2}\eta_h\,\alpha$	$10\eta_h\alpha^3$	$\frac{\rho_g}{\alpha}\cdot 10^{-4}$
65	$\frac{\rho_g}{\alpha^2 100}$	$\frac{3}{2}\eta_h\,\alpha$	$10\eta_h\alpha^3$	$2\rho_g\,\alpha\cdot 10^{-4}$
55	$\frac{\rho_g\,\alpha^2}{100}$	$\frac{2}{3}\eta_h\,q$	$10\eta_h\,\alpha^3$	$2\rho_g\,\alpha\cdot 10^{-4}$
45	$\frac{\rho_g\,\alpha^2}{100}$	$\frac{2}{3}\eta_h\,q$	$10\eta_h\,\alpha^3$	$2\rho_g\,\alpha\cdot 10^{-4}$
35	$\frac{\rho_g\,\alpha^2}{100}$	$\frac{2}{3}\eta_h\,q$	$10\eta_h\,q^3$	$2\rho_g\,\alpha\cdot 10^{-4}$
25	$\frac{\rho_g\,\alpha^2}{100}$	$\frac{2}{3}\eta_h\,q$	$10\eta_h\,q^3$	$2\rho_g\,\alpha\cdot 10^{-4}$
15	$\frac{\rho_g\,\alpha^2}{10}$	$\frac{2}{3}\eta_h\,\alpha$	$10\eta_h\,q^3$	$2\rho_g\,q\cdot 10^{-4}$
5	$\frac{\rho_g\,\alpha^2}{10}$	$\frac{2}{3}\eta_h\,\alpha$	$10\eta_h\,q^3$	$2\rho_g\,q\cdot 10^{-4}$

Table 3.2: The analytical expressions for the constants η_d, η_h, η_v and λ in the resistance force formulation

and the velocity of the rigid body reaches the initial impact velocity measured in the experiments. Appendix C shows the expressions for the four components (Eq. 3.17 - 3.20) of the resistance force as they were entered in SolidWorks for $q = 0^o$. Similar expressions were used for all cases of different impact angles and initial impact velocity. The difference in these expressions are due to the coefficients η_d, η_h, η_v and λ that are approximated in accordance to Table 3.2 for each angle. The values for these coefficients used in the simulations are given in Table 3.4.

The calculations for the simulations were performed at 10000 frames/s and with 0.0001m accuracy. The gravity acting on y is also turned on for the Motion Analysis. The first step in this study of oblique impact with granular matter was to extract the data for the displacement and velocity at the end point T. Motion Analysis was run for three impact angles, $q = 0^o, q = 45^o$ and $q = 75^o$, at three different initial velocities. The impact angles used for the models in SolidWorks were the same as the impact angles extracted from the experimental data. The colored curves in Figs. 3.15 - 3.20 show the simulation results for penetration depth and velocity with the following initial conditions:

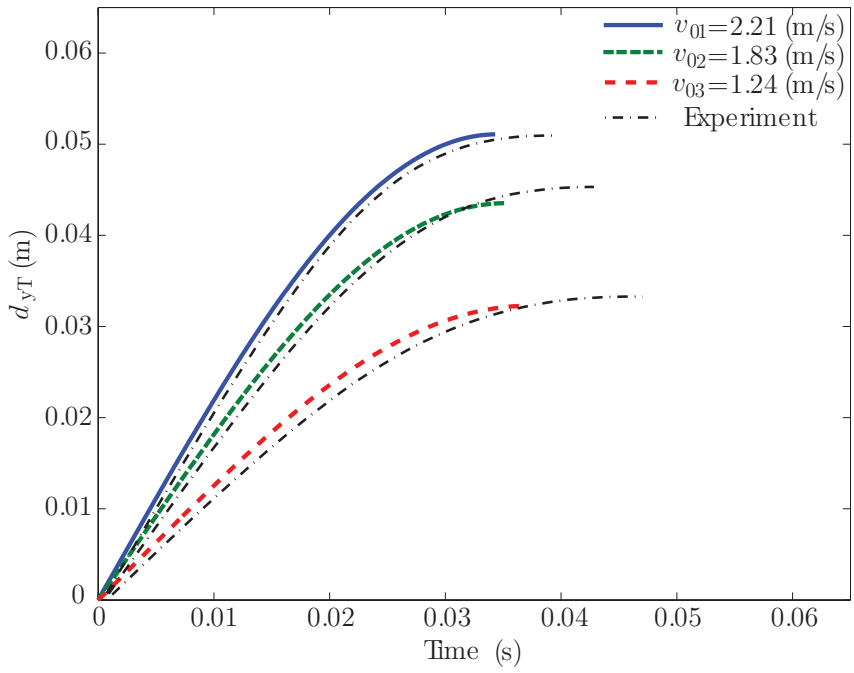

Figure 3.15: SolidWorks and experimental displacement results for impact at $q = 0^o$

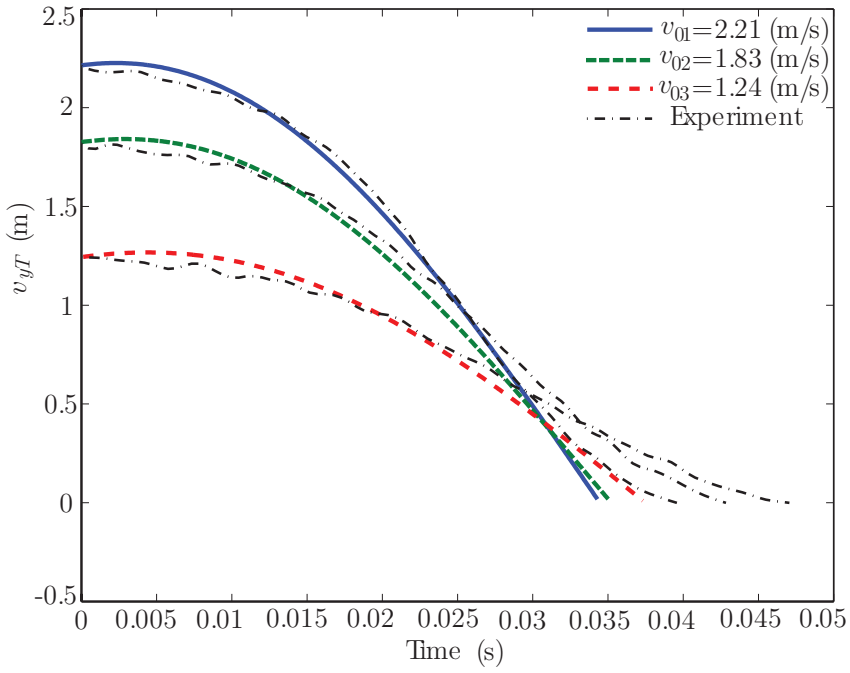

Figure 3.16: SolidWorks and experimental velocity results for impact at $q = 0^o$

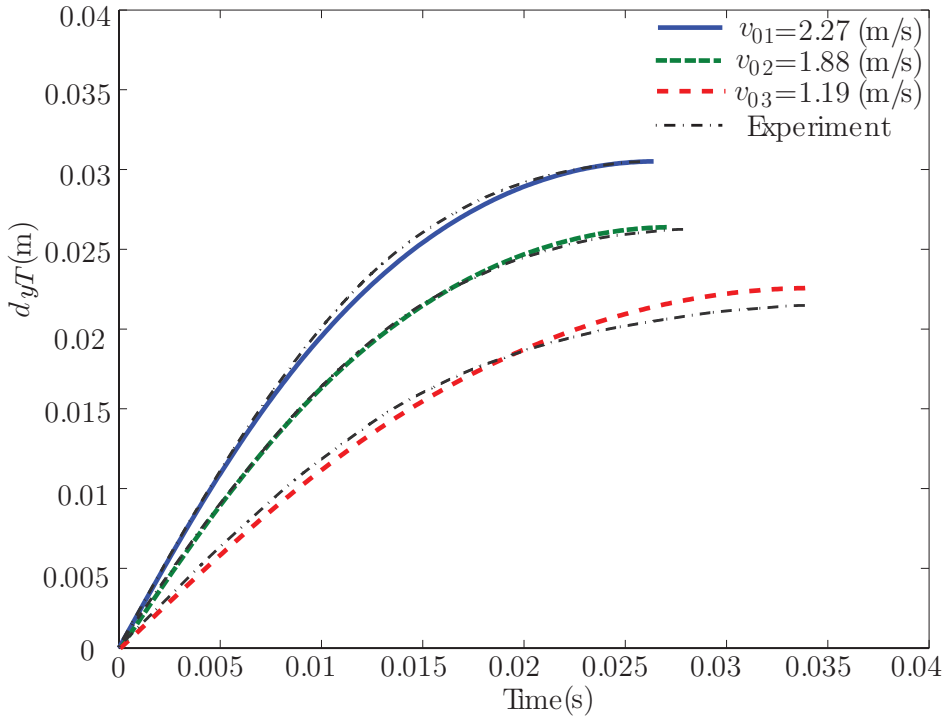

Figure 3.17: SolidWorks and experimental displacement results for impact at $q = 45^o$

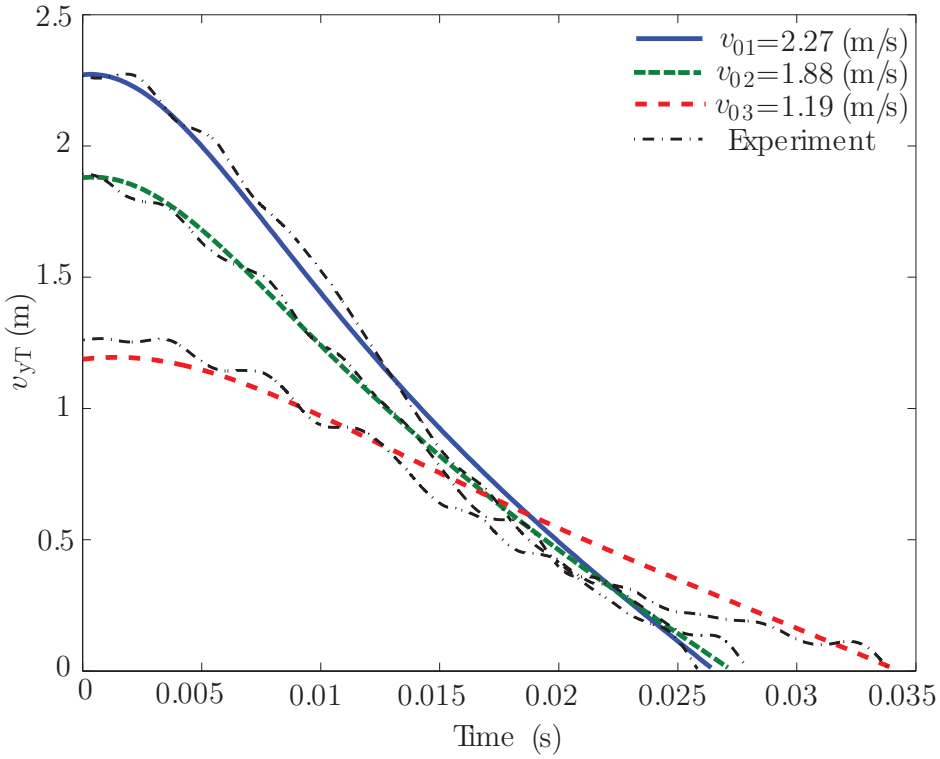

Figure 3.18: SolidWorks and experimental velocity results for impact at $q = 45^o$

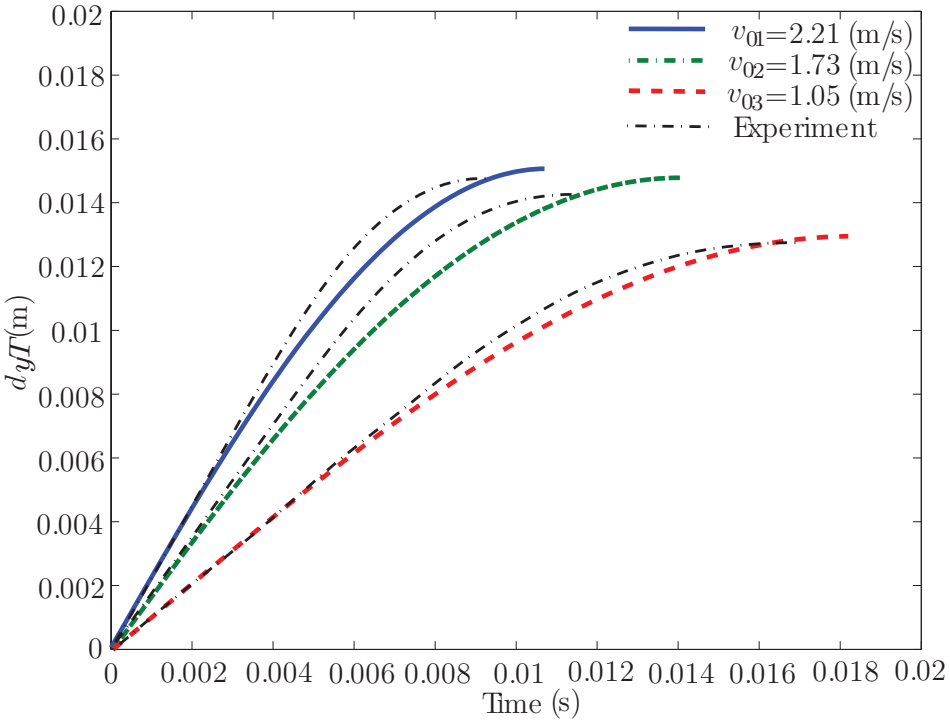

Figure 3.19: SolidWorks and experimental displacement results for impact at $q = 75^o$

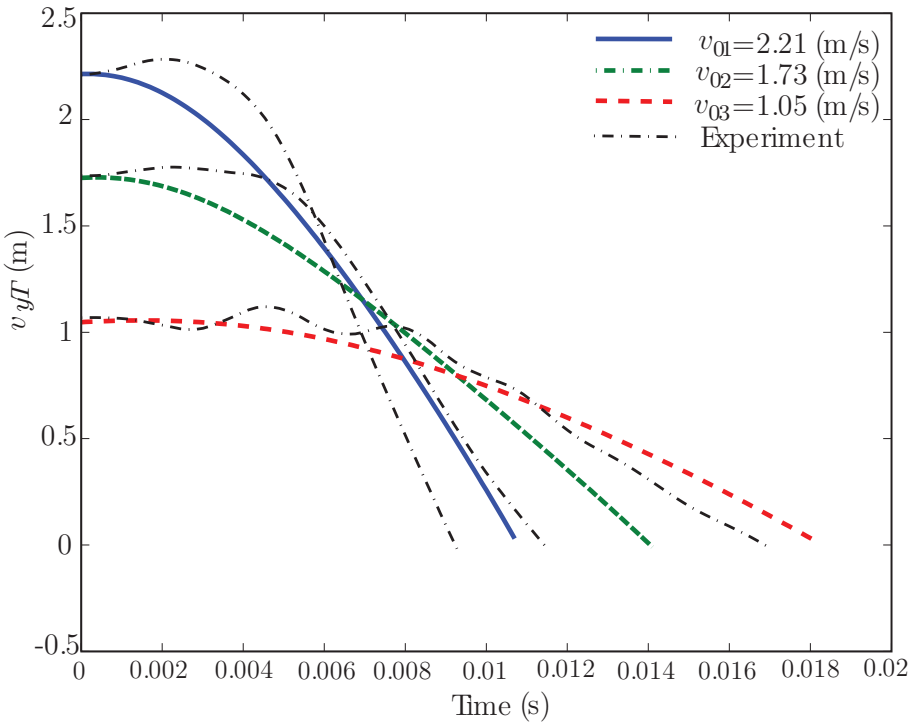

Figure 3.20: SolidWorks and experimental velocity results for impact at $q = 75^o$

- For $q(0) \simeq 0^o$: $v_{01}(0) = 2.21$ m/s at $q(0) = 0.29^o$; $v_{02}(0) = 1.82$ m/s at $q(0) = -0.51^o$; $v_{03}(0) = 1.24$ m/s at $q(0) = -0.48$.
- For $q(0) \simeq 45^o$: $v_{01}(0) = 2.27$ m/s at $q(0) = 43.5^o$; $v_{02}(0) = 1.88$ m/s at $q(0) = 44.9^o$; $v_{03}(0) = 1.19$ m/s at $q(0) = 43.72^o$.
- For $q(0) \simeq 75^o$: $v_{01}(0) = 2.21$ m/s at $q(0) = 75.6^o$; $v_{02}(0) = 1.73$ m/s at $q(0) = 75.5^o$; $v_{03}(0) = 1.05$ m/s at $q(0) = 75.6^o$.

With the higher impact velocity the rigid body traveled farther into the granular volume, although the intruder stopped faster due to the higher initial impact velocity. Figures 3.15 - 3.20 present the simulation and experimental results for the free link impact for different initial conditions: three velocities and $q = 0^o, 45^o$ and 75^o. The simulation curves (colored) are close to the experimental curves (black) for both displacement and velocity. The simulation results are thus verified by the experimental results in Figs. 3.15 - 3.20, endorsing the use of CAD software to simulate an impact with granular matter and the use of the expressions proposed for coefficients η_h, η_v, η_d, λ. The relative error between the simulation initial velocity and experimental initial

velocity, ϵ is given by

$$\epsilon = \left| \frac{de_{y_T}(t_s) - ds_{y_T}(t_s)}{de_{y_T}(t_s)} \right|, \tag{3.21}$$

where de_{y_T} is the final displacement extracted from experiments, and ds_{y_T} is the final displacement from simulation analysis when $v_{y_T}(t_s) = 0$. Table 3.3 contains the calculated relative errors between the simulation results and the experimental results for penetration depth. The Motion Analysis feature in SolidWorks produced results that were very close in terms of burrowing depth to the experimental results, but the stopping times differed significantly from the experimental measurements (see Figs. 3.15 - 3.20). These conclusions are consistent with the earlier results reported by Lee and Marghitu [30].

3.4 Analysis of the Angle Dependent Impact of a Free Rigid Link

This section takes a closer look at the effect of the angle at impact on the motion of the rigid body within the granular matter until it comes to a halt. The non-dimensional coefficients in the resistance force were the focus here, as this analysis was designed to validate the proposed expressions for η_d, η_h, η_v and λ listed in Table 3.2.

Several models were built in SolidWorks (Fig. 3.21), one for each angle of impact $\alpha(0) = 90^o, 85^o, 75^o, 65^o, 55^o, 45^o, 35^o, 25^o, 15^o, 5^o$, where α is defined as $\pi/2 - q$. For each case, the impact was simulated for the same three initial impact velocities as those used in the experiments for $\alpha(0) = 90^o, 45^o$ and 15^o:

- For $\alpha(0) = 90^o$: $v_{01}(0) = 2.21$ m/s; $v_{02}(0) = 1.82$ m/s; $v_{03}(0) = 1.24$ m/s.

	$v_{y_T}(0)$ (m/s)	ϵ (%)
$q = 0^o$	2.21	0.25
	1.82	3.92
	1.24	3.02
$q = 45^o$	2.27	0.08
	1.88	0.51
	1.19	5.05
$q = 75^o$	2.21	2.07
	1.73	3.67
	1.05	1.56

Table 3.3: Relative error between the experimental and simulation results for penetration depth

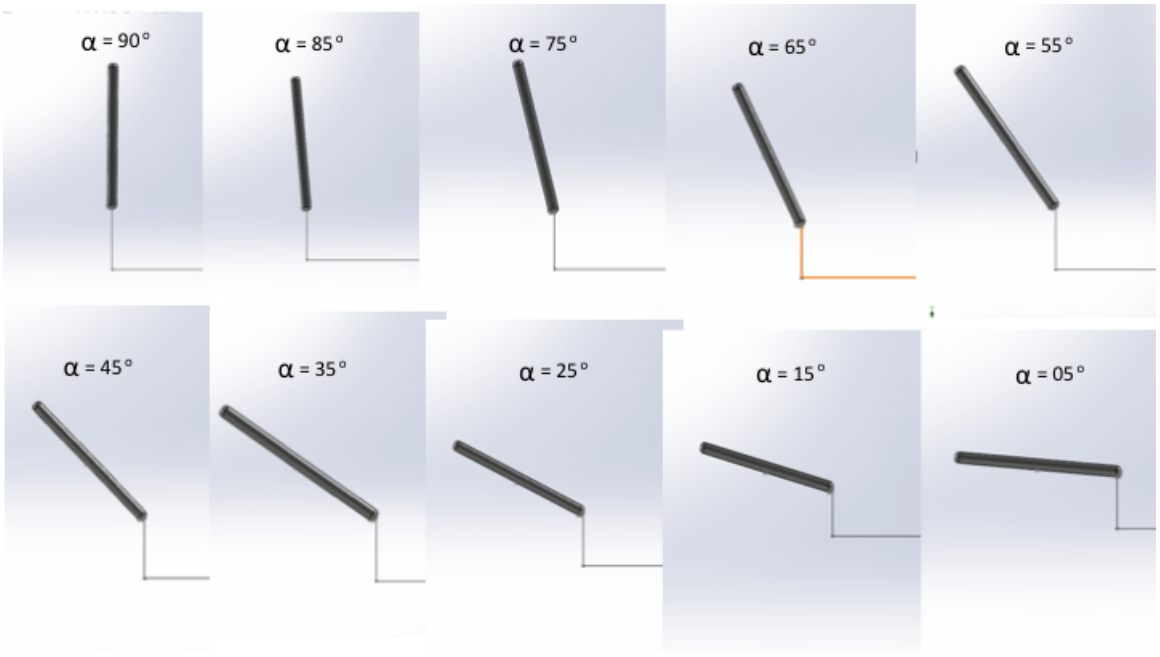

Figure 3.21: SolidWorks models for a range of angles of impact

- For $\alpha(0) = 85^o$: $v_{01}(0) = 2.25$ m/s; $v_{02}(0) = 1.79$ m/s; $v_{03}(0) = 1.17$ m/s.
- For $\alpha(0) = 75^o$: $v_{01}(0) = 2.25$ m/s; $v_{02}(0) = 1.77$ m/s; $v_{03}(0) = 1.16$ m/s.
- For $\alpha(0) = 65^o$: $v_{01}(0) = 2.24$ m/s; $v_{02}(0) = 1.77$ m/s; $v_{03}(0) = 1.12$ m/s.
- For $\alpha(0) = 55^o$: $v_{01}(0) = 2.24$ m/s; $v_{02}(0) = 1.77$ m/s; $v_{03}(0) = 1.15$ m/s.
- For $\alpha(0) = 45^o$: $v_{01}(0) = 2.27$ m/s; $v_{02}(0) = 1.88$ m/s; $v_{03}(0) = 1.19$ m/s.
- For $\alpha(0) = 35^o$: $v_{01}(0) = 2.24$ m/s; $v_{02}(0) = 1.77$ m/s; $v_{03}(0) = 1.12$ m/s.
- For $\alpha(0) = 25^o$: $v_{01}(0) = 2.24$ m/s; $v_{02}(0) = 1.75$ m/s; $v_{03}(0) = 1.12$ m/s.
- For $\alpha(0) = 15^o$: $v_{01}(0) = 2.21$ m/s; $v_{02}(0) = 1.73$ m/s; $v_{03}(0) = 1.05$ m/s.
- For $\alpha(0) = 05^o$: $v_{01}(0) = 2.25$ m/s; $v_{02}(0) = 1.78$ m/s; $v_{03}(0) = 1.13$ m/s.

The four components of the resistance force (Eqs. 3.17 - 3.20) were applied at the tip of the link, as this is the first point that contacts the granular matter surface at impact. The values for the coefficients η_d, η_h, η_v and λ were estimated using the expressions proposed in Table 3.2.

The density of the play sand in the container used was $\rho_g = 1650$ kg/m^3 (packing was taken into consideration). Adjustments such as rounding were made for velocity; changes were too small to be considered significant. In the simulations, where the values were regulated, are done by adjusting the value of η_h, as all the other coefficients this was calculated in terms of this coefficient. The resulting values that were used in the force expressions in SolidWorks are presented in Table 3.4. Empirical data [24] indicated that for a round ended cylinder type rigid body, $\eta_v \simeq 10$ and $\lambda \simeq 1.4$ [38] for burrowing motion. For the withdrawing motion, η_v is significantly smaller: $\eta_v \simeq 0.5$ and λ larger $\lambda \simeq 1.7$. The experiments that produced these results were performed at very low speeds: $v_0 = 0.5, 1, 5$ mm/s, allowing for the velocity dependent force to be ignored. Although few studies have examined the coefficient of a non-quasi static regime, the values estimated for the dynamic friction force are generally consistent with these results as η_d is significantly higher than 0.5 (which is an estimated value for a withdrawing motion) and closer to 10 (for a plunging motion). The value for η_h has been reported [7] to depend on the shape and size of the rigid body, as well as on the packing. The higher the volume fraction, the higher the coefficient. Low values for $\eta_h = 2.7 \pm 0.4$ have been found at very low speeds [8]. The experiments [38] that led to the proposed values for the power law λ were performed at very low speeds using glass beads as the medium, and the dependence on the shape of the intruder was not considered. However the work reported here demonstrates the importance of the container size for the power law values.

3.4.1 Final Displacement and Stopping Time

Applying the resistance force (Eq. 3.16) and the initial velocity conditions above to the ten models proposed, it is possible to obtain the penetration depth and stopping time for each case are given in Table 3.5.

Figure 3.22 shows that the final displacement is higher for increasing α, the angle with the negative horizontal. The penetration depth thus increases with the angle. The results also show that the initial velocity has a larger influence on the penetration depth of the burrowing rigid cylinder for higher angles, as demonstrated by the change in slope of the fitting curves for different velocities. The fitting curve of depth with impact angle for the initial velocity $v_{yT}(0) = 1.15$ m/s loses its linearity and instead assumes a positive curvature.

Angle $\alpha = \pi/2 - q$	η_h	η_d	η_v	λ
90	6.5	15.2	248	0.106
85	7.5	16.6	245	0.12
75	9	17.5	213	0.14
65	13.5	9	197	0.37
55	15.5	6.5	137	0.3
45	5.5	11	53	0.25
35	6.5	4.5	57	0.2
25	3.5	2.65	51	0.15
15	12	2	242	0.435
5	2	2	65	0.45

Table 3.4: The values for η_d, η_h, η_v and λ coefficients used in the resistance force

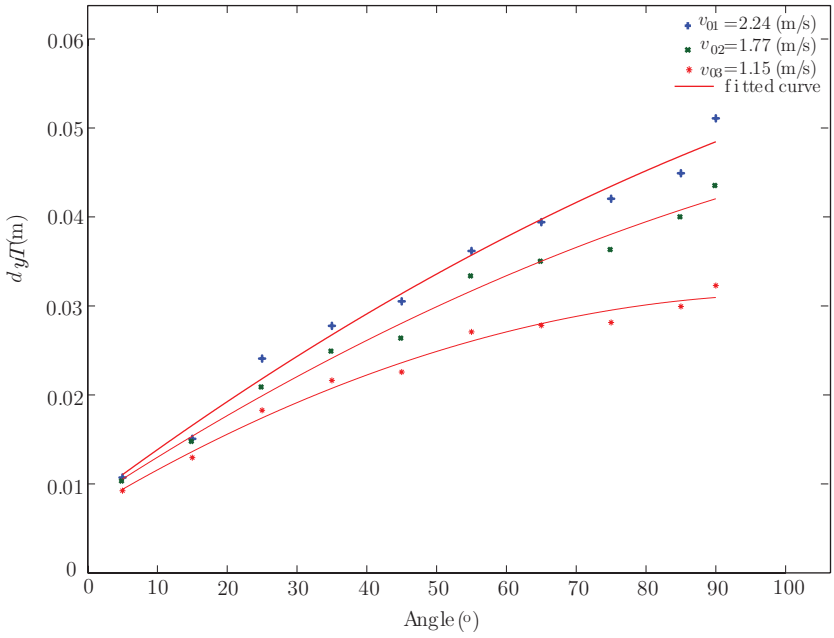

Figure 3.22: Simulation results for penetration depth with angle of impact α

	t_s (s)	d_{yT} (m)	v_{yT_0} (m/s)
$q = 0^o$	0.034	0.051	2.214
	0.035	0.044	1.826
	0.037	0.032	1.245
$q = 05^o$	0.031	0.045	2.245
	0.034	0.040	1.788
	0.037	0.030	1.171
$q = 15^o$	0.031	0.042	2.214
	0.033	0.036	1.826
	0.036	0.028	1.244
$q = 25^o$	0.029	0.039	2.245
	0.032	0.036	1.766
	0.036	0.028	1.120
$q = 35^o$	0.028	0.036	2.245
	0.031	0.033	1.766
	0.036	0.027	1.154
$q = 45^o$	0.026	0.030	2.27
	0.027	0.026	1.880
	0.034	0.023	1.188
$q = 55^o$	0.022	0.028	2.245
	0.024	0.025	1.766
	0.030	0.022	1.120
$q = 60^o$	0.025	0.030	2.147
	0.027	0.026	1.534
	0.046	0.022	0.656
$q = 65^o$	0.018	0.024	2.245
	0.020	0.021	1.754
	0.025	0.018	1.119
$q = 75^o$	0.011	0.0151	2.214
	0.014	0.0148	1.726
	0.018	0.013	1.048
$q = 85^o$	0.007	0.011	2.257
	0.009	0.010	1.787
	0.012	0.009	1.127

Table 3.5: Simulation results for the stopping time, t_s penetration depth, d_{yT} for a free round-ended link oblique impact at initial velocity v_{yT_0}

The stopping time, defined as the time it takes the rigid body to cease all forward motion into the granular volume, varies nonlinearly with increasing in angle, as displayed in Fig. 3.23. A comparison of the stopping times for different impact angles in a quadrant with distance traveled, shown in Fig. 3.24, indicates that the stopping time changes from an almost linear dependency at high velocity to supralinear at lower velocity. These results show that for low velocities the time tends to saturate at higher angles with horizontal. Therefore a smaller difference in stopping time will appear at higher angles.

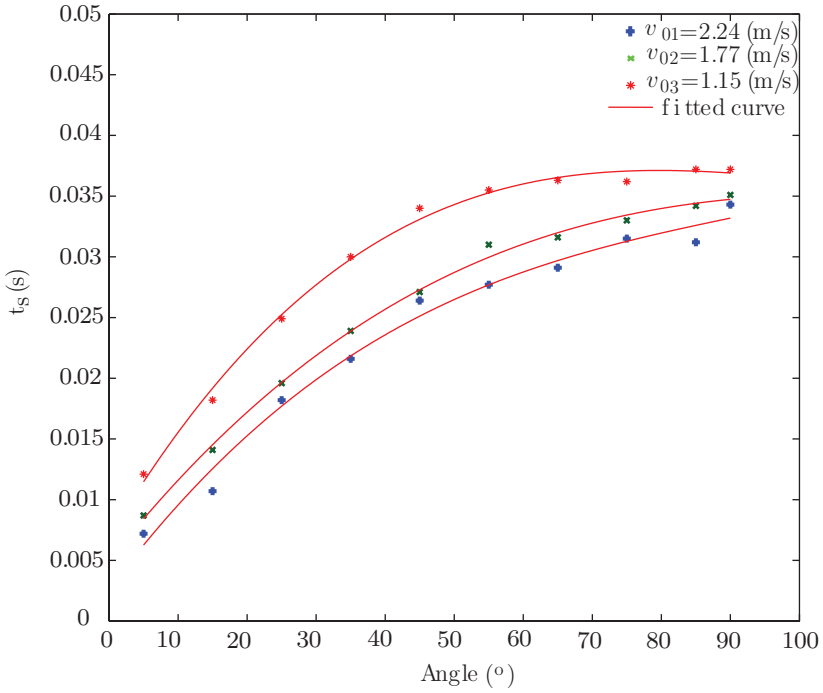

Figure 3.23: Simulation results for stopping time with angle of impact α

3.4.2 Change in Angle and Angular Velocity During Impact Analysis

During the surface penetration phase, the angle of the rigid link with the vertical changes according to the impact angle. This change, $\Delta q = q(t_s) - q(0)$, is shown in Fig. 3.25. The figure shows the fitted curve for the simulation results in Δq. For angles of impact $\alpha < 45^o$ the change in angle increases in a linear fashion with increasing the angle. As the initial impact velocity increases the slope also increases, resulting in higher final angles at the end of penetration phase. For angles

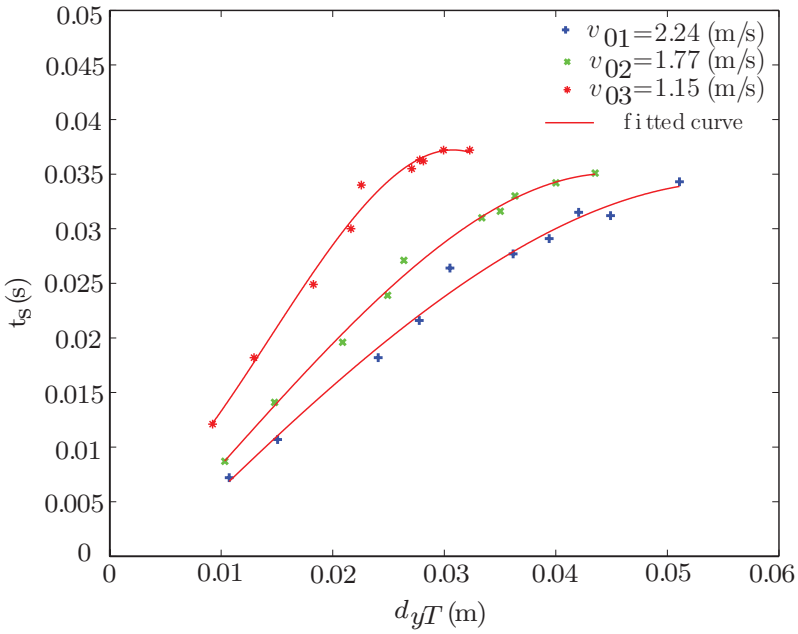

Figure 3.24: Stopping time for $\alpha = 05^o - 90^o$ with final displacement

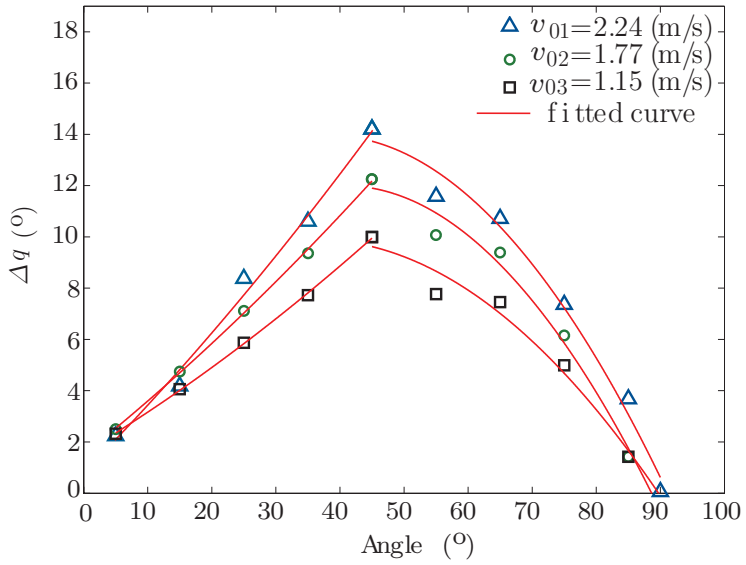

Figure 3.25: The change in angle during impact due to the angle of impact α

$\alpha > 45^o$, the change in angle decreases, but not linearly. The maximum change is at 45^o for all three initial velocities.

The change of angle in time during the penetration phase increases for angles from $\alpha = 90^o$ to $\alpha = 45^o$. From impact angles lower than 45^o, the angular velocity ω stabilizes and does not exhibit an angle dependency (see Fig. 3.26). However, increasing initial velocity, the value of ω increases.

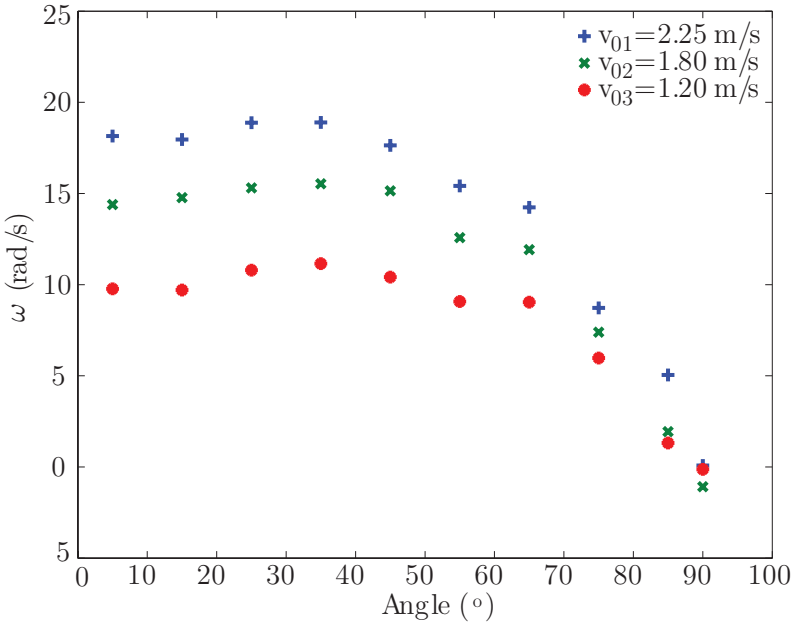

Figure 3.26: The angular velocity at the end of the penetration phase due to the angle of impact α

3.4.3 Resistance Force Analysis

Using a SolidWorks results feature, the reaction forces for the four components of the resistance force defined in Eqs. 3.17 - 3.20 can be extracted for the cases considered in this section. Appendix D contains the graphs of these terms as they act on the rigid body throughout the impact event. These graphs show how the horizontal and vertical dynamic forces, as well as the horizontal and vertical static forces depend on both the initial velocity and the impact angle. The values for the maximum dynamic friction force, static resistance force, at the end of the penetration phase and the total resistance force at the end of the impact are given in Table 3.6.

The static force is the displacement dependent component of the resistance force. This force is due to gravitation as the rigid body will tend to sink in a granular matter volume even at an initial

	F_d (N)	F_s (N)	F_r (N)
$q = 0^o$	0.12	22.87	22.87
	0.50	18.55	18.57
	0.06	13.40	13.40
$q = 05^o$	5.22	19.13	19.27
	1.92	17.22	17.22
	0.70	12.10	12.10
$q = 15^o$	7.44	15.45	15.62
	4.16	13.63	13.74
	1.60	10.14	10.21
$q = 25^o$	8.94	10.56	12.00
	5.67	9.29	10.22
	2.28	9.13	7.58
$q = 35^o$	8.00	9.91	11.00
	4.80	8.92	9.52
	1.99	6.90	7.20
$q = 45^o$	9.74	3.68	5.62
	7.34	3.80	5.21
	3.44	3.64	4.22
$q = 55^o$	6.69	5.08	7.08
	4.33	4.53	5.68
	1.73	3.42	3.84
$q = 65^o$	5.71	6.48	8.40
	3.53	5.86	6.75
	1.25	4.12	4.38
$q = 75^o$	5.10	15.36	16.65
	4.34	7.83	9.03
	1.09	5.51	5.72
$q = 85^o$	29.98	9.45	39.43
	15.31	8.62	23.93
	3.89	6.79	10.67

Table 3.6: Simulation results for the resistance force and its components for oblique impact of a free round-ended link

velocity $v(0) = 0$. The static resistant force acts on the body in reaction to the reorganization of the grains around the diameter of the intruder. Therefore, this force will depend on the direction of motion of the body in both the vertical and horizontal directions. The total static frictional force F_s is defined by Eq. 3.22.

$$F_s = \sqrt{F_{s_y}^2 + F_{s_x}^2}. \tag{3.22}$$

Figure 3.27 displays the static resistance force as it acts in time during the impact until the velocity of the rigid body drops to zero. It can be concluded that the force increases nonlinearly during impact, and tends to saturate before the end of the penetration phase. The magnitude of the static force is higher with increasing velocity. Given that the results presented in previous sections demonstrated that the intrusion ends faster at higher velocities, this means that at higher velocities, the static force will also reach higher values faster, and hence the grains will rearrange faster to oppose the intrusion motion.

Figures 3.27 and 3.28 show that $\alpha = 45^o$ is a critical angle for the reaction static force. At $\alpha = 45^o$, velocity appears to lose its influence as the magnitude of F_s for the three velocities considered are very close: F_s at $v_{01} = 3.67$ N , F_s at $v_{02} = 3.79$ N and F_s at $v_{03} = 3.63$ N.

The magnitude of the static force decreases for angles that are closer to a vertical impact, but at $\alpha \simeq 45^o$ the static force starts increasing. For impact angles $\alpha > 45^o$ the values of the static force appear to increase faster with increasing angle than the slope of the function F_s with α for smaller angles.

The dynamic resistance force, F_d arises due to the fluid properties of the granular matter and is therefore similar to the drag force in fluid dynamics. As a consequence, F_d represents the nonuniform distributed reaction from the polydisperse grains as they move, impeding the rigid body's motion and is thus highly sensitive to the velocity in both the horizontal and vertical directions. The total magnitude of F_D is defined by Eq. 3.23. The drag force is a reaction chain force between not only the grains in close proximity to the moving object but also subsequent layers, as a large scale reorganization of the grains is necessary [2].

$$F_d = \sqrt{F_{d_y}^2 + F_{d_x}^2}. \tag{3.23}$$

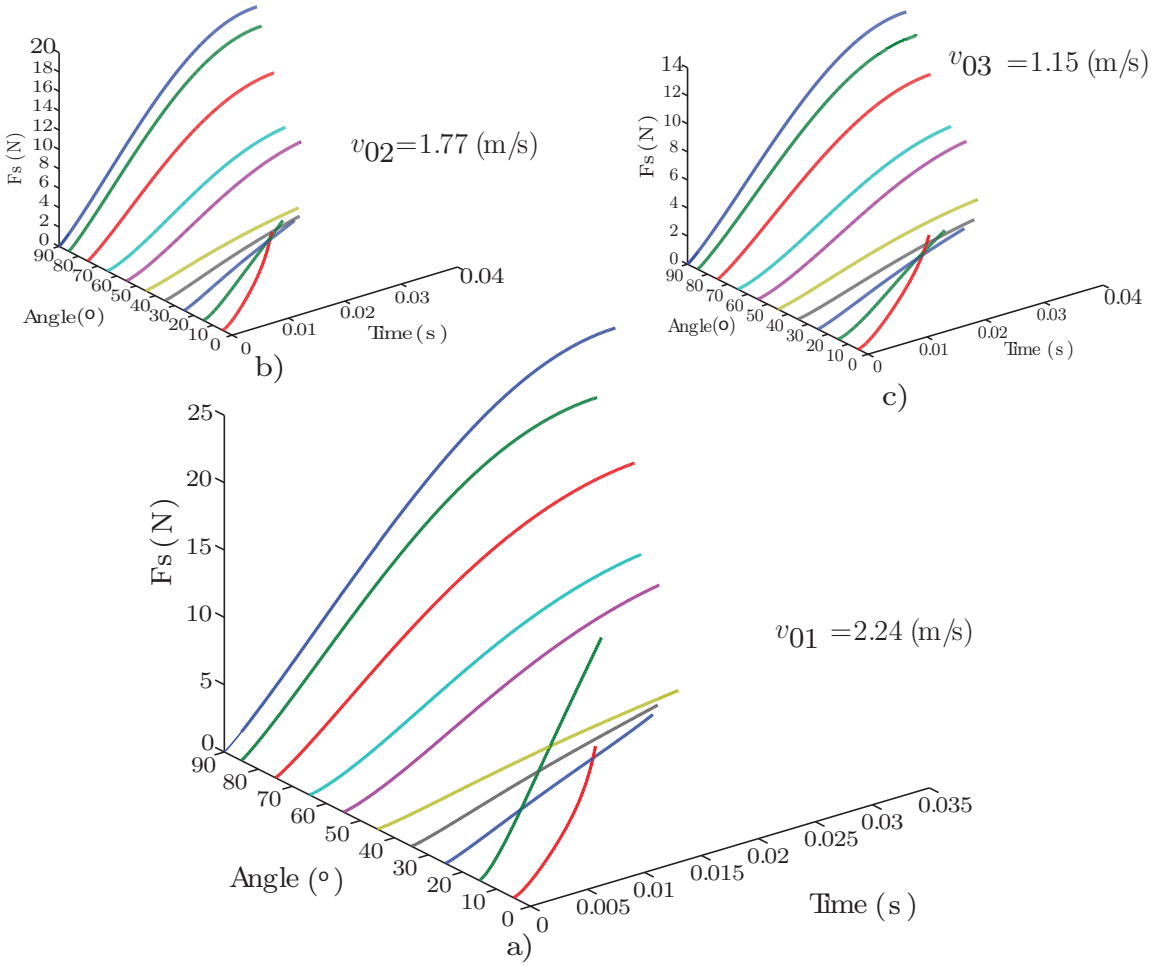

Figure 3.27: a) The static friction force for $\alpha = 0^o - 90^o$ during the link's drive at $v_{01} = 2.24$ m/s; b) The static force for $\alpha = 0^o - 90^o$ during the link's drive at $v_{02} = 1.77$ m/s; c) The static force for $\alpha = 0^o - 90^o$ during the link's drive at $v_{03} = 1.15$ m/s.

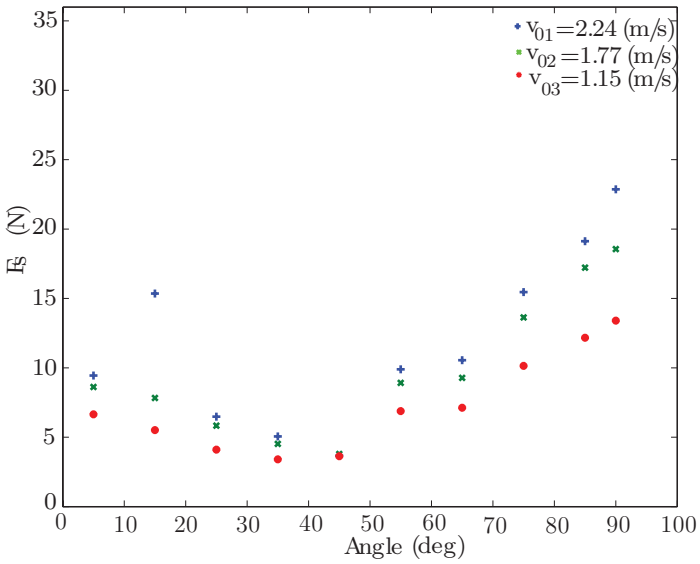

Figure 3.28: Maximum static force for impact at $\alpha = 0^o - 90^o$

When the moving object first enters the medium, the granular material will behave according to its fluid properties by engaging in a large-scale reorganization of the grains. The dynamic force increases until the repositioning transforms the medium and it starts to behave as a solid and the dynamic force decreases, as shown in Fig. 3.29.

Figures 3.29 and 3.30 illustrate how the magnitude of F_d depends on the impact angle. Note that for vertical impact and those that are close to horizontal the dynamic force exhibits uncharacteristic behavior. For a vertical impact the maximum $F_d \leq 0.5$, which is significantly less than its value in the other cases, while for $\alpha = 5^o$ the dynamic force does not decrease in value, but only changes inflection. For $10^o > \alpha < 80^o$ the maximum magnitude of the dynamic force does not seem to be highly dependent on the impact angle, although it does present as highly dependent on the velocity as the maximum magnitude of F_d increases with velocity. The maximum value for the dynamic force in this interval for an impact angle $\alpha = 45^o$ is higher than the static force for the higher impact velocities.

In the model studied here, both rate-dependent and displacement dependent phenomena must be taken into consideration. Therefore the total magnitude of the resistance force during an impact

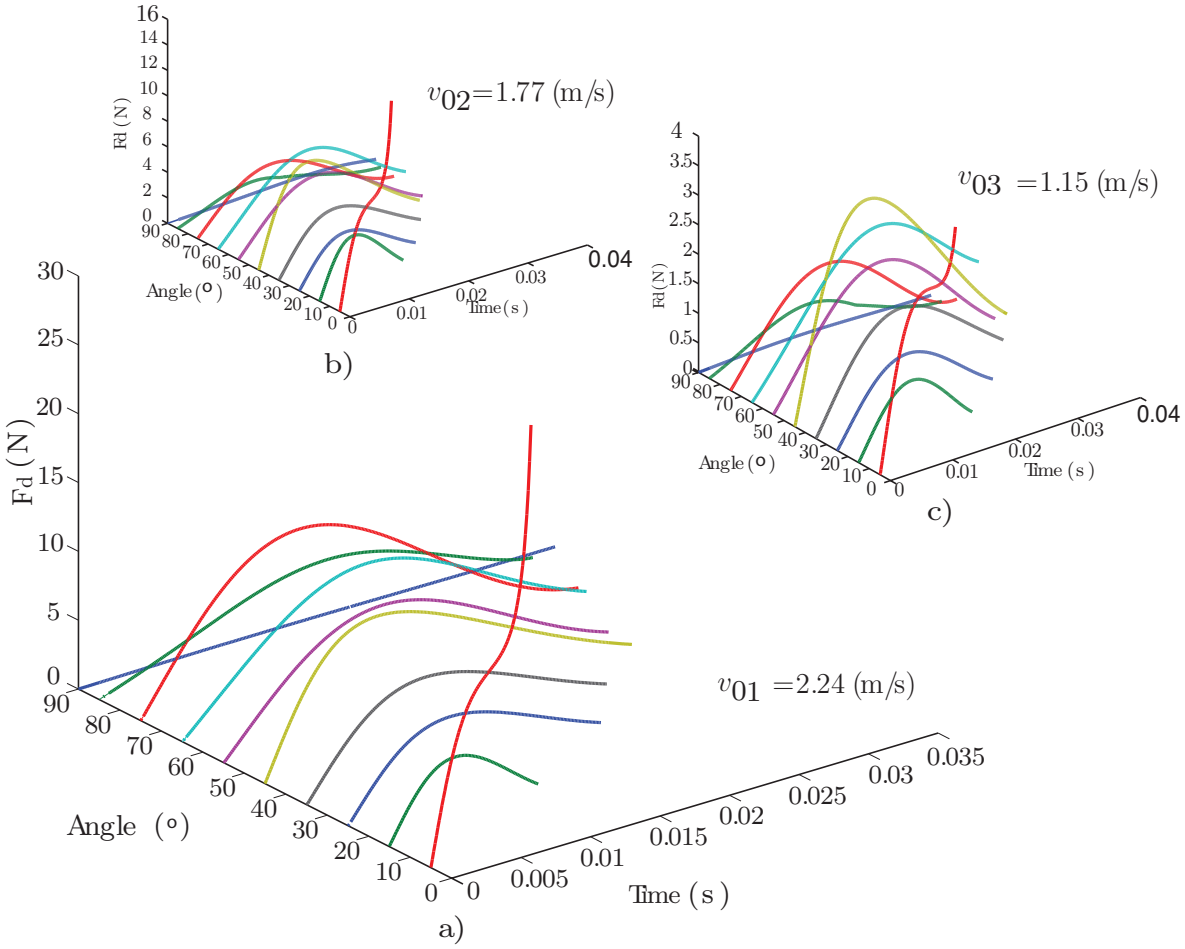

Figure 3.29: a) The dynamic force for $\alpha = 0^o - 90^o$ during the link's drive at $v_{01} = 2.24$ m/s; b) The dynamic force for $\alpha = 0^o - 90^o$ during the link's drive at $v_{02} = 1.77$ m/s; c) The dynamic force for $\alpha = 0^o - 90^o$ during the link's drive at $v_{03} = 1.15$ m/s.

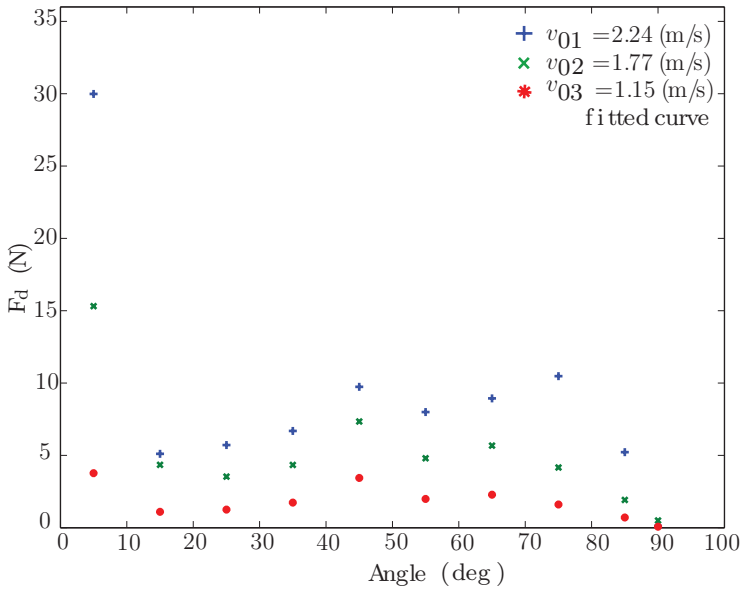

Figure 3.30: Maximum dynamic force for $\alpha = 0^o - 90^o$

with granular matter is defined by Eq. 3.24.

$$F_r = \sqrt{(F_{s_x} + F_{d_x})^2 + (F_{s_y} + F_{d_y})^2}. \tag{3.24}$$

The effects of both the velocity and depth dependency of the resistant force are evident in Fig. 3.32. The resistant force increases with time, although F_d has a greater influence on the resistance force at the beginning of immersion at higher velocities (Fig. 3.32(a)), the resistance force does not decrease to zero, as the static force compensates. For lower velocities, the dynamic force (Fig. 3.32 (c)) is not as obvious, but is present.

Due to the generally greater magnitudes of the static friction force, this force will have a major influence when considering how F_r depends on the impact angle. Figure 3.32 shows three fitted curves, one for each velocity, that characterize the resistance force as a function of angle. Each of these curves presents a minimum, but there is no axis of symmetry. The minimum for $v_{01} = 2.24$ m/s appears at $\alpha \simeq 40^o$ and that for $v_{02} = 1.78$ m/s appears at $\alpha \simeq 35^o$, with $F_r = 5$ N. The minimum $F_r = 4.5$ N for $v_{03} = 1.15$ m/s appears at $\alpha \simeq 30^o$. The maximum resistance force for $v_{01} = 2.24$ m/s appears at $\alpha = 5^o$ and is in the range of 40 N. $F_r = 13$ N is the maximum for the force due to a vertical impact when the initial velocity $v_{03} = 1.15$ m/s.

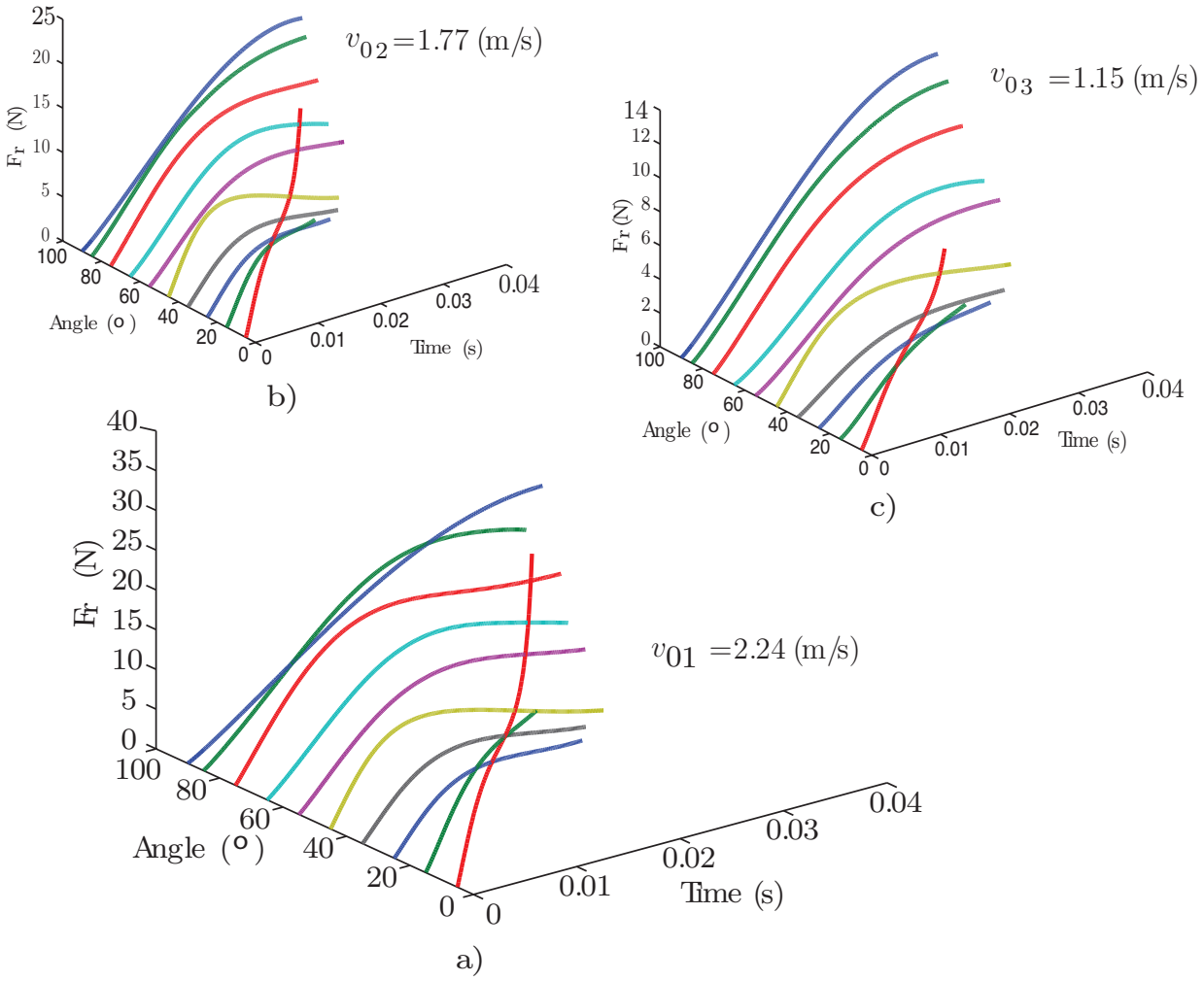

Figure 3.31: a) The resistance force for $\alpha = 0^o - 90^o$ during the link's drive at $v_{01} = 2.24$ m/s; b) The resistance force for $\alpha = 0^o - 90^o$ during the link's drive at $v_{02} = 1.77$ m/s; c) The resistance force for $\alpha = 0^o - 90^o$ during the link's drive at $v_{03} = 1.15$ m/s.

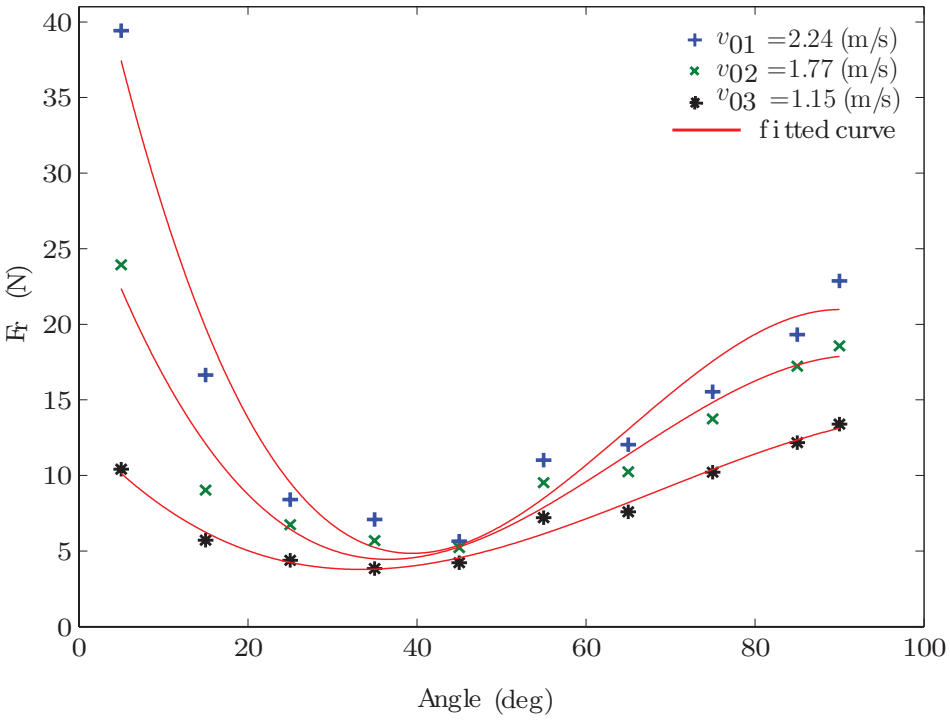

Figure 3.32: The resistance force at the end of the penetration phase for $\alpha = 0^o - 90^o$

3.4.4 Energy Analysis

Using the kinematics results presented above, this subsection discusses the mechanical energetics of the impact of a free rigid link with granular matter. Examining the mechanical energy dissipated in the granular matter substrate involves a study of the change in kinetic energy (Δ K. E.) and the change in potential energy (Δ P. E.) resulting form the immersion.

The total kinetic energy is the energy due to the motion of the link and includes both translational and rotational components, as defined in Eq. 3.25. The total potential energy represents the energy released during impact due to the change in position of the rigid body, as defined by Eq. 3.26.

$$\Delta\, KE = \frac{1}{2}\, m\, \Delta\, v_{COM}^2 \; + \; \frac{1}{2}\, I\, \Delta\omega^2, \tag{3.25}$$

$$\Delta\, PE = m\, g\, \Delta h, \tag{3.26}$$

where m is the mass of the rigid body, v_{COM} is the velocity of the center of mass of the rigid body, I is the mass moment of inertia with respect to the center of mass, ω represents the angular velocity of the rigid body during impact, g is the gravitational acceleration and h represents the vertical displacement of the rigid body during impact. To calculate the change in energy, the first state, s_1 is considered the moment when the tip of the bar comes in contact with the surface of the granular matter, and the final state, s_2 is defined as the moment when the velocity of the tip of the rigid body drops to zero. Therefore $\Delta = s_2 - s_1$.

The absolute values for the total kinetic energy, total potential energy and total energy dissipated during impact are given in Table 3.7 for the three initial velocities and all the impact angles simulated.

Because the mechanical energy is dissipated into the granular matter during immersion, the quantities displayed in Fig. 3.33 (a) and (b) are the absolute values of the change in kinetic energy (Fig. 3.33 (a)) and the change in potential energy (Fig.3.33 (b)) with the angle of impact. The results shown were extracted for each model using the SolidWorks features for calculating energy.

Intuitively, it was expected that the kinetic energy expenditure would depend on the initial velocity. Taking into consideration the angle of impact, the maximum kinetic energy (0.5 J) is dissipated during impact at higher velocities with the bar close to vertical. For angles $\alpha > 40^o$ the impact velocity plays an important role in the amount of kinetic energy as the slope of the fitted curve decreases with velocity. For angles of impact $\alpha < 40^o$, the fitted curve presents a negative curvature at $v_{01} = 2.24$ m/s, with values for the kinetic energy in the vicinity of 0.1 J (Fig. 3.33 (a)). As the velocity decreases, so does the curvature such that at $v_{03} = 1.15$ m/s it is close to zero, and the change in kinetic energy is near zero for this range of angles.

The potential energy, however, exhibits an opposite behavior. At very low impact angles, close to horizontal, the initial velocity has little to no influence on the change in potential energy $\simeq 0.025$ J (Fig. 3.33 (b)). With the rotation from the horizontal, a dependency on velocity emerges until the angle of impact is approximatively 45^o after which the potential energy gives the impression of stabilizing for each initial velocity.

Figure 3.34 superimposes the traces for the two types of energy to provide a better understanding of their individual influences on the total energy dissipated during penetration. For an initial velocity $v_{01} = 2.24$ m/s the kinetic energy is most significant with a minimum of 57% contribution

	ΔKE (J)	ΔPE (J)	ΔE (J)
$q = 0^o$	0.460	0.094	0.553
	0.310	0.080	0.392
	0.145	0.059	0.205
$q = 05^o$	0.465	0.083	0.549
	0.296	0.074	0.370
	0.127	0.055	0.182
$q = 15^o$	0.432	0.084	0.516
	0.264	0.072	0.336
	0.111	0.056	0.167
$q = 25^o$	0.344	0.089	0.433
	0.206	0.078	0.285
	0.072	0.062	0.134
$q = 35^o$	0.276	0.090	0.366
	0.165	0.081	0.246
	0.059	0.065	0.124
$q = 45^o$	0.197	0.089	0.287
	0.123	0.078	0.200
	0.036	0.065	0.101
$q = 55^o$	0.119	0.079	0.198
	0.058	0.070	0.128
	-0.001	0.060	0.060
$q = 65^o$	0.092	0.068	0.160
	0.043	0.059	0.102
	-0.003	0.050	0.047
$q = 75^o$	0.097	0.04	0.137
	0.042	0.042	0.084
	0.000	0.034	0.035
$q = 85^o$	0.103	0.028	0.131
	0.057	0.027	0.084
	0.012	0.024	0.036

Table 3.7: Simulation results for the energy dissipated during the oblique impact of a free round-ended link with granular matter

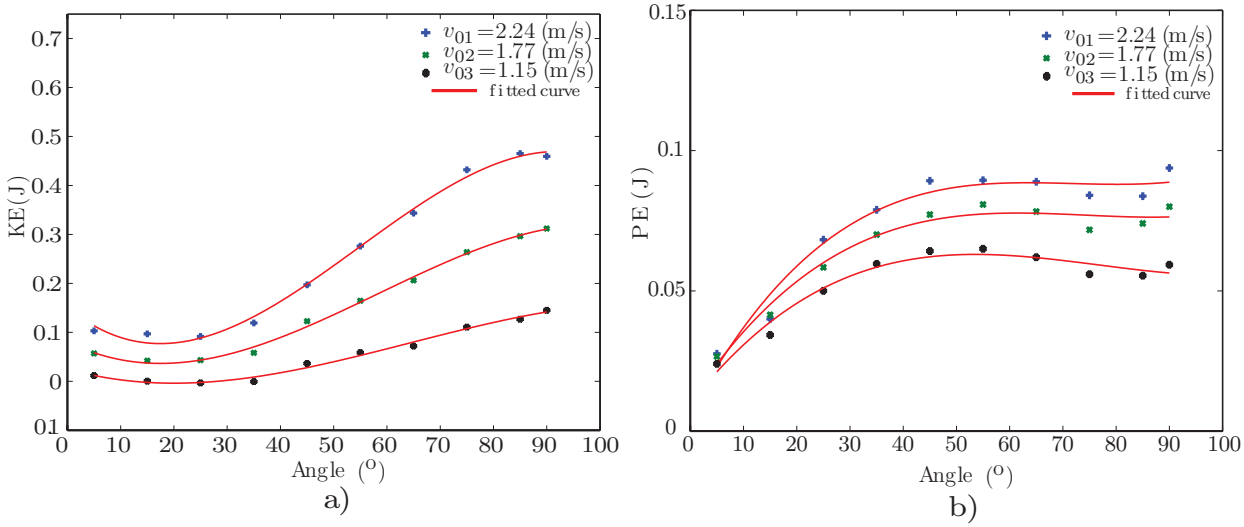

Figure 3.33: Energy dissipated during penetration phase with angle: a) The kinetic energy; b) The potential energy.

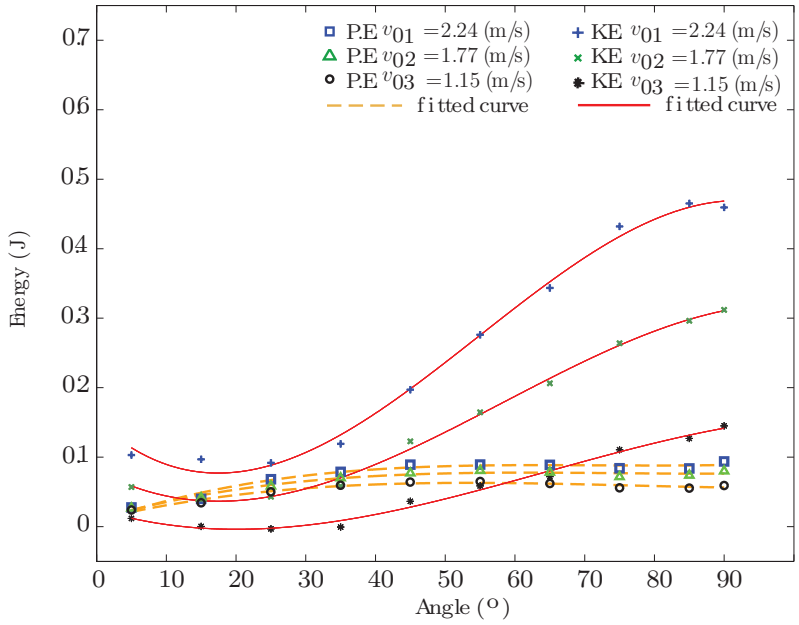

Figure 3.34: The kinetic and potential energy dissipated superimposed

to the total energy at $\alpha = 25^o$ and a maximum of 85% for impact closer to vertical. For an intermediate initial velocity $v_{02} = 1.77$ m/s the potential energy makes almost the same contribution as the kinetic energy for angles between 15^o and 35^o. For a smaller initial velocity $v_{01} = 1.15$ m/s, potential energy is the major contributor to the total energy for angles $\alpha < 55^o$. For $15^o > \alpha < 35^o$ the total energy consists almost entirely of potential energy.

The total energy as a function of impact angle will thus tend to carry the shape of the kinetic energy, as shown in Fig. 3.35, although there will be slight changes for for impact at lower angles with lower initial velocities. For $v_{03} = 1.15$ m/s, the total energy dissipated during the immersion of a free link into granular matter increases quasi-linearly with the impact angle.

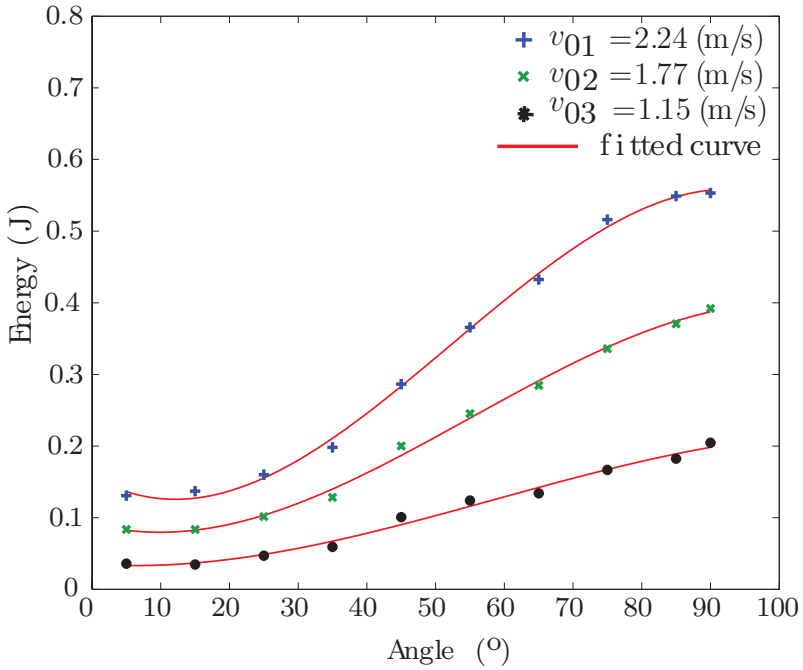

Figure 3.35: The change in total energy dissipated during the penetration phase with angle

The maximum mechanical energy the rigid body will dissipate is 0.55 J for a vertical impact with $v_{01} = 2.24$ m/s, while for the same vertical angle the mechanical energy dissipated at impact with $v_{03} = 1.15$ m/s will be 0.14 J. Given that impact at higher velocity will end faster, this means that the bar will dissipate 0.5 J of energy in 0.034 sec, but it will take 0.0372 sec to dissipate 0.14 J. This may explain a phenomenon commonly observed for impact with granular matter, where the intruder will stop faster with higher initial velocity because the system will release more energy (the kinetic energy being the main contributor at high initial velocities) to the granular substrates.

Thus, the grains will reorganize faster and enter the solid state faster, stopping the immersion of the rigid body. This study of the energy dissipation mechanism can also help with gauging the erosive power of the link in the granular matter volume.

3.5 Conclusions

This chapter presented a study on the impact of a free rigid link on granular matter. The model created in SolidWorks produced results that are comparable to the experimental results for the penetration depth of the tip of the rigid body. The depth increases with the initial impact velocity, while the stopping time decreases with increasing velocity, forcing the object to stop more rapidly. The SolidWorks simulation used a combination of a quadratic velocity dependent term and a displacement dependent term for the resistance force to simulate the impact with polydispersed grains. A series of expressions were proposed to approximate the values for the coefficients in the force terms. These values were estimated for 30 cases in which not only the velocity was varied, but the impact angle if the rigid body as well. This study showed that the dynamic force plays a major role in the increase of the resistance force, thus confirming that it is advisable not ignore the velocity dependent term of the force in such impact. The study also identified critical angles of impact that produce a change in the reaction force. This result is consistent with other research [52] that has shown the existence of a critical angle. The analysis of the resistance force in this chapter also revealed that at small impact angles with the horizontal, the force exhibits more complex features. The simulation results demonstrated that for a vertical impact, the dynamic force has only a very small influence on the resistance force. Although the energy dissipation enforced the concept of critical impact angles, it also introduced the theoretical concept of a critical velocity below which the potential energy makes greater contribution to the total energy. A similar conclusion can be drawn for the contribution of the dynamic force to the total resistance force.

Chapter 4

Impact of a Double-Link Kinematic Chain with Granular Matter

This chapter presents a study of a two link impact, with two contact points, with granular matter. The penetration depth and velocity analysis is presented for a set of experiments produced at three different initial velocities. A simulation model was created in SolidWorks. Applying the analytical force model used for one link impact described in the previous chapter, the displacement, reaction force and mechanical energy produced by the simulation model were analyzed.

4.1 Model of the Impact of a Double Kinematic Chain

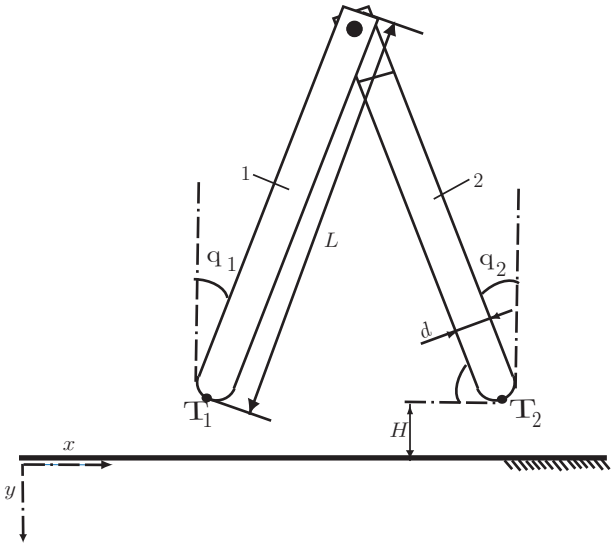

Figure 4.1: Two link kinematic chain

The schematic of the experimental system used to examine the impact of a kinematic chain with two impact points is shown in Fig. 4.1. The two round ended steel links in this system were identical in mass and dimensions: diameter $d_1 = d_2 = 0.0064$ m and length $L_1 = L_2 = 0.135$ m. Each link had a plastic washer with a thickness of 0.5 mm around the screw hole. This washer was

placed between the links to reduce the friction between the two links to a negligible level while at the same time allowing them to rotate around a screw at the top.

As in the case of the single impact point considered in Chapter 3, the system was constrained to a planar motion in a fixed Cartesian reference frame. The positive x axis is considered to be the right and the positive y axis is considered to be downward (Fig. 4.1). The angle between Link 1 and the y axis is q_1, and the angle between Link 2 and the vertical y axis is q_2. These angles constitute the impact angles of the system with the granular volume. The angle between the two links is $\alpha = 30^o$ (Fig. 4.1). The system is in free fall from height H so that that impact velocity for points T_1 and T_2 is $v_{0_{T_1}} = v_{0_{T_2}} = \sqrt{2\,q\,H}$.

The impact of each link was modeled using the single point impact resistance force expressions given in Eq. 3.16. One such force exists for each link, therefore F_{R_1} acts in the centroid of the immersed volume of link 1 and F_{R_2} acts in the centroid of the immersed volume of link 2. Each of these forces will depend on the impact angle. To estimate the constants η_d, η_h, η_v and λ that are needed to scale the F_{R_i} (i=1,2) forces, expressions from Table 3.2 are utilized with a couple of compromises insert space. The appropriate expressions form Table 3.2 are used with small adjustments due to the changed dynamics, as there is a reaction force acting in the pin between the two links. Lee and Marghitu performed a numerical study of the impact of multiple link kinematic chains [31] using a symmetric and asymmetric two link model with links. They derived appropriate equations of motion using the Newton-Euler method, and solved the system numerically, concluding that just as in the case of a single point impact [31], the stopping time of the penetrating object decreases with increasing velocity. The expression used for the dynamic force F_d differs from the expressions used in this study in terms of the way the dependency on the density of the granular volume is invoked. The Lee and Marghitu expression is $\mathbf{F}_d = -\frac{\mathbf{v}}{|\mathbf{v}|}\,\beta A\mathbf{v}\cdot\mathbf{v}$. Here the coefficient $\beta = 1569.9$ hides the value for ρ_g. Thus the expression for F_d (Eq. 3.23) proposed in this study improves on that expression.

4.2 Experimental Setup and Results

4.2.1 Experimental Setup

The system used to capture the motion of the two link system is the same Northern Digital Inc. OPTOTRAK 3020 as that used for the study reported in Chapter 3. Figure 4.2 illustrates the equipment set-up. For this system, four IR sensors were utilized (Fig. 4.3), with one being positioned in the center of each link (M_1 and M_3), one on the top M_2 of the screw so that it would not interfere with the rotation, if necessary, of the links and the fourth on the granular medium surface. The pipeline used in NDI Toolbench to extract the position in time of the four links is presented in Appendix E. Appendix F represents a 2D view of the IR markers as their position is recorded by the NDI Toolbench when the pipeline is evaluated.

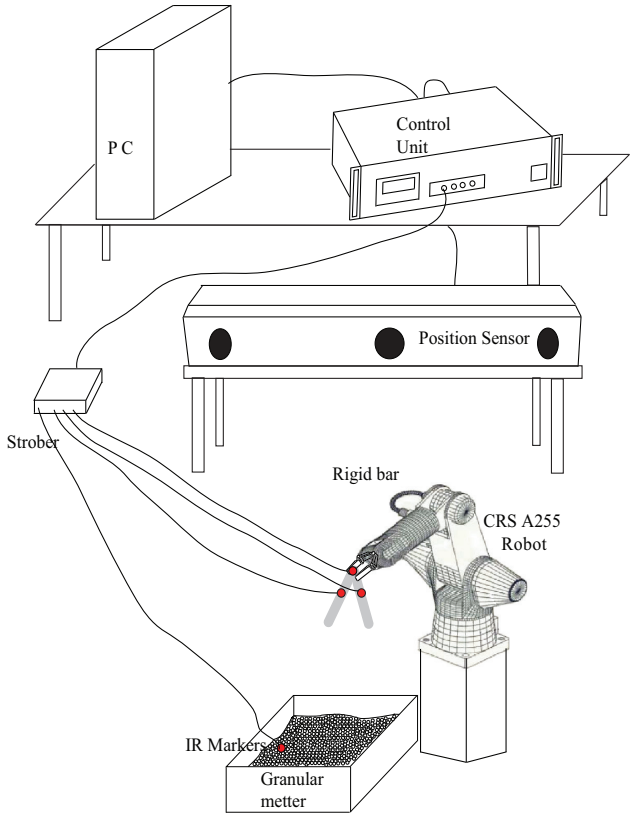

Figure 4.2: OPTOTRAK 3020 equipment setup for impact of a two link kinematic chain with two points of impact with granular matter

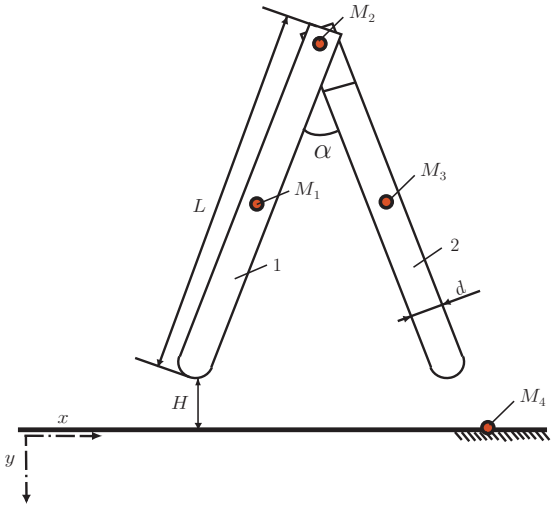

Figure 4.3: Positioning of the four IR markers on the kinematic chain

	$v_T(0)$ (m/s)	$q(0)$ (^{o})
Link 1	2.57	-16.72
	2.29	-14.70
	1.60	-14.08
Link 2	2.57	13.48
	2.29	15.50
	1.61	16.00

Table 4.1: The angles with the vertical at impact for the two links

The granular medium utilized for the experiments in this study was the same as in the previous experiment with one free link, "Play sand" (Quikrete 1113-51) . The granular matter was contained in a box of dimensions $0.45 \times 0.32 \times 0.09$ m (L $\times$ W $\times$ H). This container was significantly larger than the size of the kinematic chain, thus the Jansen effect was not expected to be a factor. The granular matter was stirred and leveled before each drop to eliminate material history, but still maintain the same packing characteristics for each run.

4.2.2 Experimental Results

To examine the impact of a two link kinematic chain, the experiments were performed for three initial velocities. In each case, four sets of data were recorded. Table 4.1 lists the average initial conditions for all three cases.

	t_s (s)	d_{yT} (m)	$v_{yT}(0)$ (m/s)
Link 1	0.024 ± 0.003	0.035 ± 0.002	2.58 ± 0.021
	0.026 ± 0.003	0.030 ± 0.001	2.29 ± 0.118
	0.029 ± 0.001	0.025 ±0.0005	1.60 ± 0.036
Link 2	0.026 ± 0.002	0.037 ± 0.001	2.57± 0.036
	0.030 ± 0.005	0.031 ± 0.002	2.3 ± 0.095
	0.032 ± 0.002	0.025 ± 0.0003	1.61 ± 0.025

Table 4.2: The experimental results for the two end points of the double kinematic chain

For each recording the position data during impact was extracted. The impact for each link starts when the position of the tip of the respective link is zero (for Link 1 $d_{T_1} = 0$ and for Link 2 $d_{T_2} = 0$. The links reach zero displacement with the surface at the same time (for $v_{T_1}(0)$, $\Delta t(0) = 0.0013$ s; for $v_{T_2}(0)$, $\Delta t(0) = 0.0005$ s; for $v_{T_3}(0)$, $\Delta t(0) = 0.0003$, where $\Delta t(0) = t_1(0) - t_2(0)$ is the difference in the time the tips of the two links start penetrating the surface). Table 4.2 shows the average recorded stopping time, t_{s_1} for link 1 and t_{s_2} for link 2; final displacement, $d_{yT_1}(t_{s_1})$ for link 1 and $d_{yT_2}(t_{s_2})$ for link 2; initial impact velocities $v_{yT_1}(0)$ for link 1 and $v_{yT_2}(0)$ for link 2, as well as the standard deviation values for the five series of data for each initial velocity.

Figure 4.4 shows the displacement of the tip of each link during immersion for the three initial velocities in Table 3.1. For each link, the displacement in the granular medium increases with increasing of velocity, but the stopping time decreases with higher velocity. These results are supported by the change in velocity during penetration shown in Fig. 4.5. Interestingly, both links reach the same displacement at the penetration phase of the impact, although link 2 (see Table 4.2) takes longer to reach it. This can be attributed to the interaction between the two links upon impact and the slight differences in the velocities at impact for each link.

4.3 Simulation of The Impact of a Double Kinematic Chain with Granular Matter

4.3.1 Simulation Model

SolidWorks ® 2013-2014 was used to simulate the impact of the two-link system employed in the experiments. The assembly shown in Fig. 4.6 includes the two links (that have the Nylon 101 washers embedded) and the washer between the links. Each part is constructed with the same dimensions as the actual parts used in the experiment: diameter $d_1 = d_2 = 0.0064$ m and length

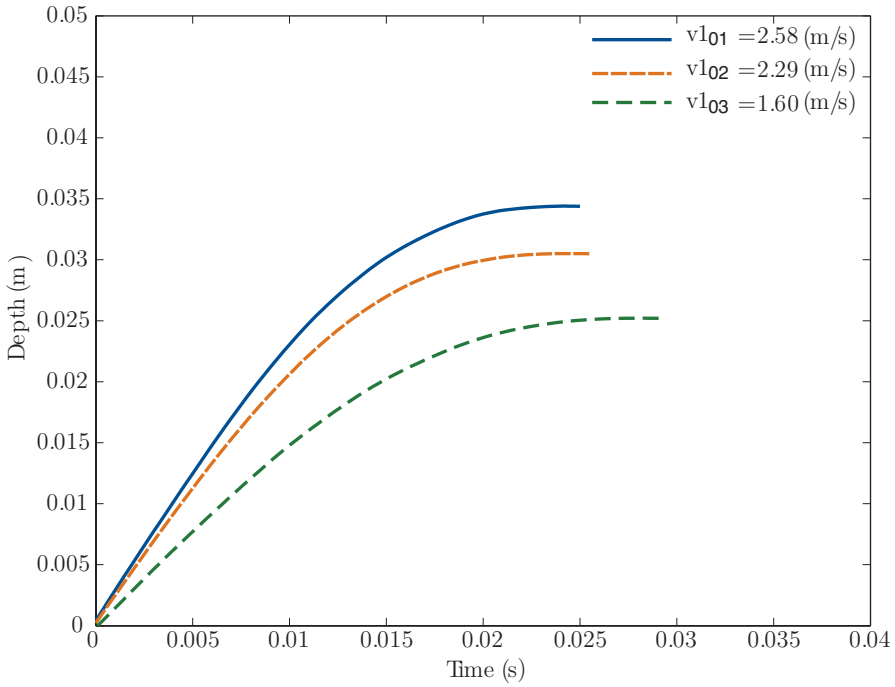

(a) Displacement in time of the tip point T_1 for Link 1

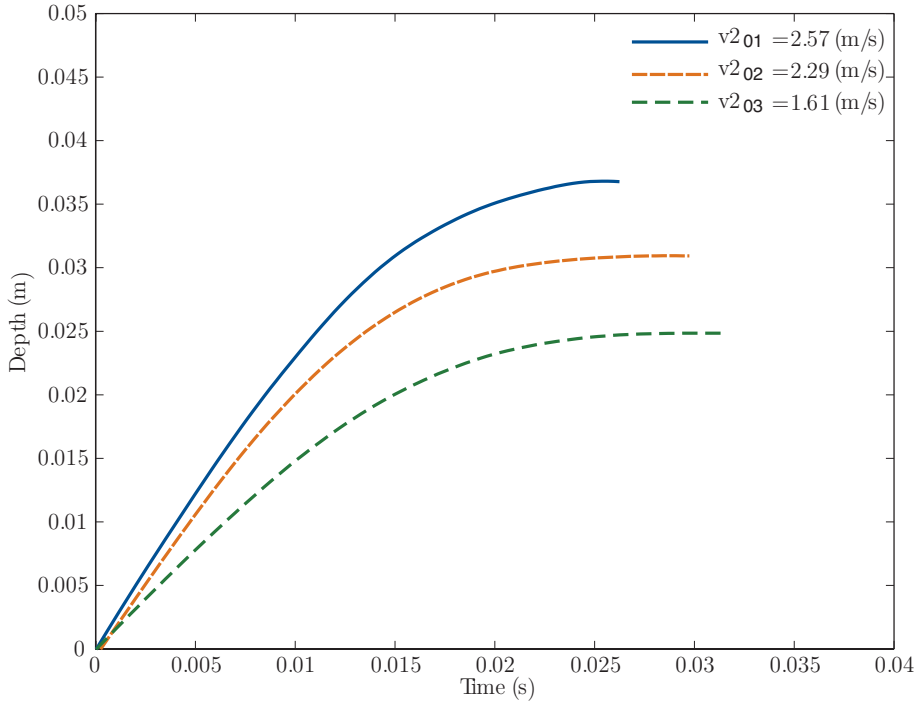

(b) Displacement in time of the tip point T_2 for Link 2

Figure 4.4: The experimental results for displacement during impact of a double kinematic chain with two contact points: (b) for link 1, and (b) for link 2

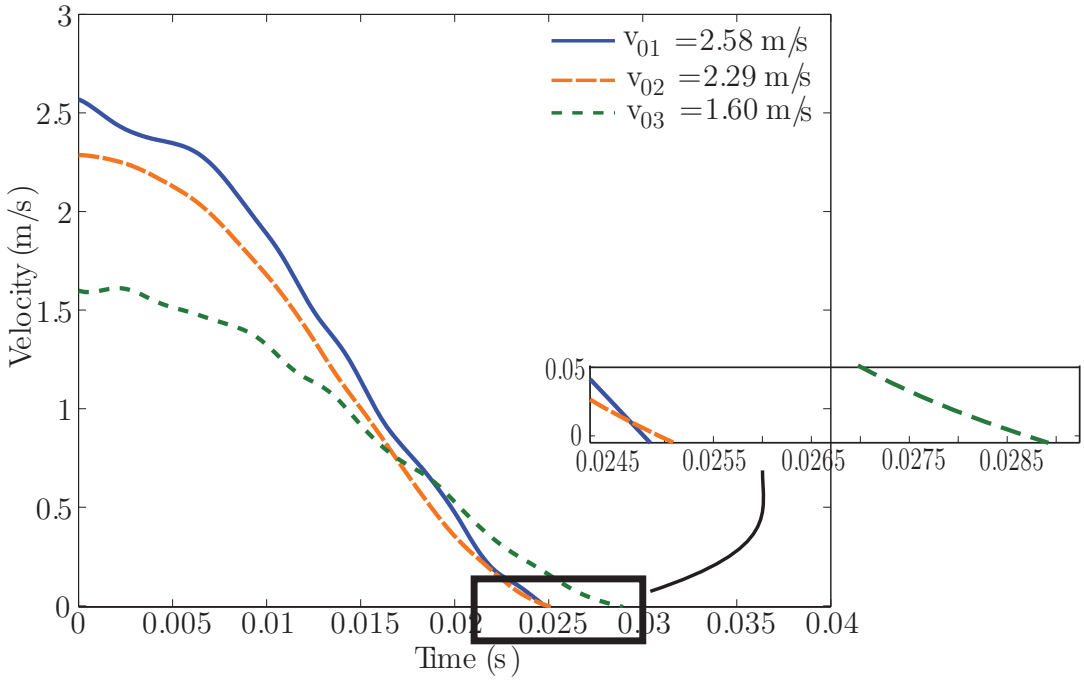

(a) Velocity in time during the penetration phase of the tip point T_1 for Link 1

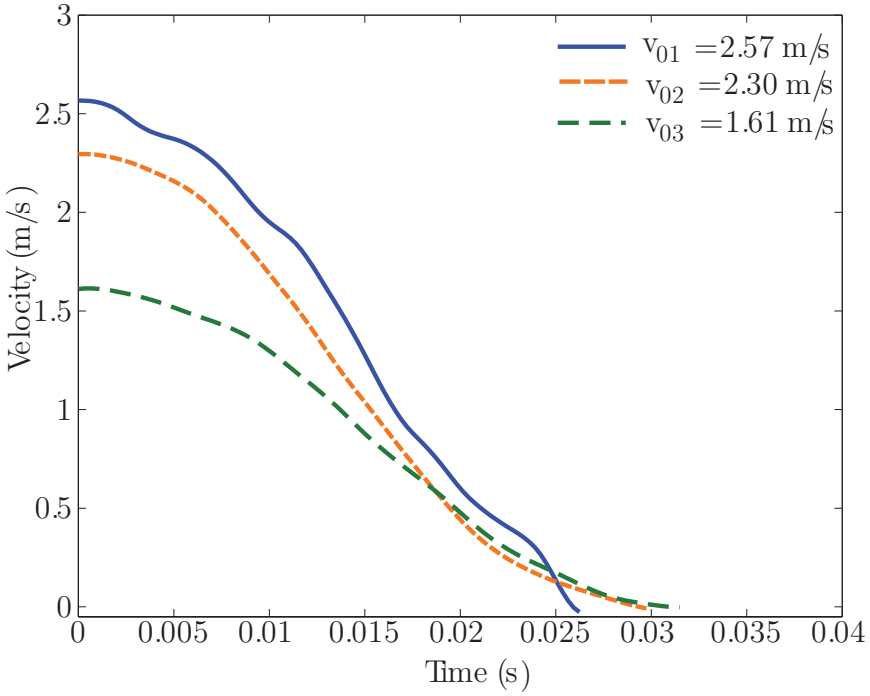

(b) Velocity in time during the penetration phase of the tip point T_1 for Link 2

Figure 4.5: The experimental results for velocity during impact of a double kinematic chain with two contact points: (a) for link 1, (b) for link 2

$L_1 = L_2 = 0.135$ m . The system is held together by mates of concentric and coincidence type, so that as in the real system the links are allowed to rotate about the top point with negligible friction.

The resistance force used to simulate the impact with the granulate matter is given in Eq. 2.1. This force acts at the contact point with the surface on each link in the opposite direction to the motion of each link. Thus for $i = 1, 2$, the resistance force $\mathbf{F}_{r_i} = \mathbf{F}_{d_i} + \mathbf{F}_{s_i}$, where

$$\mathbf{F}_{d_i} = -\frac{\mathbf{v}_{E_i}}{|\mathbf{v}_{E_i}|}\,\eta_{d_i}\,A_{r_i}\,\rho_g\,\mathbf{v}_{E_i}\cdot\mathbf{v}_{E_i}, \tag{4.1}$$

$$\mathbf{F}_{s_i} = \left(-\text{sign}(v_{E_{x_i}})\,\eta_{h_i}\,g\,\rho_g\,d_c\,d_{yT_i}^2\right)\mathbf{\imath} - \left(\text{sign}(v_{E_{y_i}})\,\eta_{v_i}\,(d_{yT}/L)^{\lambda_i}\,g\,\rho_g\,V_i\right)\mathbf{\jmath}. \tag{4.2}$$

The reference area, A_{r_i} in Eq. 4.1 is defined as the immersed longitudinal area of each link i and is given by Eq. 3.13. The volume V of the immersed rigid body will be calculated in terms of the impact angle of each link by Eq. 3.15. The velocity of the center of the immersed volume is defined according to Eq. 3.4 for each link as

$$\mathbf{v}_{E_i} = \left(v_{xT_i} + \frac{d_{y_{T_i}}}{2}\,\omega_i\right)\mathbf{\imath} + \left(v_{yT_i} + \frac{d_{y_{T_i}}}{2}\,\tan(q_i)\,\omega_i\right)\mathbf{\jmath}. \tag{4.3}$$

In the SolidWorks assembly, the resistance force is applied as four components ($F_{d_{x_i}}$, $F_{d_{y_i}}$, $F_{s_{x_i}}$, $F_{s_{y_i}}$) at the end point of each link (Appendix G). The expressions for these components are given by Eqs. 4.4- 4.7

$$F_{d_{x_i}} = -\left(v_{T_{x_i}} + \frac{d_{y_{T_i}}}{2}\,\omega_i\right)\,\eta_{d_i}\,\rho_g\,d_c\,\frac{d_{y_{T_i}}}{\cos q_i}\cdot \left|\sin\left(q_i - \tan^{-1}\left(\frac{v_{T_{x_i}} + \frac{d_{y_{T_i}}}{2}\,\omega}{v_{T_{y_i}} + \frac{d_{y_{T_i}}}{2}\,\tan(q_i)\,\omega_i}\right)\right)\right| \cdot \sqrt{\left(v_{T_{x_i}} + \frac{d_{y_{T_i}}}{2}\,\omega_i\right)^2 + \left(v_{T_y} + \frac{d_{y_{T_i}}}{2}\,\tan(q_i)\,\omega_i\right)^2}, \tag{4.4}$$

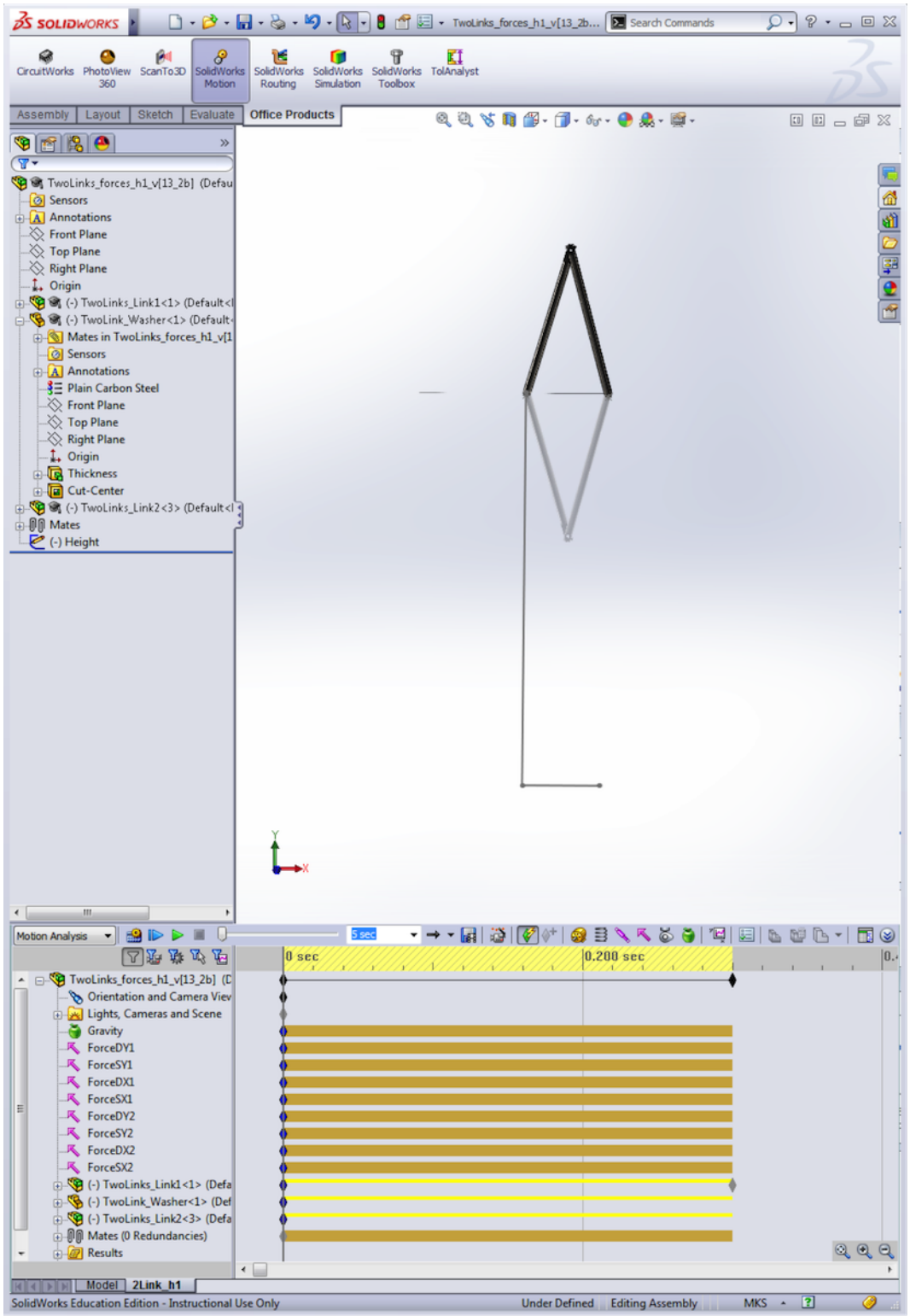

Figure 4.6: The double link assembly in SolidWorks

$$F_{d_{y_i}} = -\left(v_{T_{y_i}} + \frac{d_{y_{T_i}}}{2}\,\tan(q_i)\,\omega_i\right)\,\eta_{d_i}\,\rho_g\,d_c\,\frac{d_{y_{T_i}}}{\cos q_i}\cdot \left|\sin\left(q_i - \tan^{-1}\left(\frac{v_{T_{x_i}} + \frac{d_{y_{T_i}}}{2}\,\omega_i}{v_{T_{y_i}} + \frac{d_{y_{T_i}}}{2}\,\tan(q_i)\,\omega_i}\right)\right)\right| \cdot \sqrt{\left(v_{T_{x_i}} + \frac{d_{y_{T_i}}}{2}\,\omega_i\right)^2 + \left(v_{T_{y_i}} + \frac{d_{y_{T_i}}}{2}\,\tan(q_i)\,\omega_i\right)^2}, \tag{4.5}$$

$$F_{s_{x_i}} = -\frac{\mathbf{v}_{E_{x_i}}}{|\mathbf{v}_{E_{x_i}}|}\,\eta_{h_i}\,g\,\rho_g\,d_{y_{T_i}}^2\,d_c, \tag{4.6}$$

$$F_{s_{y_i}} = -\frac{\mathbf{v}_{E_{y_i}}}{|\mathbf{v}_{E_{y_i}}|}\,\eta_{v_i}\,(d_{y_{T_i}}/L)^{\lambda_i}\,g\,\rho_g\,\frac{\pi\,{d_c}^2}{4}\,\frac{d_{y_{T_i}}}{\cos q_i}. \tag{4.7}$$

The coefficients η_{d_i}, η_{h_i}, η_{v_i} and λ_i are constants that depend on the properties of the granular material, and on the angle of impact (Chapter 3). For the simulation of the resistant force, F_{r_i} the values of the four constants were estimated using Table 4.3, which is similar to the values suggested in Table 3.2 in Chapter 3. To approximate the necessary values for link 2, where $q_2 \simeq 15$ is positive (as in the case of the single link analysis), the expressions depend on the impact angle and ρ_g used were those corresponding to angle $\alpha_2 = \pi/2 - q_2 \simeq 75^o$. For link 1, $q_1 \simeq -15^o$, which is a negative angle from the single link study, and $\alpha_1 = pi/2 - abs(q_1)$ the row for $\alpha = 15^o$ in Table 3.2 proved to be more useful. Due to the changes in the settings of the system, adjustments for the expression proposed were necessary. The most important adjustments come in the form of changing the multiplying coefficients in the expressions due to the reaction that exists between the two links. Other slight modifications were due to rounding or adjusting the horizontal static drag coefficient, η_h. When this coefficient was adjusted, the other three η coefficients also changed since they are expressed in terms of η_h. The calculated values that were substituted for the coefficients in the F_{r_i} expression are given in Table 4.4.

A few remarks considering these expressions are necessary. The β coefficient in the η_{h_1} used for $v1_{01}$ expression appears because the impact angle is significantly ($\simeq 12\%$) larger than the impact angle $\alpha = 15^o$ and there is therefore a change of expression from $\alpha = 15^o$ to $\alpha = 25^o$. In this case,

	$v_{T_y}(0)$ (m/s)	η_h	η_d	η_v	λ
Link 1	2.60	$\beta \cdot \frac{\rho_g \alpha_1^2}{10}$	$\frac{3}{2}\eta_h \alpha_1$	$1.55\eta_h \alpha_1^3$	$\frac{\rho_g}{\alpha_1} \cdot 10^{-4}$
	2.29	$\frac{\rho_g \alpha_1^2}{10}$	$\frac{3}{2}\eta_h \alpha_1$	$1.55\eta_h \alpha_1^3$	$\frac{\rho_g}{\alpha_1} \cdot 10^{-4}$
	1.60	$\frac{\rho_g \alpha_1^2}{10}$	$\frac{3}{2}\eta_h \alpha_1$	$1.55\eta_h \alpha_1^3$	$\frac{\rho_g}{\alpha_1} \cdot 10^{-4}$
Link 2	2.60	$1.25 \cdot \frac{\rho_g}{\alpha_2^2 \cdot 100}$	$\frac{2}{3}\eta_h \alpha_2$	$5\eta_h \alpha_2^3$	$\rho_g \alpha_2 \cdot 10^{-4}$
	2.30	$1.25 \cdot \frac{\rho_g}{\alpha_2^2 100}$	$\frac{2}{3}\eta_h \alpha_2$	$5.25\eta_h \alpha_2^3$	$\rho_g \alpha_2 \cdot 10^{-4}$
	1.61	$1.25 \cdot \frac{\rho_g}{\alpha_2^2 100}$	$\frac{2}{3}\eta_h \alpha_2$	$5.25\eta_h \alpha_2^3$	$\rho_g \alpha_2 \cdot 10^{-4}$

Table 4.3: The expressions for resistance force coefficients η_h, η_d, η_v, λ

$\beta = (25 - 15)/q_1 = 0.6$. The same adjustment is not needed for link 2 with $q_2 = 13^o$, since there is no change in expression suggested from $q = 5^o$ to $q = 15^o$ for η_{h_2} in Table 3.2.

4.3.2 Simulation Results and Analysis

The impact was simulated in the Motion Analysis mode in SolidWorks. The resistance forces F_{R_i} became active when $d_{y_{T_i}} = 0$ (see Appendix G) and the velocity reached the initial velocity set in the experiments. The values for η_{h_i}, η_{d_i}, η_{v_i} and λ_i are given in Table 4.4. The simulation calculations were performed at 10000 frames/s and with 10^{-6} m accuracy and the gravity in the y direction was turned on.

	$v_{T_y}(0)$ (m/s)	η_h	η_d	η_v	λ
Link 1	2.60	8	13	33	0.125
	2.29	9	19	33	0.13
	1.60	10	19	38	0.14
Link 2	2.60	11.8	10	137	0.205
	2.30	12.5	10.8	144	0.21
	1.61	13	12	145	0.22

Table 4.4: The values for the resistance force coefficients η_h, η_d, η_v, λ

Displacement and Velocity Simulation Results and Analysis

The Motion Analysis was run for three initial velocities and the angles of the two links with the vertical were the same as in the experimental setup (see Table 4.1). The colored curves in Fig. 4.7 show the simulation results for the immersion of the tip point of link 1 Fig. 4.7 (a) and link 2 Fig. 4.7 (b) conditioned by the initial velocity.

	t_s (s)	d_{yT} (m)	$v_{yT}(0)$ (m/s)
Link 1	0.024	0.034	2.62
	0.025	0.030	2.29
	0.027	0.026	1.60
Link 2	0.025	0.036	2.61
	0.026	0.032	2.29
	0.027	0.025	1.61

Table 4.5: The simulation results for the two end points of the double kinematic chain

For each link, the phenomenon normally associated with an impact with granular matter appeared. The final displacement corresponding to zero value for the vertical linear velocity of the end point T_i increased with initial velocity, but the stopping time for both links decreased with increasing initial velocity. The displacement in time for each link during simulations was very similar to the average displacement in time observed in the experimental trials (black curves in Fig. 4.7). The values for the simulation results are displayed in Table 4.5. For

$$\epsilon_i = \left| \frac{de_{y_{T_i}}(t_s) - ds_{y_{T_i}}(t_s)}{de_{y_{T_i}}(t_s)} \right|, \tag{4.8}$$

$i = 1, 2$, de_{y_T} is the final displacement for experiments, and ds_{y_T} is the final displacement for simulation analysis when $v_{y_T}(t_s) = 0$.

The relative error between the simulation results and the experimental final displacement was calculated using Eq. 4.8 and is shown in Table 4.6.

The relative errors between the experiments and the simulation results for depth are small, with the highest errors being for $v2_{02}$. As in the case of the free link impact, there is a significant

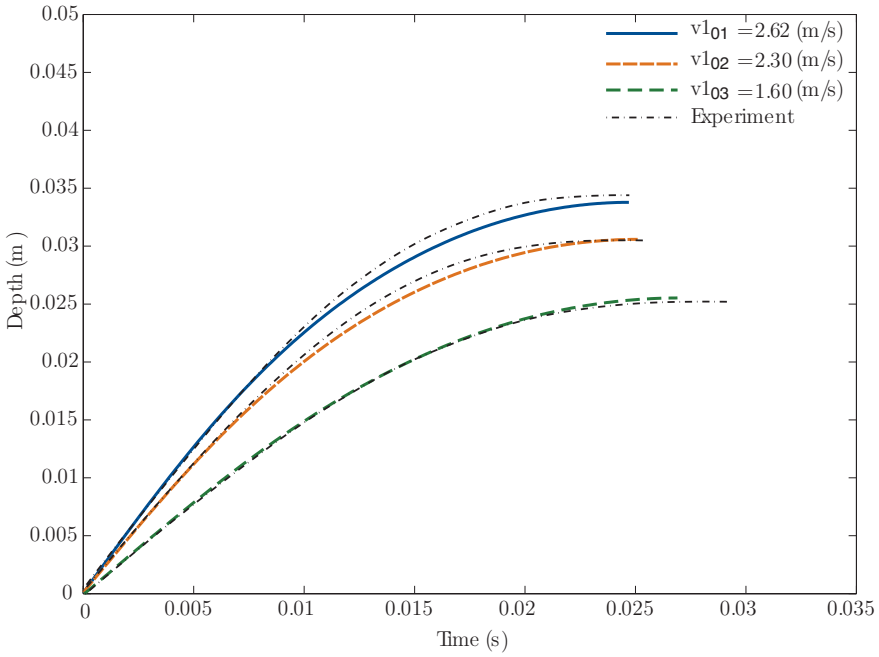

(a) Displacement in time of the tip point T_1 for Link 1

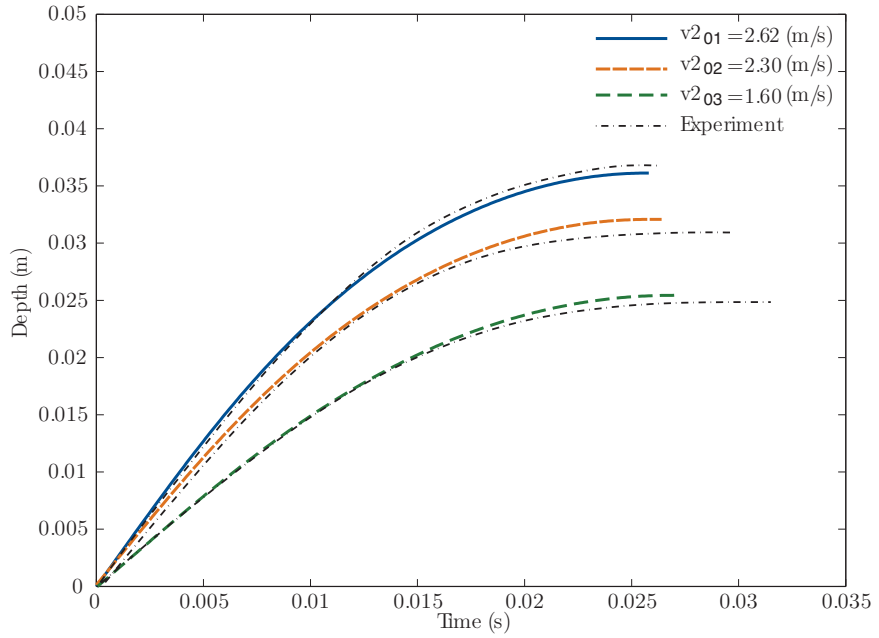

(b) Displacement in time of the tip point T_2 for Link 2

Figure 4.7: Simulation and experimental impact results for the penetration displacement of a double kinematic chain with two contact points: (a) for link 1, and (b) for link 2

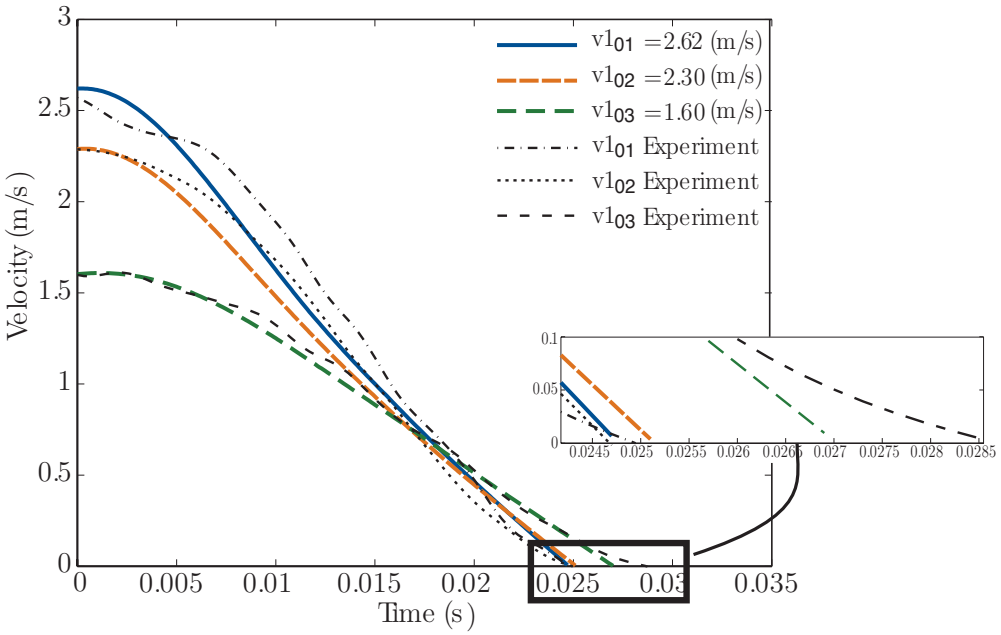

(a) Velocity for Link 1

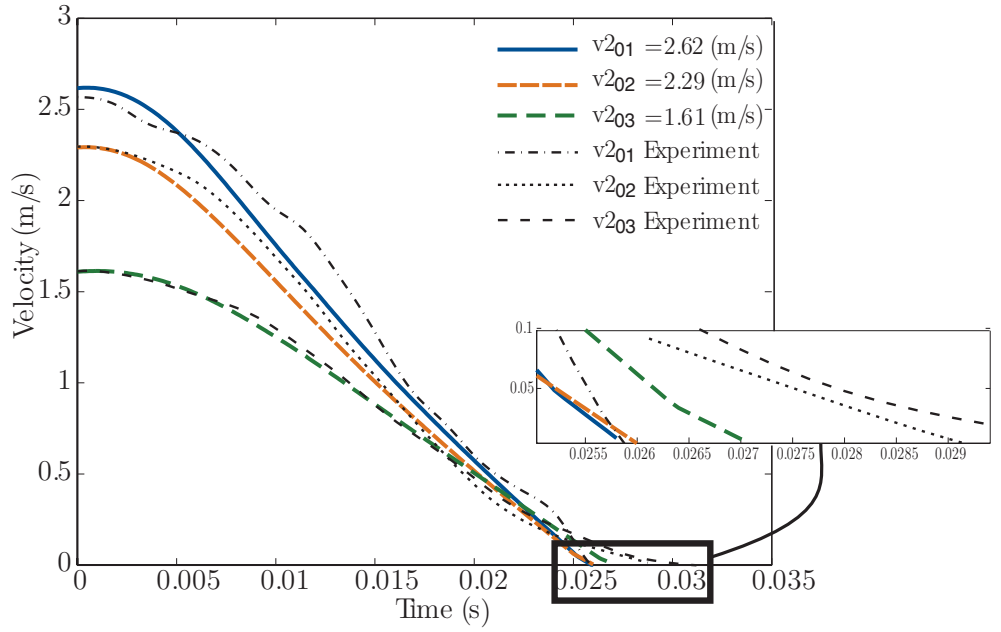

(b) Velocity for Link 2

Figure 4.8: The simulation and experimental velocity during penetration phase of the impact of a double kinematic chain with granular matter: (a) for link 1, (b) for link 2

	$v_{y_T}(0)$ (m/s)	ϵ_i (%)
$i = 1$ for Link 1	2.62	1.77
	2.29	0.61
	1.60	1.31
$i = 2$ for Link 2	2.60	1.77
	2.29	3.72
	1.61	2.39

Table 4.6: Relative error between the experimental and simulation results for penetration depth

difference in stopping times between the simulation and the experimental values. This can be observed in the displacement graphs in Fig. 4.7 (a) and (b), as well as in the velocity graphs in Fig. 4.8 (a) and (b).

Resistance Force Simulation Results and Analysis

The SolidWorks results feature was used to extract the reaction forces for the four components of the resistance force (Eq. 3.17 - 3.20) for the three cases considered in this section. Appendix H contains the graphs of Fd_{x_i}, Fd_{y_i}, Fs_{x_i}, Fs_{y_i} as they act on the rigid body during the immersion phase. The graphs show how the horizontal and vertical dynamic forces, as well as the horizontal and vertical static forces, depend on both the initial velocity and impact angle of each link.

The magnitude of the dynamic force $F_{d_i} = \sqrt{F_{d_{x_i}}^2 + F_{d_{y_i}}^2}$ is displayed in Fig 4.9. For all three initial velocities, the dynamic force increased with time until it reached a maximum and then decreased. The time at which the dynamic force reached its maximum value was not constant with the initial velocity ($t1_{s_1}$ = 7 ms, $t2_{s_1}$ = 7.3 ms,$t1_{s_2}$ = 7.2 ms,$t2_{s_2}$ = 7.1 ms, $t1_{s_3}$ = 9.1 ms, and $t1_{s_1}$ = 8.7 ms). The magnitude of the dynamic force increased and reached its maximum faster with increasing initial velocity for each link (F_{d_1} = 3.5 N at $v1_{01}$, F_{d_1} = 3.25 N at $v1_{02}$, F_{d_1} = 1.4 N at $v1_{03}$, F_{d_2} = 2.5 N at $v2_{01}$, F_{d_2} = 1.7 N at $v2_{02}$, F_{d_2} = 0.85 N at $v2_{03}$). At higher velocities, v_{01} = 2.6 m/s and v_{02} = 2.30 m/s, the maximum values for the magnitude of F_d were very close. An interesting observation is that for link 2, F_d reached its maximum 0.1 ms faster at v_{02}. This can be explained by the $\epsilon = 3.72$ error in the displacement for the link at this velocity. Figure 4.9 also shows that at the end of the penetration phase ($v_{y_{T_i}}(t_s) = 0$ (m/s)), the vertical dynamic force reached zero. The different maximum dynamic force values for the two links is consistent with the

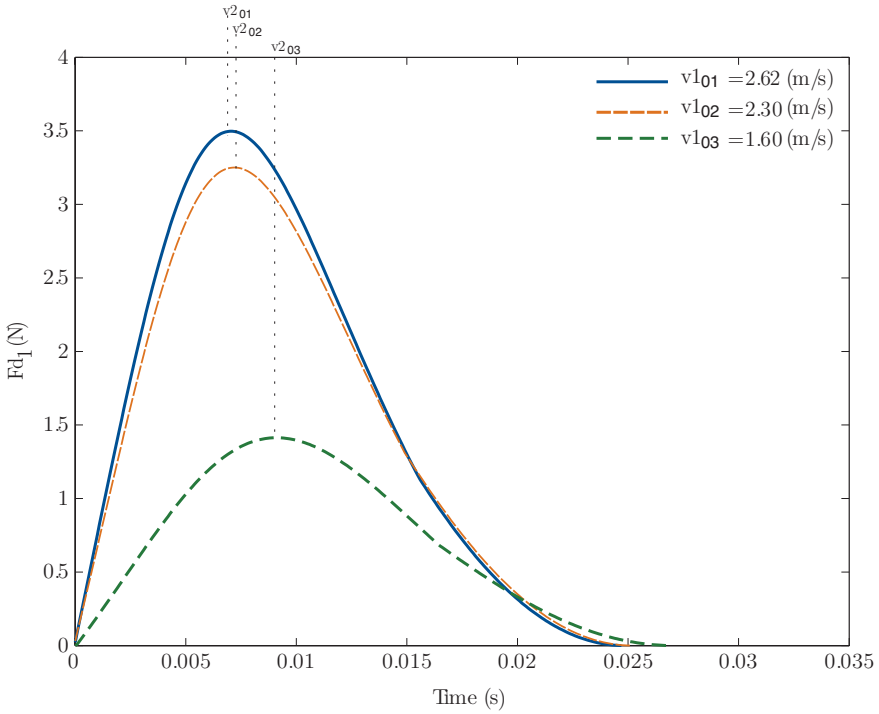

(a) The reaction of the dynamic force on Link 1

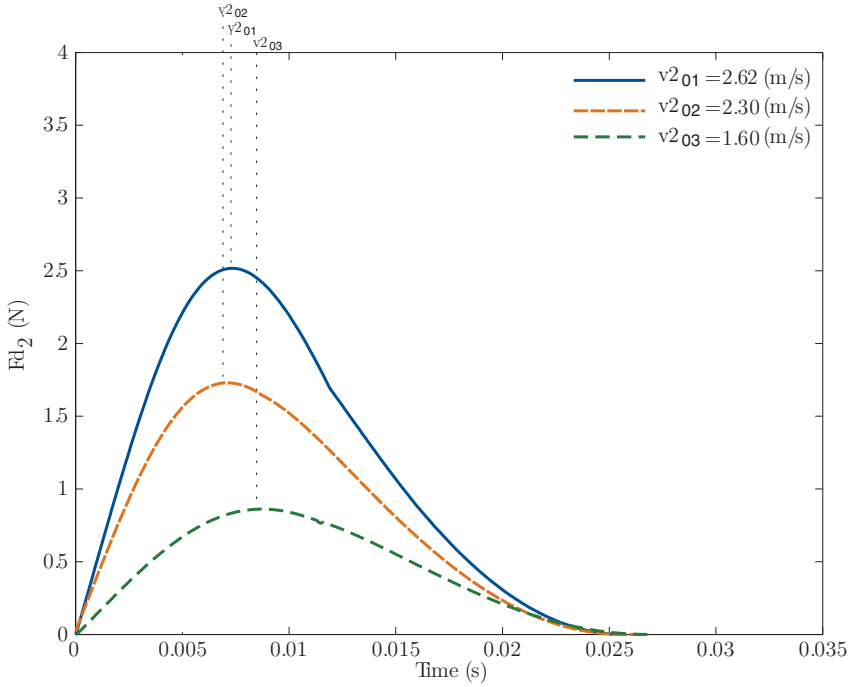

(b) The reaction of the dynamic force on Link 2

Figure 4.9: The dynamic reaction force during penetration phase on the impacting system: (a) for link 1, and (b) for link 2

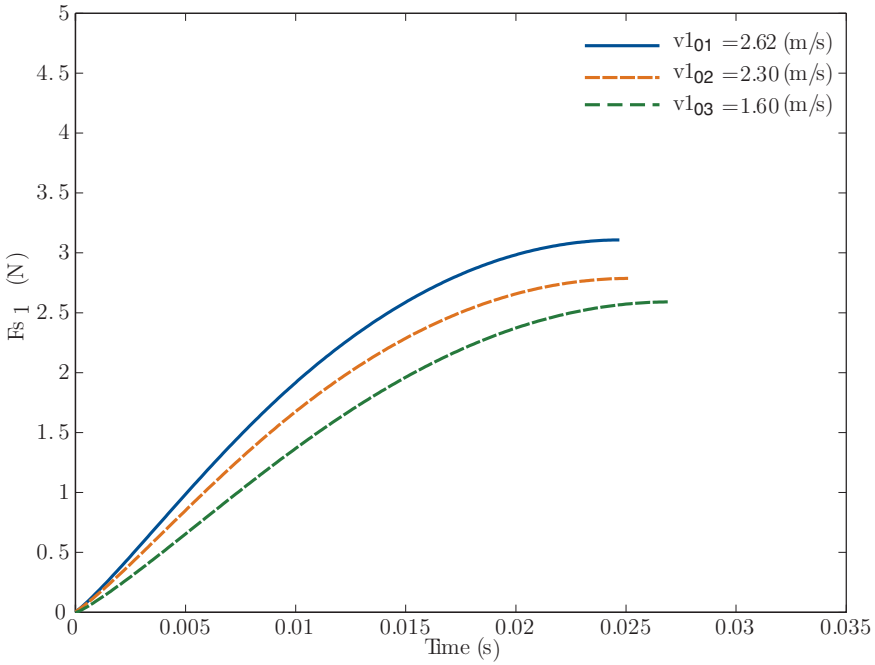

(a) The reaction of the static force on Link 1

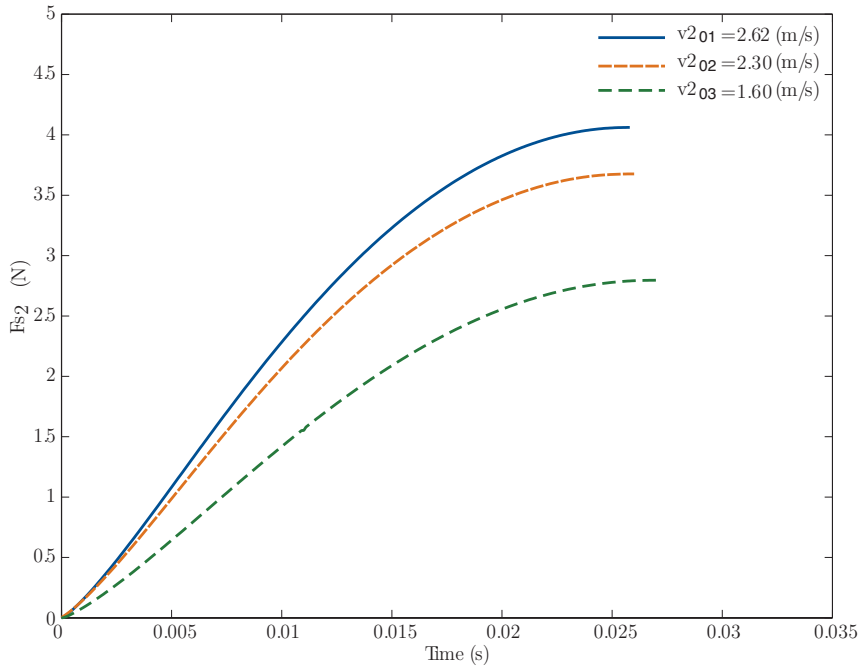

(b) The reaction of the static force on Link 2

Figure 4.10: The static force during penetration phase on the impacting system: (a) for link 1, and (b) for link 2

results obtained for the study of the oblique impact of a free link discussed in the previous chapter and shown in Fig. 3.29.

The magnitude of the static force, $F_{s_i} = \sqrt{F_{s_{x_i}}^2 + F_{s_{y_i}}^2}$ increased monolithically at a different slope with initial velocity until it tended to saturate at the end of the immersion (Fig. 4.10). Therefore at the end of the penetration phase, the static force at its maximum, which is expected since this term is the linear displacement dependent component of the resistance force. If for the dynamic force, the maximum values are higher for link 1, the magnitude for the static force will be higher for link 2 ($F_{s_1} = 3.1$ N at $v1_{01}$, $F_{s_1} = 2.8$ N at $v1_{02}$, $F_{s_1} = 2.6$ N at $v1_{03}$, $F_{s_2} = 4$ N at $v2_{01}$, $F_{s_2} = 3.7$ N at $v2_{02}$, $F_{s_2} = 2.8$ N at $v2_{03}$).

The total resistance force $F_{r_i} = \sqrt{(F_{s_{x_i}} + F_{d_{x_i}})^2 + (F_{s_{x_i}} + F_{d_{x_i}})^2}$ on each link is presented in Fig. 4.11. The resistance force increases with increasing initial velocity for each link. During the penetration, the resistance force will increase according to the dynamic force until this component reaches its maximum and then the resistance force will act more and more under the influence of the static force. The penetration phase ends with the resistance force having a magnitude equal to the static force. A similarity in behavior with the free link impact is again noticeable here. The curves in Fig. 4.11 are comparable with the results obtained for the resistance force of the free link and an oblique impact shown in Fig. 3.31 for the impact angles considered for the two links. The two links impact the granular surface at different angles $q_1 = -15^o$, corresponding to the impact angle for free link $\alpha = 15^o$ and $q_2 = 15^o$ for link 2 to $\alpha = 72^o$.

Figure 4.11 shows that the resistance force depends on the dynamic force for longer at higher initial velocities. This is also depicted in Fig. 4.12, which shows the instant at which the dynamic and static components interchange influences. For link 2, the dependence of the resistance force on the dynamic force with initial velocity is more pronounced (Fig. 4.12, (b)) and the dynamic force will exert an influence on the resistance force for longer at higher velocities. This is reversed at low velocities, where the displacement dependency will dominate longer. For link 1 (Fig. 4.12, (a)), the static force will prevail for longer than at higher velocities because for this link, the magnitudes of the dynamic force for $v1_{01}$ and $v1_{02}$ are so close in value and in appearance in time that the velocity dependence and displacement velocity will switch dominance almost at the same time.

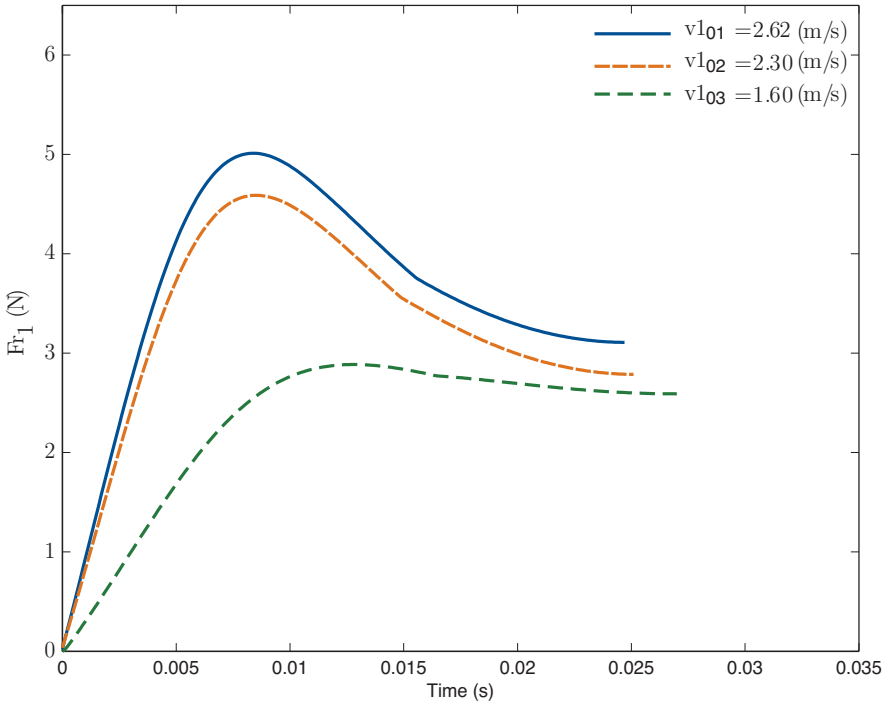

(a) The reaction of the resistance force on Link 1

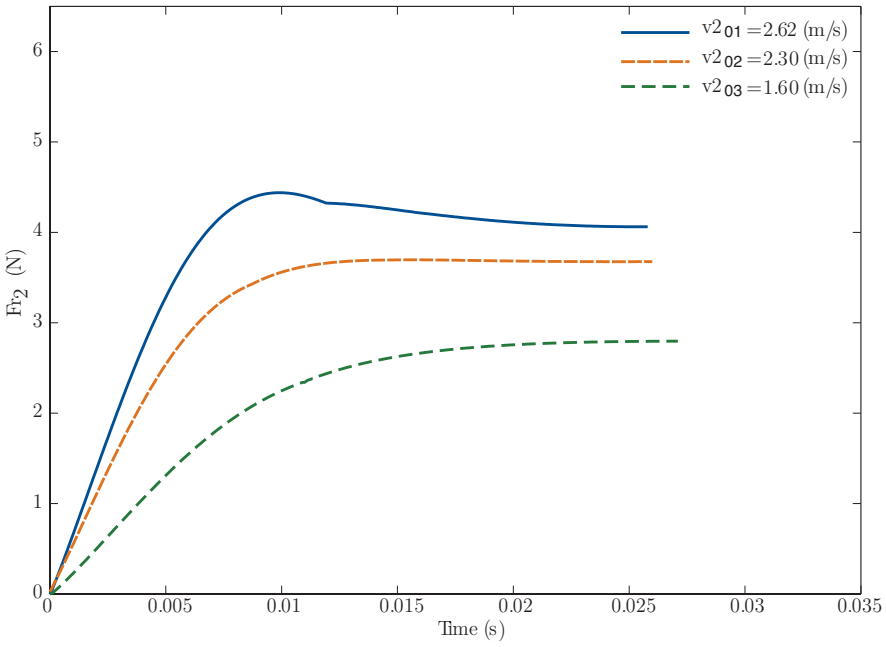

(b) The reaction of the resistance force on Link 2

Figure 4.11: The resistance force during penetration phase on the impacting system: (a) for Link 1with impact angle $q_1 = -15^o$, and (b) for Link 2 with impact angle $q_2 = 15^o$

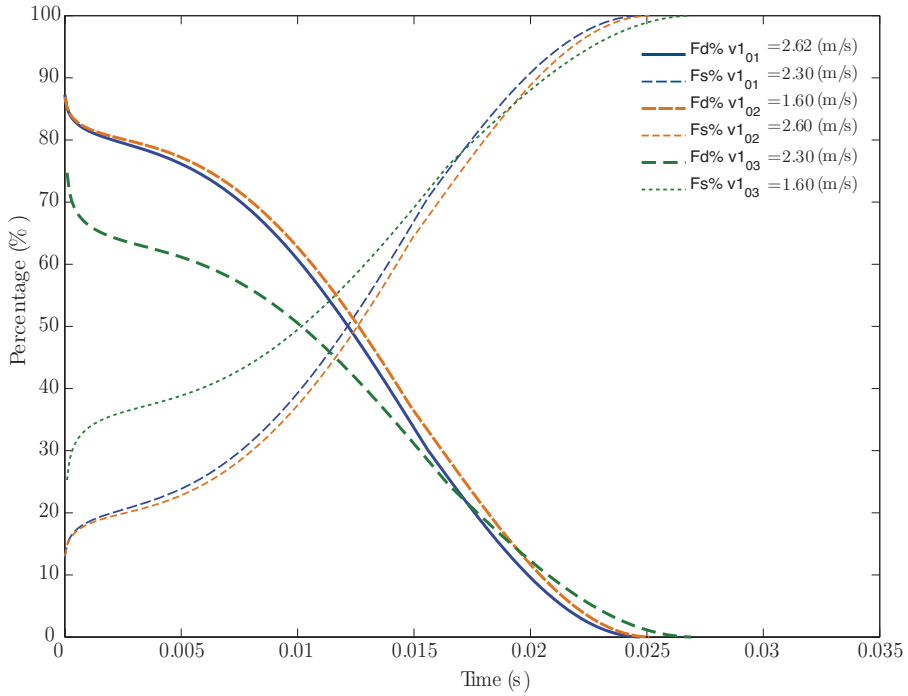

(a) The contribution of the dynamic and static reaction on Link 1

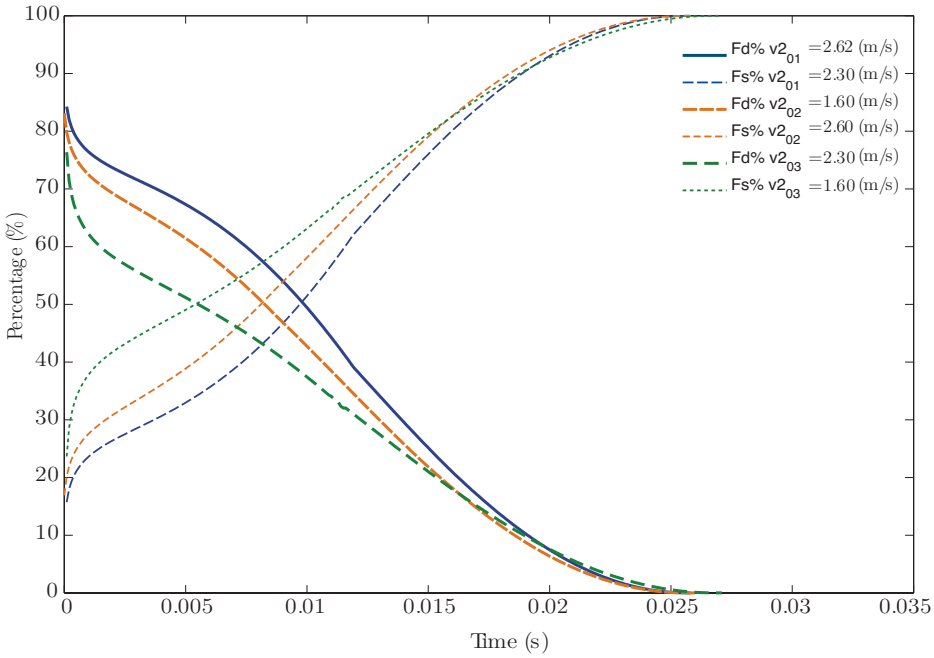

(b) The contribution of dynamics and static reaction on Link 2

Figure 4.12: Dynamic and static force percent out of the resistance force for a impact of a two-link kinematic chain with granular matter during the penetration phase: (a) for link 1, and (b) for link 2

Mechanical Energy Simulation Results and Analysis

The granular matter will react to the intrusion of the system with the resistance force, F_r discussed in the previous subsection. The system will release energy to the of granular matter environment to help the medium transition from exhibiting fluid-like to solid-like properties, thus halting the intruders. For

$$\Delta K.E._{\cdot i} = \frac{1}{2} m_i \, \Delta vi_{COM}^2 \, + \, \frac{1}{2} I_i \, \Delta\omega_i^2, \tag{4.9}$$

$$\Delta P.E._{\cdot i} = m_i \, g \, \Delta h_i, \tag{4.10}$$

$i = 1, 2$, m_i is the mass of each link, vi_{COM} is the velocity of the center of mass of each link, I_i is the mass moment of inertia with respect to the center of mass, ω_i represents the angular velocity of each link during impact, g is the gravitational acceleration and h represents the vertical displacement of the each link during impact. To calculate the change in energy, the first state, s_1 is considered to be the moment when the tip of the bar comes in contact with the surface of the granular matter, and the final state, s_2 is defined as the moment when the linear velocity of the tip of the rigid body reaches zero. Therefore $\Delta = s_2 - s_1$.

The mechanical energy will be dissipated according to a linear displacement dependent term, namely potential energy (Eq. 4.10), and a quadratic velocity dependent term, kinetic energy (Eq. 4.9). The kinetic energy results produced from the simulation for each link includes both linear and angular motion. The potential energy is determined for each link using a SolidWorks results feature.

Figure 4.13 shows how the kinetic energy that is dissipated into the granular matter during impact is higher with a higher initial velocity. The error in the kinetic energy released by the two links at each initial velocity is defined by $\epsilon = (K.E._{\cdot 1} - K.E._{\cdot 2})/K.E._{\cdot 1}$ and is presented in Table 4.7. This result shows that in terms of energy, the sign of the angle with the vertical is unimportant. Hence, $q_1 = |q_1| \simeq 15^o$. This conclusion is validated by the results for potential energy (Fig. 4.14). The potential displacement on the vertical axis for the potential energy can be calculated using the trigonometric function cosine, which is an even function. Thus, the two links should have an equal influence on the total energy released. The error in potential energy between link 1 and link

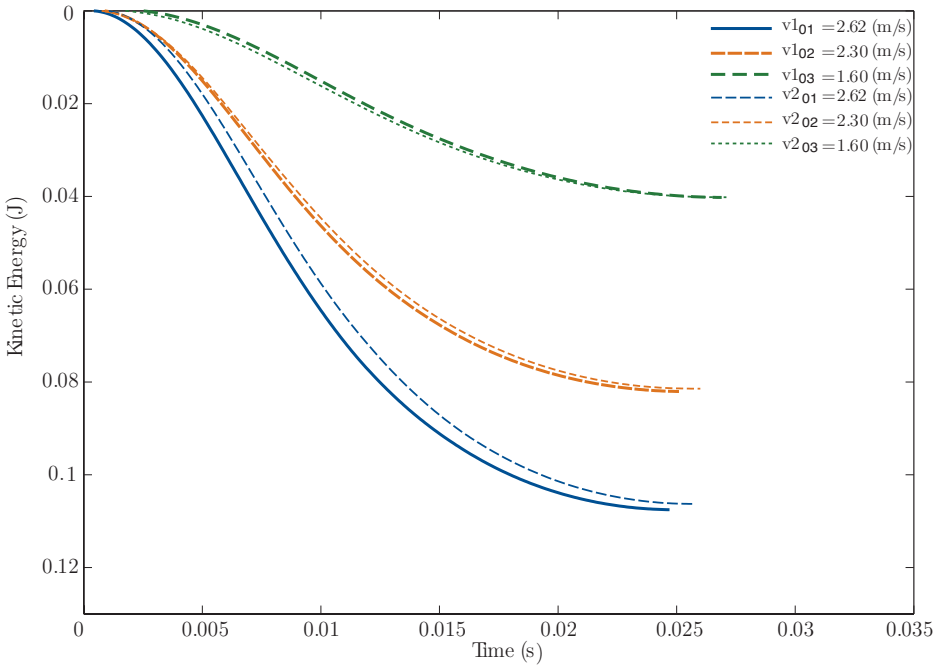

Figure 4.13: The kinetic energy dissipated to the granular environment during the penetration phase

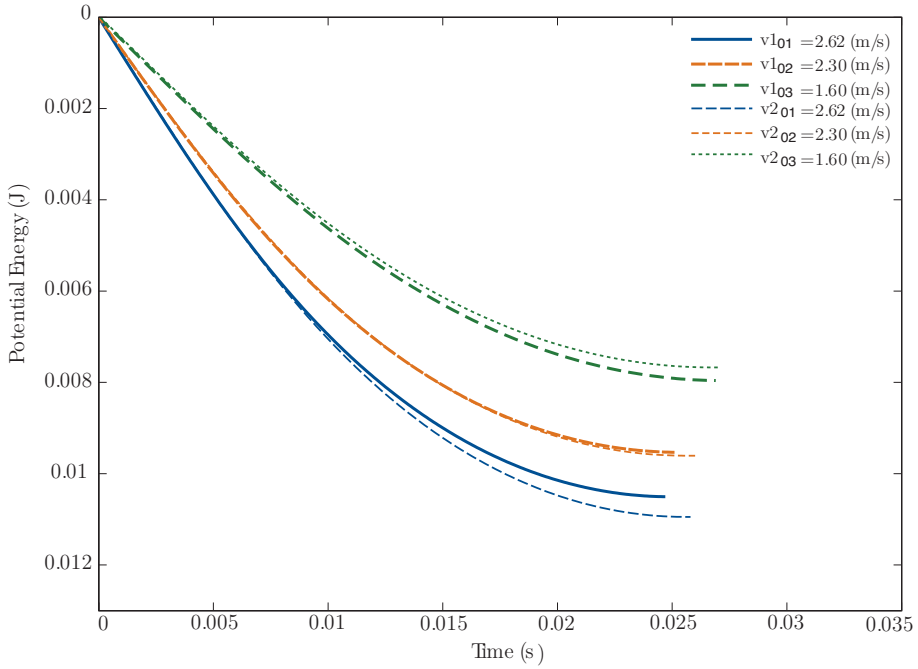

Figure 4.14: The potential energy dissipated to the granular environment during the penetration phase

2 (Table 4.7), comes from the errors in the final displacement between the two links, but also arises due to the slight difference in the value of the impact angle with the vertical.

	$v_{y_T}(0)$ (m/s)	ϵ_i (%)
K.E.	2.62	1.16
	2.29	0.7
	1.60	0.1
P.E.	2.60	-4.2
	2.29	-0.8
	1.61	3.2

Table 4.7: Relative error between the kinetic and potential energy for Link 1 and Link 2

The total energy dissipated to the granular medium by each link $\Delta E_i = \Delta K.E._i + \Delta P.E._i$ is shown in Fig. 4.15. The error between the two links in total energy dissipated stabilizes to 0.6% for all three initial velocities. The total energy released to the medium increases with initial velocity ($\Delta E = 0.24$ J at $v_{01} = 2.6$ m/s, $\Delta E = 0.18$ J at $v_{02} = 2.3$ m/s and $\Delta E = 0.10$ J at $v_{03} = 1.6$ m/s).

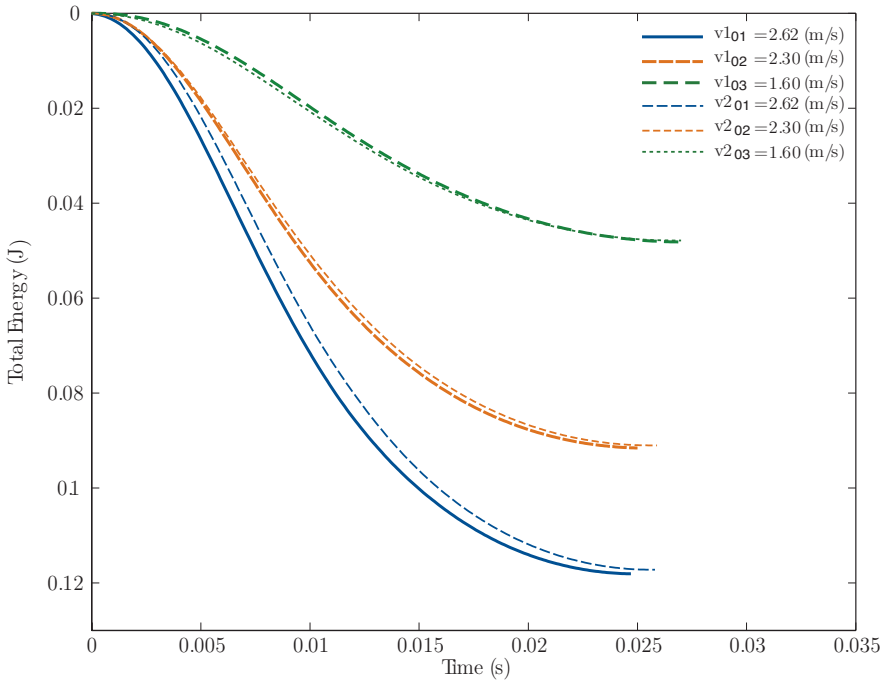

Figure 4.15: The total mechanical energy dissipated to the granular environment during penetration phase

The kinetic energy starts with a concave curvature, but then goes through an inflection point and changes curvature. Interestingly, the potential energy does not show the same tendency and so

will have a initial influence on the total energy values. However, due to the approximatively 10 time higher values for the kinetic energy, the potential energy will present a logarithmic like influence on the total energy while the kinetic energy will increase and come to dominate the energy dissipation trend (Fig 4.16). The lower the the velocity, the longer it will take for the percentage of kinetic energy to increase.

4.4 Conclusions

This chapter has presented both experimental and simulation measurements of the impact of a two link kinematic system with granular matter. The experiments showed that the system will stop faster with increasing initial velocity, but will immerse deeper into the volume. The analysis was performed for each link separately, each with its own contact point. The experimental system settings were utilized for the simulations and a model was created in SolidWorks. The series of resistance force components, both for quadratic velocity and for the linear displacement dependent variables, were used to simulate the impact as for the case of a free link impact with granular matter discussed in Chapter 3. Appropriate force coefficients η_h, η_d, η_v and λ expressions and values were proposed, and the expressions for these constants perfected for negative angles with the vertical. The errors between the simulation and experimental results were low, and the behavior consistent. The simulations also revealed the impact of the dynamic and static components on the resistance force and the percentage contribution of each. For increasing velocity, a slower shift in dominance from dynamic force to static force was both expected and demonstrated during the simulations. The resulting curves describe the progression of the dynamic and static forces and, in consequence of the resistance force, are consistent for each link when compared to the forces obtained for the single link impact angle model at the impact angles used in this study. The total mechanical energy for each link is preponderantly due to the kinetic energy for higher velocities, with the potential energy of the system released to the environment about being at the most 10 times smaller than the kinetic energy. Each link contributes about 50% to the total mechanical energy discharged to the environment for the system consisting of two identical links positioned at the same angle with the vertical.

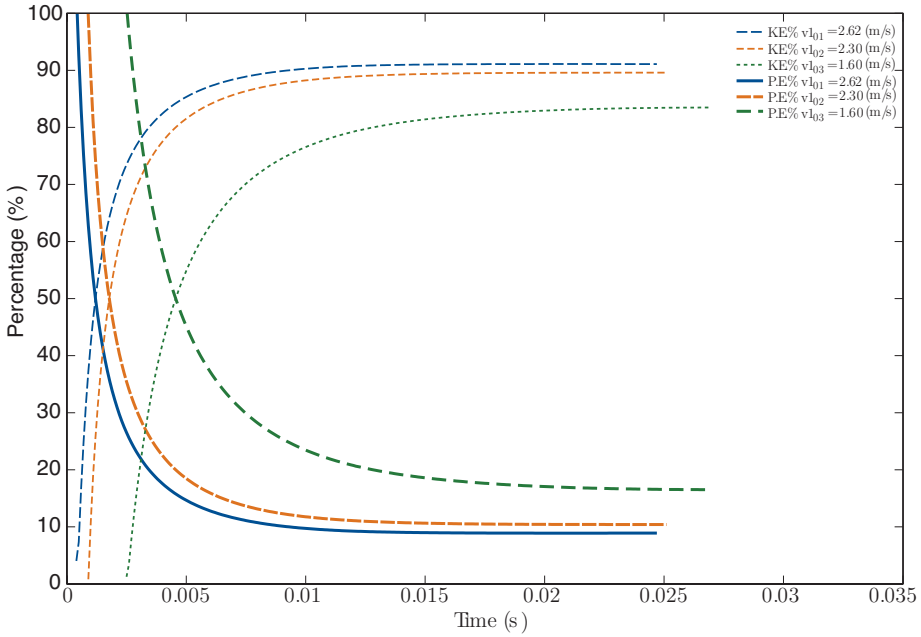

(a) The percentage of kinetic and potential energy that accounts the total energy dissipation for Link 1

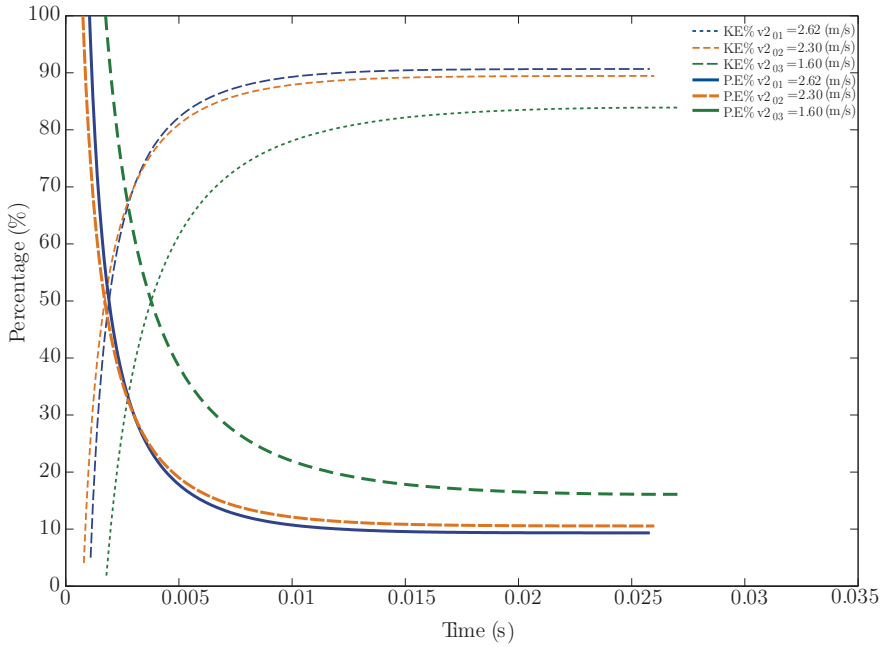

(b) The percentage of kinetic and potential energy that accounts for the total energy dissipation for Link 2

Figure 4.16: The contribution of the kinetic and potential energy to the total energy dissipation during the penetration phase by the system to the environment: (a) for link 1, and (b) for link 2

Chapter 5

Human Bipedal Impact with Granular Matter

This chapter presents a study of lower body human impact with two points of contact with granular matter. Experiments were designed to enable human subjects to impact granular matter at two initial velocities and the resulting real time position of the foot during jumps monitored. Final displacement, stopping time and velocity analysis were then recorded for two different initial velocities and a SolidWorks model for a human mannequin created. The force model discussed in the previous two chapters for the impact of a free link and a two link kinematic chain were then applied to simulate the bipedal impact with granular matter. Final displacement and velocity analysis were performed and the results are reported in this chapter.

5.1 Model of Human Bipedal Impact

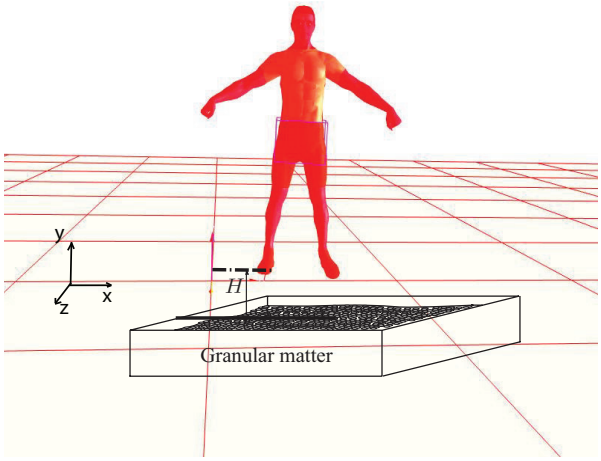

Figure 5.1: The human model coordinates

The human model developed for this study is considered as a multi-link kinematic chain. Both for simulations and experiments, the human motion is in 3D (Fig. 5.1). The positive x axis and its attached unit vector $\mathbf{\imath}$ is defined along the shoulders. The positive y axis (with the $\mathbf{\jmath}$ unit vector) is vertically upwards, and the positive z axis (with the $\mathbf{k}$ unit vector attached) is perpendicular coming out of the chest. The focus of this study was on the vertical and horizontal motion, so the analysis of the motion of interest was treated as being restricted to a two axis reference frame.

The quantities measured through experiments and simulation were the depth of penetration of the foot into the granular matter and the stopping time. The penetration was considered to start when the foot reaches the granular surface and the displacement were zero and the penetration phase ended when the vertical velocity of the foot in the sand was zero.

The force model used was based on the model described in chapter four that was validated for an impact with two contact points. In the case of human bipedal motion, the contact point at impact is the sole of the foot. Due to the difference in shape of the intruder for each subject, adjustments to the model were necessary. The frictional resistance force, F_r for a human foot sinking into a granular bed presents a linear displacement dependency, a static resistance force and a dynamic rate-dependent force. Therfore,

$$\mathbf{F_r} = \mathbf{F_d} + \mathbf{F_{s_h}} + \mathbf{F_{s_v}}, \tag{5.1}$$

$$\mathbf{F_d} = -\frac{\mathbf{v}_E}{|\mathbf{v}_E|}\,\eta_d\,\rho_g\,A_r\,\mathbf{v}_E\cdot\mathbf{v}_E = -\mathbf{v}_E\,\eta_d\,\rho_g\,A_r\,|\mathbf{v}_E|, \tag{5.2}$$

$$\mathbf{F}_{sh} = -\frac{\mathbf{v}_{E_h}}{|\mathbf{v}_{E_h}|}\,\eta_h\,g\,\rho_g\,d_{yT}^2\,f_s = \left[-\text{sign}(v_{E_h})\,\eta_h\,g\,\rho_g\,d_{yT}^2\,f_s\right]\,\mathbf{\imath}, \tag{5.3}$$

$$\mathbf{F}_{sv} = -\frac{\mathbf{v}_{E_v}}{|\mathbf{v}_{E_v}|}\,\eta_v\,(d_{yT}/l_l)^\lambda\,g\,\rho_g\,V = \left[-\text{sign}(v_{E_v})\,\eta_v\,(d_{yT}/l_l)^\lambda\,g\,\rho_g\,V\right]\,\mathbf{\jmath}. \tag{5.4}$$

where l_l is the length of the tibia in m, f_s is the foot size of the human subject in m, ρ_g is the density of the granular medium as a function of the density of the grains and the packing fraction. Velocity $\mathbf{v}_E$ is the linear velocity vector of ankle in m/s, with v_{Ex} the horizontal component of the velocity $\mathbf{v}_E$ and v_{Ev}, the vertical component of the velocity of $\mathbf{v}_E$. The term A_r represents the reference area of the plunged rigid body in m^2. Since in this model, the foot was the only part of the body immersed into the granular media, the reference area was approximated by the shape of a rectangle with length of the foot size and width of the penetration depth d_{yT} (see Fig. 5.2).

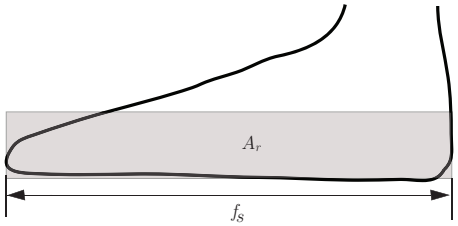

Figure 5.2: The human foot reference area

For the model in this study, the expression for the reference area is:

$$A_r = f_s \frac{d_{yT}}{\cos q} \left| \sin \left(q - q_m \right) \right|, \tag{5.5}$$

$$q_m = \tan^{-1} \left(\frac{v_{Eh}}{v_{Ev}} \right), \tag{5.6}$$

where q is the impact angle with the horizontal and q_m is the moving angle (see Fig. 3.14) of the intruder. The volume V of the immersed rigid body was also calculated in terms of the immersion angle:

$$V = f_s \, w_s \, \frac{d_{yT}}{\sin q}, \tag{5.7}$$

where w_s is the approximate width of the foot in m (see Fig. 5.3).

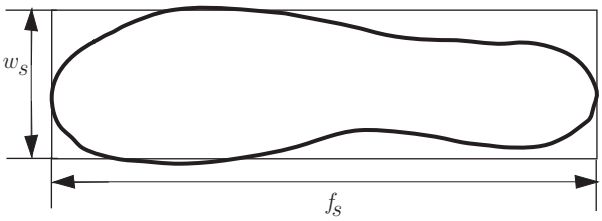

Figure 5.3: The human sole approximate area

5.2 Experiments for a Human Jumping Onto Granular Matter

5.2.1 Experimental Setup

For this study, kinematic data was collected for the entire body using a 3D motion capture system (Motion Realty, Inc from the Motion Capture Laboratory of Auburn University). The motion capture system utilized six 180Hz digital cameras with processing and pattern recognition

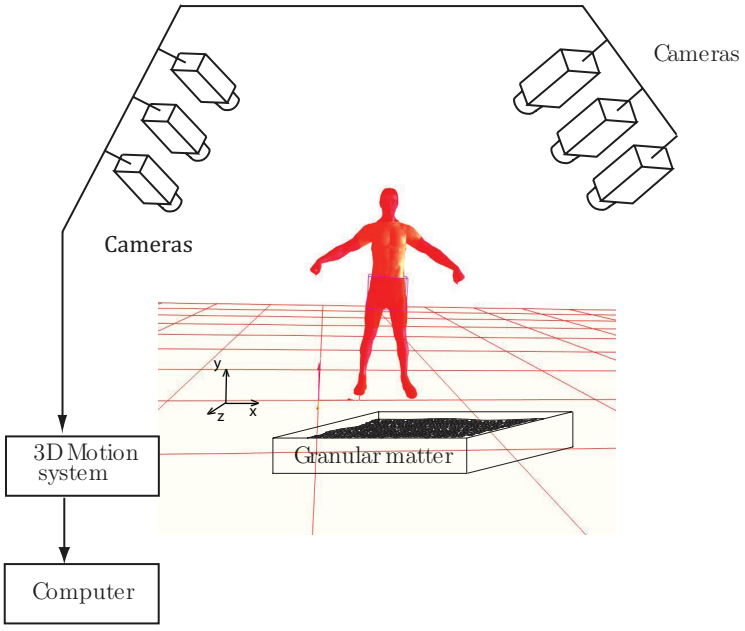

Figure 5.4: The motion capture system setup

capabilities (Fig. 5.4). Each camera recorded the planar motion of a series of reflective markers in a virtual volume within which the cameras could detect the position of the center of each marker to within 1/10th of a pixel. The volume covered by the cameras was $2.56 \times 2.6 \times 2.6$ m and the image produced by the cameras was 640×640 pixels, so for a camera magnification factor 2, the results were accurate to 0.001 m. The 3D motion system (Fig. 5.5) received the 2D coordinates from each camera and returned the 3D coordinates of all markers in the volume, after which they were transmitted to the PC. The system required regular calibration, both for fixed points and random points in the volume for accurate capture. The recorded total error was maintained at approximatively 0.1 pixels to ensure a consistent accuracy rate.

Thirty-eight high reflective markers were placed at specific locations on the human subject (see Fig. 5.5). Using specific body dimensions (height, weight, and shoe size) a 3D graphic model (Appendix I) was created through a scaling operation.The Motion Realty software displays a real-time view of the model as the human subject performs specific activities and collects nearly instantaneous information that is then stored and can be recalled at a later time.

The same system has been used for analyzing and improving swing techniques for high-school baseball players [46, 47], thus confirming its utility. An alternative way of validating the use of this

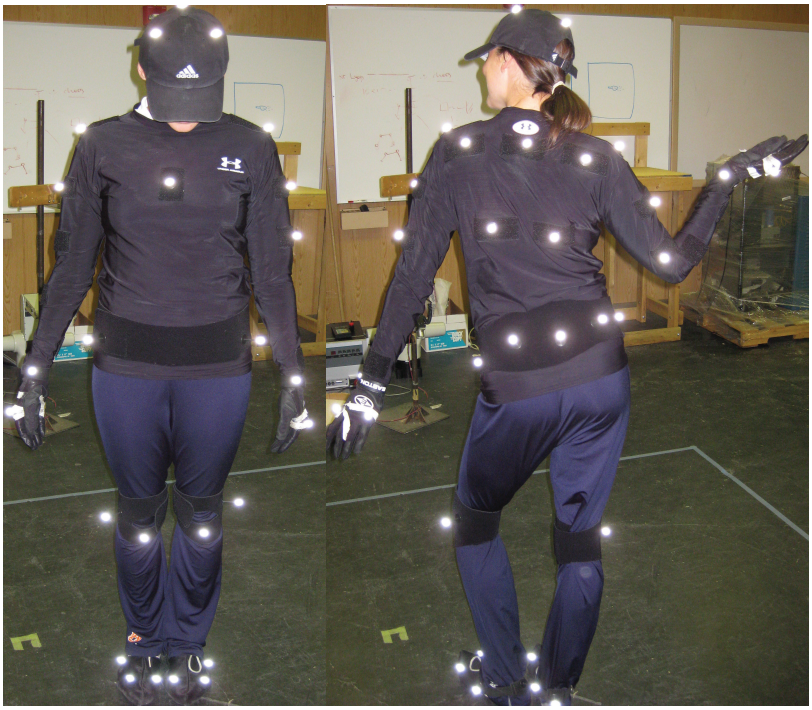

Figure 5.5: The placement of the 38 markers on the human subject

system for the purposes of this study was by analyzing the path of the foot during capture for two different initial velocities (see Fig. 5.6). A clear difference ($d_1 > d_2$) was observed in the burrowing depths, d_1 and d_2, for jumps from two different heights, h_1 and h_2, respectively.

The human subjects jumped onto a volume of fine sand (Quikrete 1961-52) in a box of dimensions $1.00 \times 0.60 \times 0.15$ m (L $\times$ W $\times$ H). The dimensions of the container were sufficient for the Jansen effect to be negligible. The box is positioned in the center of the virtual volume seen by all six cameras. Before each capture, the sand was stirred and leveled to eliminate history and maintain consistent packing. Five male subjects ($m = 75.35 \pm 0.568$ kg and $h = 1.78 \pm 0.032$ m) volunteered for this study. The participants did not report any previous leg injuries and all wore running shoes. Four participants reported themselves to be right handed and one left handed. The results obtained in Chapter 4 revealed no significant difference between the impacts of each of the two identical links with granular matter. Thus, the analysis of a single foot was deemed is sufficient for the purposes of this experiment. The data studied in here is for the non-dominant leg (four for the left and one for the right leg). Before each jump, reference data was collected to record the position of the surface relative to the origin of the capture volume. Each participant was instructed

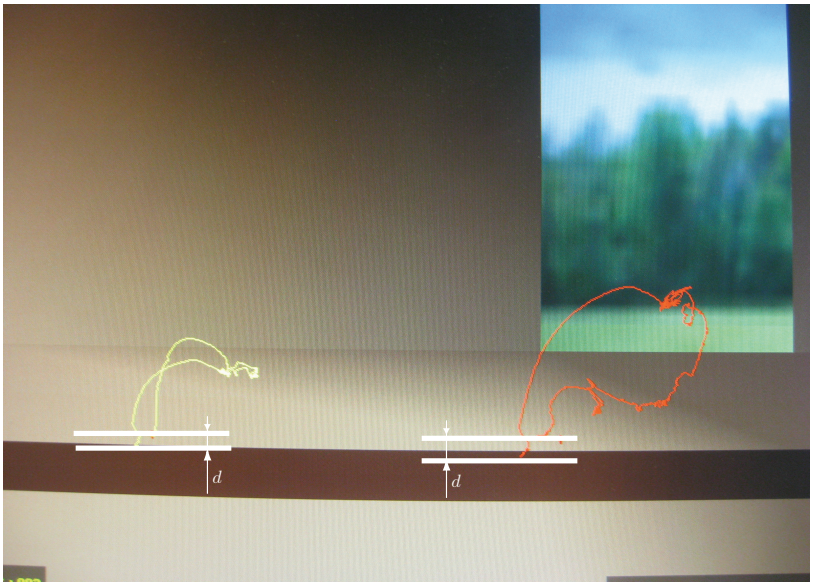

Figure 5.6: The foot path during capture for two initial velocities

in how to jump off the platform, to ensure the technique remained consistent throughout. The subjects steps off the platform and lands with both feet at the same time.

5.2.2 Experiment Results

For each platform height, the subjects performed five jumps. For each jump the position data was collected for the entire body, but the marker attached to the ankle was especially closely monitored. The impact data extracted was considered from the point of zero displacement of the ankle with respect to the reference data collected before the jump, up to the point the linear vertical velocity of the ankle joint becomes zero.

Table 5.2.2 presents the mean of all the captured stopping times for the impacts (the time from zero displacement to zero vertical linear velocity), t_s, the displacement during impact, d_y, and the initial velocity, $v_0 i$ (where $i = 1, 2$) for one contact point for each subject. The mean impact data extracted for each subject (Appendix J) revealed that the faster the impact velocity, the more rapidly the immersion of the subject's foot terminates, the deeper the resulting crater. Figure 5.7 shows that each subject registered higher final displacements (Fig. 5.7 (a)) and shorter stopping times (Fig. 5.7 (b)) with increasing of initial velocity.

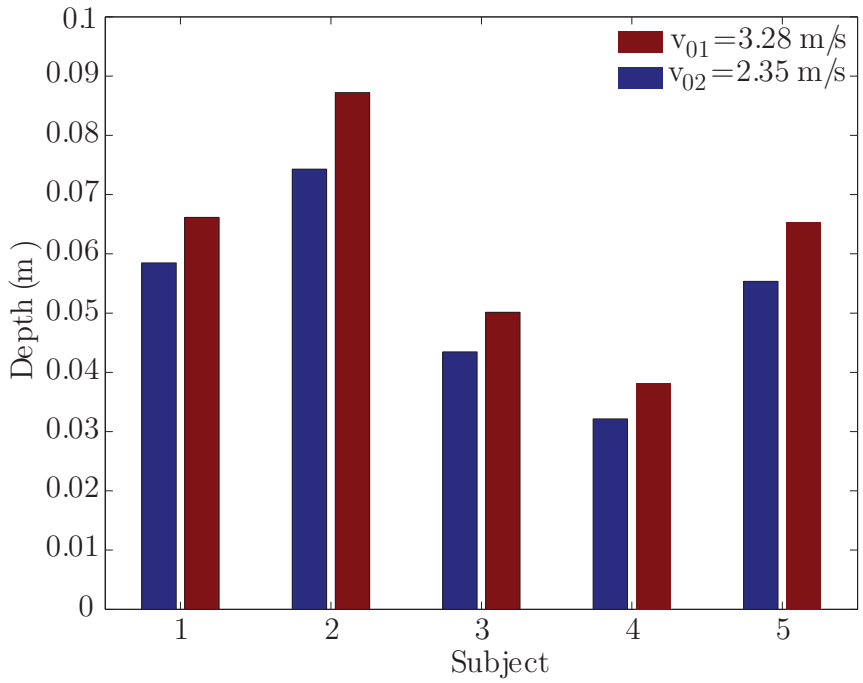

(a) Final depth with initial velocity per subject

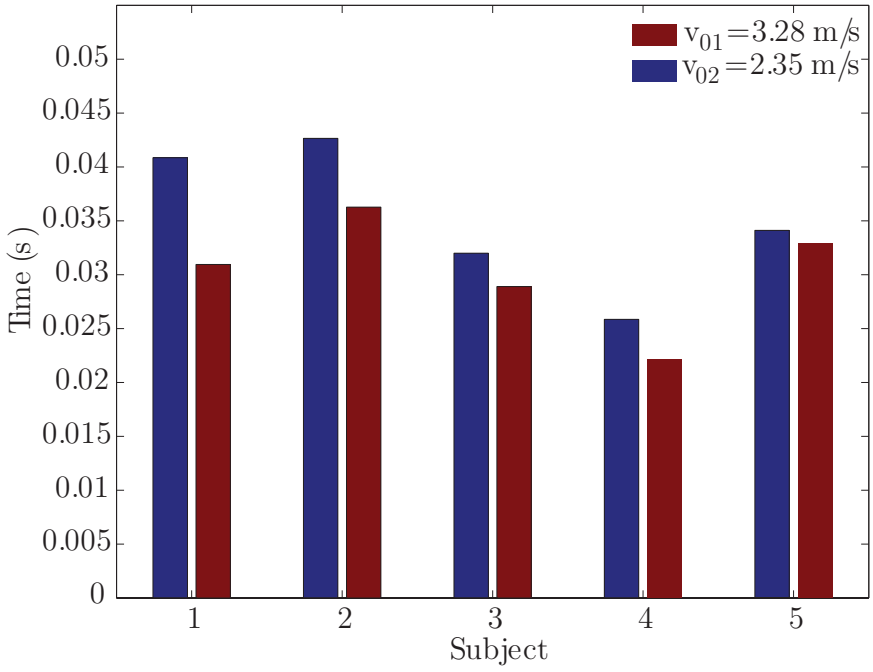

(b) Stopping time with initial velocity per subject

Figure 5.7: Average experimental impact results per subject: (a) depth for the two initial velocities, and (b) stopping time for the two initial velocities

	t_s (s)	d_y (in)	$v_0(0)$ (in/s)
	0.031 ± 0.002	0.07 ±0.006	3.49 ± 0.098
	0.036 ± 0.002	0.09 ± 0.005	3.48 ± 0.111
h_1	0.029 ± 0.022	0.05 ±0.005	2.93 ± 0.048
	0.022± 0.001	0.04 ± 0.000	3.35± 0.09
	0.032 ± 0.002	0.07 ±0.006	3.16 ± 0.32
	0.041 ± 0.002	0.059 ±0.005	2.31 ± 0.067
	0.042 ± 0.005	0.075 ± 0.008	2.34 ± 0.099
h_2	0.032 ± 0.001	0.04 ± 0.003	2.36 ± 0.082
	0.026 ± 0.001	0.03 ± 0.004	2.39 ± 0.082
	0.034 ± 0.002	0.06 ± 0.010	2.50 ± 0.025

Table 5.1: The experimental results for human bipedal impact

The experimental data was examined using SPSS software to determine whether the differences between subjects were statistically significant. A multivariate test showed that there was a statistically significant difference in impact results per initial velocity based on subject, F(12, 34.7) = 9.7, $p < 0.001$ for $v_{0_1} = 3.28$ m/s and F(12, 34.7) = 8.9, $p < 0.001$ for $v_{0_2} = 2.35$ m/s. A one-way analysis of variance revealed a statistically significant difference between subjects for stopping time, distance and velocity (Table 5.2.2). There was a very strong correlation between stopping time and distance traveled into the granular matter ($r(20) = 0.939$ for $v_{0_1} = 3.28$ m/s and $r(2) = 0.934$ for $v_{0_2} = 2.35$ m/s).

Under these conditions, the average impact results for human bipedal impacts across subjects could provide a good indicator of the impact with sand of the lower human body. The final displacement for the penetration phase is shown in Fig. 5.8 (a) and the decay of velocity during impact in Fig. 5.8 (b) for all subjects. The depth of the crater for the human lower body impact with granular sand is greater with higher initial impact velocity and it is also created more rapidly. Thus, for a human with average mass $m = 75.35 \pm 0.568$ kg and a height $h = 1.78 \pm 0.032$ m jumping onto a granular volume with $v_{01} = 3.28$ m/s, each foot will stop sinking at $d = 0.05$ m after $t_s = 0.030$ s. If the impact with the granular matter is somewhat slower, at $v_{02} = 2.35$ m/s, each foot will stop sinking at $d = 0.06$ m after $t_s = 0.035$ s.

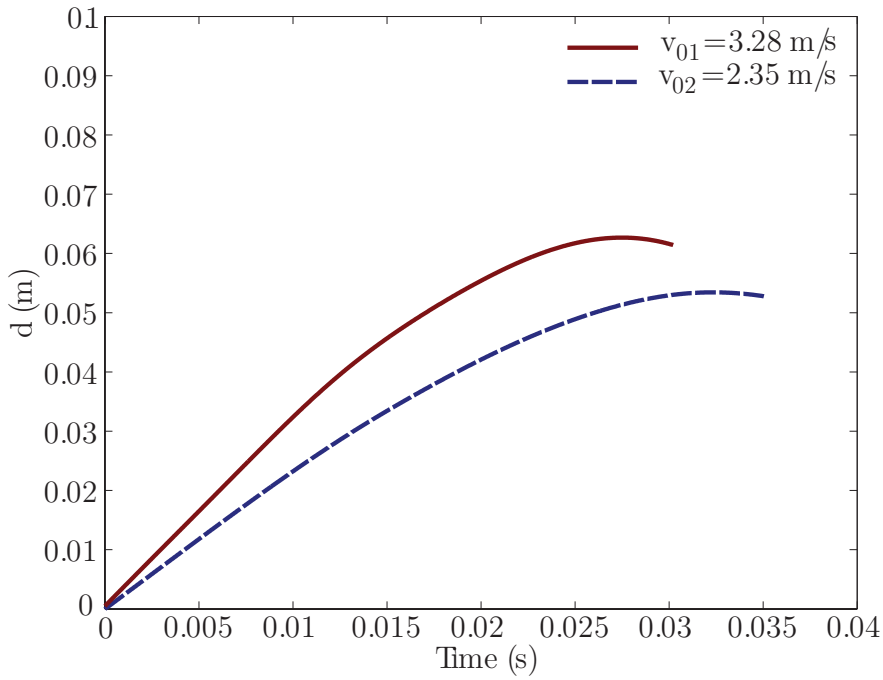

(a) Depth during impact

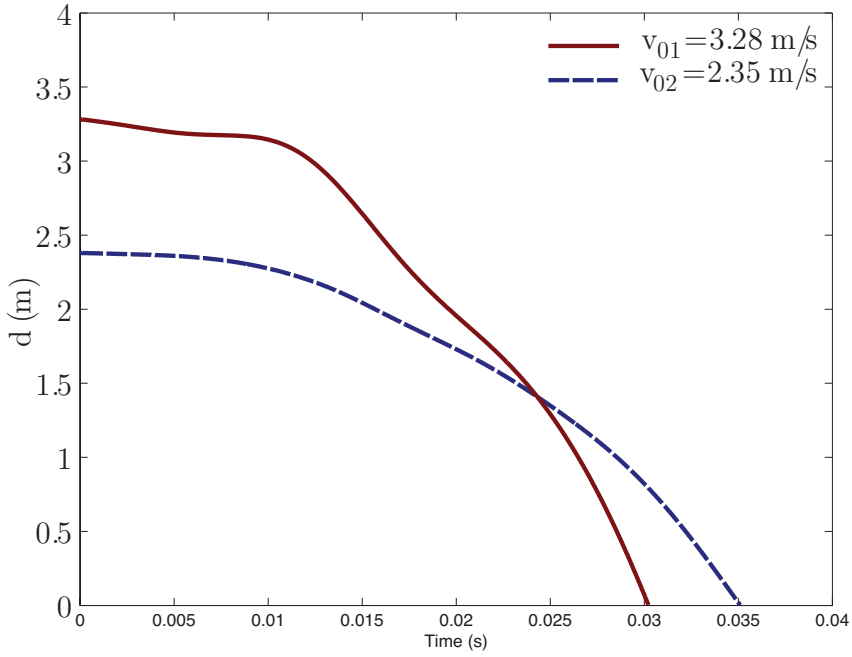

(b) Velocity during impact

Figure 5.8: Average, over all subjects, experimental results for human bipedal impact during penetration phase: (a) depth, and (b) velocity

	Variable	Source	*df*	Mean Squares	F	*p*
v_{01}	Time	Between Groups	4	0.000	33.117	0.000
		Within Groups	15	0.000		
	Depth	Between Groups	4	2.123	27.644	0.000
		Within Groups	15	0.077		
	Velocity	Between Groups	4	345.205	8.081	0.001
		Within Groups	15	42.718		
v_{02}	Time	Between Groups	4	0.000	29.369	0.000
		Within Groups	15	0.000		
	Depth	Between Groups	4	1.574	33.708	0.000
		Within Groups	15	0.047		
	Velocity	Between Groups	4	32.643	3.711	0.027
		Within Groups	15	8.7978		

Table 5.2: ANOVA results for human bipedal impacts

5.3 Simulation Model and Results

5.3.1 Simulation Model

A simulation CAD model was created for this study to simulate bipedal impact utilizing SolidWorks ® 2013-2014. A human model was created using SolidWorks human parts provided through the GrabCAD Community [16] by Emmanuel Mahay (Fig. 5.9). The parts were scaled to match the average size and weight of the experimental subjects ($m = 75.35 \pm 0.568$ kg and $h = 1.78 \pm 0.032$ m) using proportions defined by Dempster [10]. These parts were connected using coincident and concentric mates, to preserve the necessary degrees of freedom for each joint.

To model the impact of the human lower body with the granular matter, the equations proposed for the resistance force in Eqs. 5.1 - 5.4 were applied. Substituting the expressions for the reference area (Eq. 5.5), moving angle (Eq. 5.6) and immersed volume (Eq. 5.7), the expressions for the resistance force components become:

$$\mathbf{F_d} = -\mathbf{v}_E \, \eta_d \, \rho_g \, f_s \, \frac{d_{vT}}{\cos q} \left| \sin\left(q - \tan^{-1}\left(\frac{v_{Eh}}{v_{Ev}} \right) \right) \right| \, |\mathbf{v}_E|, \tag{5.8}$$

$$\mathbf{F}_{sh} = \left[-\text{sign}(v_{E_h}) \, \eta_h \, g \, \rho_g \, d_{vT}^2 \, f_s \right] \, \mathbf{i}, \tag{5.9}$$

$$\mathbf{F}_{sv} = \left[-\text{sign}(v_{E_v}) \, \eta_v \, (d_{vT}/l_l)^{\lambda} \, g \, \rho_g \, f_s \, w_s \, \frac{d_{vT}}{\sin q} \right] \, \mathbf{j}. \tag{5.10}$$

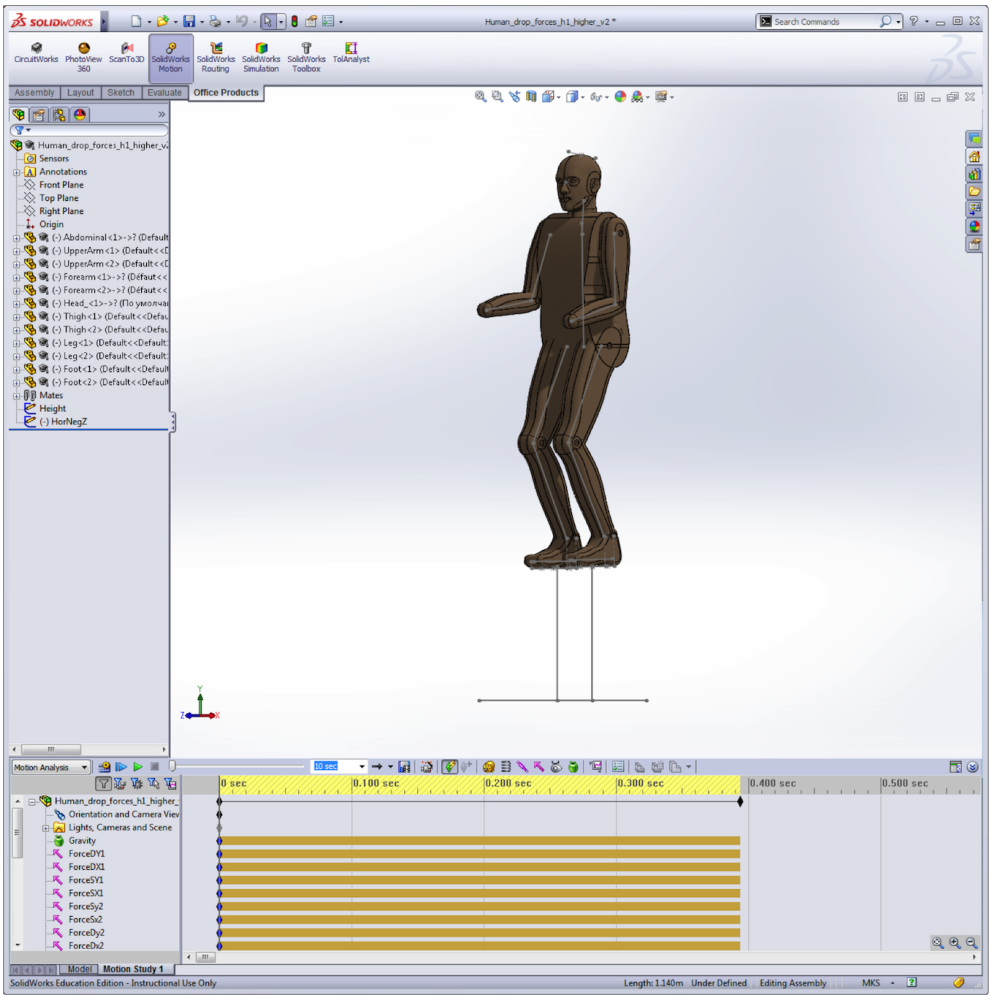

Figure 5.9: The SolidWorks human model

The velocity of the center of the immersed volume,E is defined in terms of the contact point of the bottom of the shoe, T:

$$\mathbf{v}_E = \frac{1}{2}\frac{d_{vT}}{t}\tan(q)\mathbf{1} + \frac{1}{2}\frac{d_{v_T}}{t}\mathbf{1}. \tag{5.11}$$

Therefore the equations for static resistance force and the dynamic force used in this simulation are:

$$F_{dv} = -\eta_d\,\rho_g\,f_s\,\frac{d_{vT}}{\cos q}\left|\sin\left(q - \tan^{-1}\left(\frac{\frac{1}{2}\frac{d_{vT}}{t}\tan q}{\frac{1}{2}\frac{d_{vT}}{t}}\right)\right)\right| \cdot \frac{1}{2}\frac{d_{vT}}{t}\cot\sqrt{\left(\frac{1}{2}\frac{d_{vT}}{t}\right)^2 + \left(\frac{1}{2}\frac{d_{vT}}{t}\tan q\right)^2}, \tag{5.12}$$

$$F_{dh} = -\eta_d\,\rho_g\,f_s\,\frac{d_{vT}}{\cos q}\left|\sin\left(q - \tan^{-1}\left(\frac{\frac{1}{2}\frac{d_{vT}}{t}\tan q}{\frac{1}{2}\frac{d_{vT}}{t}}\right)\right)\right| \cdot \frac{1}{2}\frac{d_{vT}}{t}\tan q\cot\sqrt{\left(\frac{1}{2}\frac{d_{v_T}}{t}\right)^2 + \left(\frac{1}{2}\frac{d_{vT}}{t}\tan q\right)^2}, \tag{5.13}$$

$$F_{sh} = -\text{sign}(\frac{1}{2}\frac{d_{vT}}{t}\tan q)\,\eta_h\,g\,\rho_g\,d_{vT}^2\,f_s, \tag{5.14}$$

$$F_{sv} = -\text{sign}(\frac{1}{2}\frac{d_{vT}}{t})\,\eta_v\,(d_{vT}/l_l)^\lambda\,g\,\rho_g\,f_s\,w_s\,\frac{d_{vT}}{\sin q}. \tag{5.15}$$

The impact angle q is measured as the angle of the tibia with the vertical axis. Because the human starts with an angle q close to 0^o, the expressions for $\alpha = 90^o$ in Table 3.2 can be used as a starting point to estimate the coefficients η_{d_i}, η_{h_i}, η_{v_i} and λ_i.

5.3.2 Simulation Results

After assigning values for all the force components in Motion Analysis mode in SolidWorks based on the realtime results: d_{vT}, q, the resistance force becomes active when $d_{vT} = 0$. The force coefficients values used were: $\eta_{d_1} = 13$, $\eta_{h_1} = 10$, $\eta_{v_1} = 195$ and $\lambda_1 = 1.05$ for $v_{01} = 3.28$ m/s and $\eta_{d_2} = 6$, $\eta_{h_2} = 12$, $\eta_{v_2} = 215$ and $\lambda = 0.9$ for $v_{01} = 2.35$ m/s. The granular matter density was $\rho_g = 1600$ kg/m^3. The other shape properties were scaled in relation to the average human subject size, with the foot size $f_s = 0.254$ m, the length of the tibia $l_l = 0.432$ m and the shoe width $w_s = 0.086$ m. Using the metric equivalents of these constants in the Motion Analysis model, the final displacement for the penetration phase and stopping time (when $v_{vT} = 0$ m/s) were extracted and analyzed.

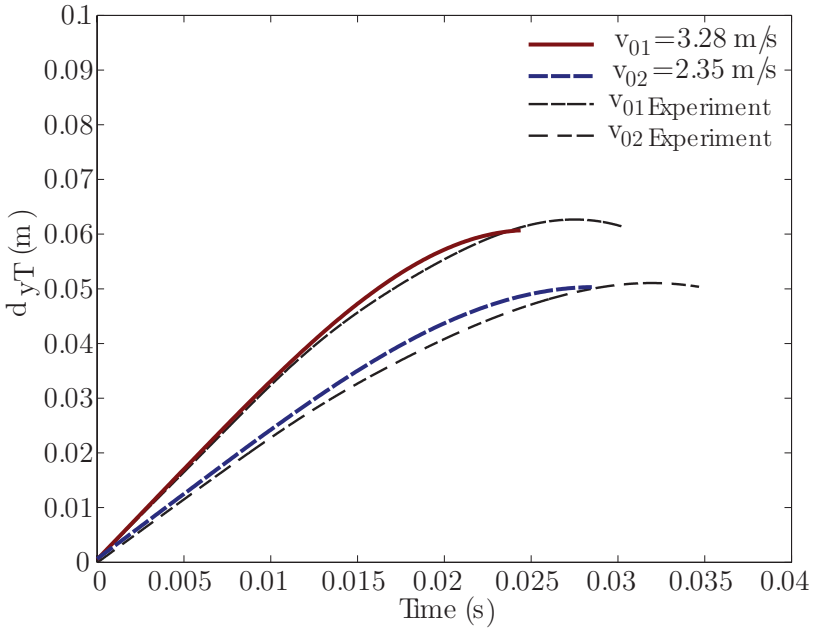

(a) Depth during impact

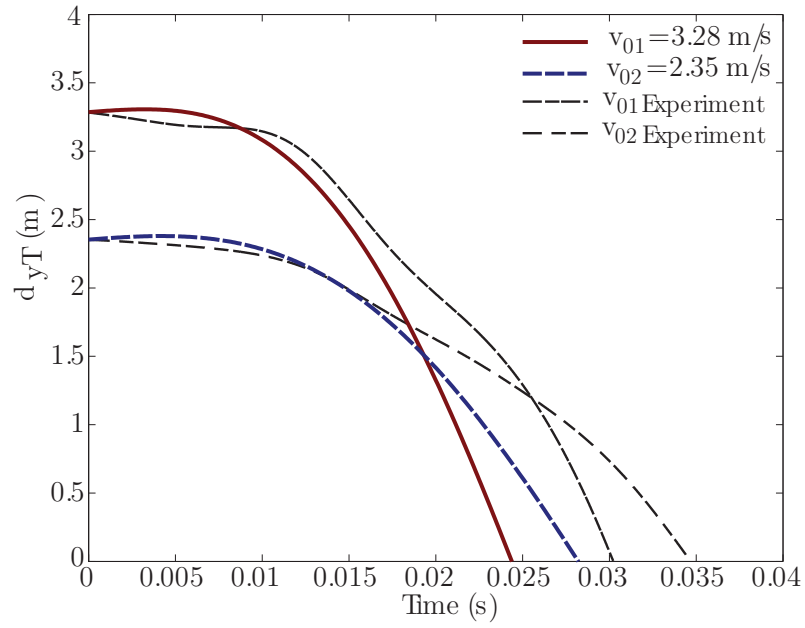

(b) Velocity during impact

Figure 5.10: The simulation and the average experimental results for all subjects: (a) depth, and (b) velocity

Figure 5.10 (a) presents the simulation results obtained, with the experimental results shown as dashed lines for comparison. For the initial velocities considered, the depth of immersion of the foot was higher for the higher velocity, but the stopping time was smaller for the higher velocity. Thus the foot will stop sinking into the granular matter faster, but it will go deeper at higher velocity. The simulation results broadly follow the curves obtained experimentally; the relative error calculated between the experimental results and those of the simulation results, ϵ, is given by

$$\epsilon = \left| \frac{de_{y_T}(t_s) - ds_{y_T}(t_s)}{de_{v_T}(t_s)} \right|, \tag{5.16}$$

where de_{y_T} is the final displacement extracted from the experiments, and ds_{y_T} is the final displacement from the simulation analysis when $v_{y_T}(t_s) = 0$. For $v_{01} = 3.29$ m/s, the simulation results end at $t_{s_1} = 0.024$ s and produce a depth $d_{yT_1} = 0.06$ m, with a relative error $\epsilon_1 = 1.17\%$. For the lower initial velocity, $v_{02} = 2.35$ m/s, the simulation results end at $t_{s_2} = 0.029$ s and thus produce a depth $d_{yT_2} = 0.05$ m, with a relative error $\epsilon_1 = 0.1\%$. The simulation model proposed for the bipedal impact produces results that are very close for the displacement, although the stopping times are significantly different. Figure 5.10 (b) shows clearly that the simulation stopping time is smaller than the stopping time measured experimentally.

5.4 Conclusions

For this study of the impact of the human lower body on granular matter were compared with those from computer simulations. Using a motion capture system with high accuracy, position data for the entire body were collected for five male subjects. Displacement during foot impact up to the point at which the vertical linear velocity of the shoe became zero, was higher for higher initial velocities. However, the shoe's immersion phase terminates faster at higher initial velocities. A statistically significant difference was found between subjects. For the first time, a CAD model of the human body was used to simulate this type of impact. The force resistance model proposed includes a dynamic term (quadratic velocity dependent) and a static (linear displacement dependent) term. The results produced by the simulation are consistent with the experimental results for displacement. As in the cases of a free link and a two link kinematic chain impact with

two contact points, the stopping time produced by the simulation predicted significantly different values than those obtained experimentally.

Chapter 6

Conclusions

This research examined the dynamics of the impact with granular matter of three different systems. The focus of the study was the use of a new model for the resistance force that represents the reaction of the medium to an intrusion, up to the end of the penetration phase. Previous studies investigating the contact force for such an impact have focused on a single type of impact, thus constraining the phenomenon, by performing experiments at very low speeds or limiting the shapes of the impactors. There was therefore a need for a comprehensive analysis of the dynamics of impact. A very important step is to create a force model that does not limit or constrict the impact such as the resistance force used in this study, which incorporates components that are both quadratic velocity dependent and linear depth dependent. The results obtained for this study establish a series of coefficients that can be used in this formulation. The validation of this force makes it possible to conduct a more in-depth study of the impact dynamics of complicated systems, such as two impact point kinematic chains and even human bipedal impacts. Up until now, the simulation of impacts with granular matter has been complicated and required a lot of computer power for discrete computational methods, but this study has adopted a new approach by utilizing the resistance force model to simulate the impact using computer-aided design software. This will open up valuable new avenues for investigation by enabling researchers to model a much wider and more diverse range of shapes, properties and initial conditions in studies of impact with granular matter.

In this research, simulation models for the impact of a free round-ended link were created using the computer aided design package SolidWorks. This software allows users to follow in real time the results computed at each step with high accuracy. A series of impact angles ($90 - 05^o$ in increments of 10^o) and initial velocities were inspected and the simulation results revealed that for higher initial velocities the penetration depth increases and the penetration phase ends faster. This result is valid not only for vertical impact, but also for impact at an angle. The results were validated by

comparing them with experimentally measured values for vertical, 45^o and 15^o impacts. There was a high dependency on the impact angle and initial velocity for the impact of a round-ended filled cylinder with granular matter. Both stopping time and depth decreased with the impact angle, but differently depending on the initial velocity. This study found that at small angles the impact becomes more complex and a closer analysis of this scenario is required in the future. Examining the components of the resistance force, the dynamic force increases during impact until it reaches a maximum and then decreases, while the static force increases uniformly throughout the impact. In terms of the energy dissipated to the volume during impact, its value also depends on impact angles and initial velocity. At lower velocities and low impact angles the potential energy is higher than the kinetic energy, while at higher initial velocities, the kinetic energy is much larger than the potential energy.

The phenomena whereby the decreased stopping time and increased penetrating distance arises as a result of the increased initial impact velocity also occur for the case of the impact of a two link kinematic chain with two points of impact. The simulation results (again obtained using SolidWorks) were consistent with the experimental results for the same initial velocities, although each link had a slightly different depth and stopping time at each velocity. These characteristics were carried through to the simulation because of the sensitivity of the force to the impact angle. The dynamic force was the dominant contributor to the total resistance force up to the point at which it reached its maximum, after which the contribution the static force became more significant. For low velocities, the intersection point at which the crossover between the static force and the dynamic force occurred was closer to the beginning of the impact event. The potential energy decreased rapidly, and the kinetic energy took over at higher velocities.

The validation of the force model for the two link kinematic chain facilitated the extension of the model to describe the impact of the human lower body with granular matter. A human model was created in SolidWorks and the resistance component forces applied at the ankle joint. The simulation results for two initial velocities revealed that the behavior of the granular matter when impacted is consistent with the two simpler cases. For higher velocity impacts, the human foot sank deeper and faster than for lower initial velocities. The experiments performed with five male subjects produced results that were statistically significant between subjects and the averaged results were consistent with those obtained using the simulation. A rigorous model for jumping on

solid surfaces is not yet available and the work in Chapter 5 represents only the very earliest steps in this new field of study. The force model proposed here will doubtless be improved as we more is learned and gain a better understanding of human kinematics. This study of human lower body impacts is significant as provides a stepping stone towards developing a comprehensive analysis of energy expenditure, joint stress, tendon and ligaments recovery, and prosthetics.

Bibliography

[1] I. Albert, J. G. Sample, A. J. Morss, S. Rajagopalan, A.-L. Barabasi, and P. Schiffer. Granular drag on a discrete object: Shape effects on jamming. *Physical Review E.*, 64:061303:1–4, 2001.

[2] R. Albert, M. A. Pfeifer, A.-L. Barabsi, and P. Schiffer. Slow drag in granular medium. *Physical Review Letters*, 82 (1):205–209, 1999.

[3] P. E. Alcaraz, J. M. Palao, J. L. L. Elvira, and N. P. Linthorne. Effects of a sand running surface on the kinematics of sprinting at maximum velocity. *Biology of Sport*, 28(2):95–101, 2011.

[4] M. A. Ambroso, R. D. Kamien, and D. J. Durian. Dynamics of shallow impact cratering. *Physical Review E*, 72:041305 1 – 4, 2005.

[5] Optotrack brochure from http://www.ndigital.com/.

[6] John R. Bruyn and Amanda M. Walsh. Penetration of spheres into loose granular media. *Canadian Journal of Physics*, 82:439–446, 2004.

[7] T. A. Brzinski III, P. Mayor, and D. J. Durian. Depth-dependent resistance of granular media to vertical penetration. *Physical Review Letters*, 111:168002:1–5, 2013.

[8] D. J. Costantino, J. Bartell, K. Scheidler, and P. Schiffer. Low-velocity granular drag in reduced gravity. *Physical Review E*, 83:011305:1–4, 2011.

[9] K. D'Aout, L. Meert, B. Van Gheluwe, D. De Clercq, and P. Aerts. Experimentally generated footprints in sand: Analysis and consequences for the interpretation of fossil and forensic footprints. *American Journal Of Physical Anthropology*, 141(4):515–525, 2009.

[10] Wilfrid T. Dempster and George R. L. Gaughran. Properties of body segments based on size and weight. *American Journal of Anatomy*, 120:33–54, 1967.

[11] Yang Ding, Nick Gravish, and Daniel I. Goldman. Drag induced lift in granular media. *Physical Review Letters*, 106:028001: 1 – 4, 2011.

[12] Thierry Faug, Remi Beguin, and Benoit Chanut. Mean steady granular force on a wall overflowed by free-surface gravity-driven dense flows. *Physical Review E*, 80:021305: 1 – 13, 2009.

[13] Thierry Faug, Paolo Caccamo, and Benoit Chanut. Equation for the force experienced by a wall overflowed by a granular avalanche: Experimental verification. *Physical Review E*, 84:051301: 1 – 7, 2011.

[14] D. P. Ferris and C. T. Farley. Interaction of leg stiffness and surface stiffness during human hopping. *Journal of Applied Physiology*, 82:15–22, 1997.

[15] Daniel P. Ferris, Micky Louie, and Claire T. Farley. Runners adjust leg stillness for their first step on a new running surface. *Journal of Biomechanics*, 32:787–794, 1999.

[16] GrabCAD Community from http://grabcad.com//.

[17] Dassault Systems SolidWorks Help from http://help.solidworks.com.

[18] Dassault Systems SolidWorks 2014 from http://www.solidworks.com/.

[19] Paolo Gaudinoa, Claudio Gaudinob, Giampietro Albertia, and Alberto E. Minettic. Biomechanics and predicted energetics of sprinting on sand: Hints for soccer training. *Journal of Science and Medicine in Sport*, 16(3):271–275, 2013.

[20] Daniel I. Goldman and Paul Umbanhowar. Scaling and dynamics of sphere and disk impact into granular media. *Physical Review E*, 77: 021308:1–14, 2008.

[21] Nick Gravish. Force and flow at the onset of drag in plowed granular media. *Physical Review E*, 89:042202: 1 – 10, 2014.

[22] Francois Guillard, Yoel Forterre, and Olivier Pouliquen. Depth-independent drag force induced by stirring in granular media. *Physical Review Letters*, 110:138303: 1 – 5, 2013.

[23] Francois Guillard, Yoel Forterre, and Olivier Pouliquen. Lift forces in granular media. *Physics of Fluids*, 26:043301, 1–16, 2014.

[24] G. Hill, S. Yeung, and S. A. Koehler. Scaling vertical drag forces in granular media. *Europhys. Letters*, 70(1):137–143, 2005.

[25] M. Hou, Z. Peng, R. Liu, K. Lu, and C.K. Chan. Dynamics of a projectile penetrating in granular systems. *Physical Review E*, 72:062301(4), 2005.

[26] F M Impellizzeri, E Rampinini, C Castagna, F Martino, S Fiorini, and U Wislof. Effect of plyometric training on sand versus grass on muscle soreness and jumping and sprinting ability in soccer players. *British Journal of Sports Medicine*, 42:42–46, 2008.

[27] Alicia Anne Karver. Sand jump training versus ground jump training for volleyball players, 2012.

[28] H. Katsuragi and D.J. Durian. Unified force law for granular impact cratering. *Nature Physics*, 3:420–423, 2007.

[29] S. Lee and D. B. Marghitu. Analysis of a rigid body obliquely impacting granular matter. *Nonlinear Dynamics*, 57:289–301, 2009.

[30] S. Lee and D. B. Marghitu. Analytical and experimental analysis of a free link in contact with a granular medium. *The ScientificWorld Journal*, 2013:808574 : 1–9, 2013.

[31] S. Lee and D.B. Marghitu. Multiple impacts of a planar kinematic chain with a granular matter. *International Journal of Mechanical Sciences*, 51:881–887, 2009.

[32] T. M. Lejeune, P. A. Willems, and N. C. Heglund. Mechanics and energetics of human locomotion on sand. *The Journal of Experimental Biology*, 201:2071–2080, 1998.

[33] C. Li, P.B. Umbanhowar, H. Komsuoglu, and D.I. Goldman. The effect of limb kinematics on the speed of a legged robot on granular media. *Experimental Mechanics*, 50:1383–1393, 2010.

[34] C. Li, P.B. Umbanhowar, H. Komsuoglu, DE Koditschek, and D.I. Goldman. Sensitive dependence of the motion of a legged robot on granular media. *Proc Natl Acad Sci*, 106(9):3029–3034, 2009.

[35] Chen Li, S. Tonia Hsieh, and Daniel I. Goldman. Multi-functional foot use during running in the zebra-tailed lizard. *The Journal of Experimental Biology*, 215:3293–3308, 2012.

[36] Chen Li, Tingnan Zhang, and Daniel I. Goldman. A terradynamics of legged locomotion on granular media. *The European Physical Journal*, 35:7:1–12, 2013.

[37] Ryan D. Maladen, Yang Ding, Chen Li, and Daniel I. Goldman. Undulatory swimming in sand:subsurface locomotion of the sandfish lizard. *Science*, 325:314–318, 2009.

[38] K. Matsuyama and H. Katsuragi. Power law statistics of force and acoustic emission from a slowly penetrated granular bed. *Nonlinear Processes Geophys.*, 21:1–8, 2014.

[39] Nicole Mazouchova, Nick Gravish, Andrei Savu, and Daniel I. Goldman. Utilization of granular solidification during terrestrial locomotion of hatchling sea turtles. *Biology Letters*, 6:398–401, 2010.

[40] Chet T. Moritz and Claire T. Farley. Human hopping on damped surfaces: strategies for adjusting leg mechanics'. *The Royal Society*, 270:1741–1746, 2003.

[41] Shigeru Muramatsu, Akinori Fukudome, Motoyoshi Miyama, Morio Arimoto, and Akira Kijima. Energy expenditure in maximal jumps on sand. *Journal of Physiology Anthropology*, 25(1):59–61, 2006.

[42] Zheng Peng, Xiantao Xu, Kunquan Lu, and Meiying Hou. Depth dependence of vertical plunging force in granular medium. *Physical Review E*, 80:021301:1–5, 2009.

[43] A. Seguin, Y. Bertho, P. Gondret, and J. Crassous. Dense granular flow around a penetrating object: Experiment and hydrodynamic model. *Physical Review Letters*, 107: 048001:1–4, 2011.

[44] R. G. Soule and R. F. Goldman. Terrain coefficients for energy cost prediction. *Journal of Applied Physiology*, 32 (5):706–708, 1972.

[45] T. Spagele, A. Kistner, and A. Gollhofer. Modelling, simulation and optimization of a human vertical jump. *Journal of Biomechanics*, 32:521–530, 1999.

[46] David J. Szymanski, Joseph McIntyre, Jessica M. S. Szymanski, T. Jason Bradford, Ryan L. Schade, Nels H. Madsen, and David D. Pascoe. Effect of torso rotational strength on angular hip, angular shoulder, and linear bat velocities of high school baseball players. *Journal of Strength and Conditioning Research*, 21(4):1117–1125, 2007.

[47] David J. Szymanski, Jessica M. S. Szymanski, Ryan L. Schade, T. Jason Bradford, Joseph McIntyre, Coop DeRenne, and Nels H. Madsen. The relation between anthropometric and physiological variables and bat velocity of high-school baseball players before and after 12 weeks of training. *Journal of Strength and Conditioning Research*, 24:2933–2943, 2010.

[48] Dimitris P. Tsakiris, Michael Sfakiotakis, Arianna Menciassi, Gianni La Spina, and Paolo Dario. Polychaete-like undulatory robotic locomotion. Proceedings of the 2005 IEEE. Barcelona, Spain, April 2005.

[49] L.S. Tsimring and D. Volfson. Modeling of impact cratering in granular media. *Powders and Grains 2005*, pages pp.1215–1223, 2005.

[50] J. S. Uehara, M. A. Ambroso, R.P. Ojha, and D. J. Durian. Low-speed impact craters in loose granular media. *Physical Review Letters*, 90: 194301:1–4, 2003.

[51] Paul Umbanhowar and Daniel I. Goldman. Granular impact and the critical packing state. *Physical Review E*, 82: 010301:1–4, 2010.

[52] Dengming Wang, Xiaoyan Ye, and Xiaojing Zheng. The scaling and dynamics of a projectile obliquely impacting a granular medium. *The European Physical Journal E*, 35:7:1–12, 2012.

[53] Lichao Xu, Shiwu Zhang, Ronald Xu, and Jie Yang. A hybrid force model to estimate the dynamics of curved legs in granular materials. *IEEE Transaction On Robotics*, XXX:1–9, 2013.

[54] P. Zamparo, R. Perini, C. Orizio, M. Sacher, and G. Ferretti. The energy cost of walking or running on sand. *European Journal of Applied Physiology*, 65:183–187, 1992.

Appendices

Appendix A

NDI ToolBench Pipeline

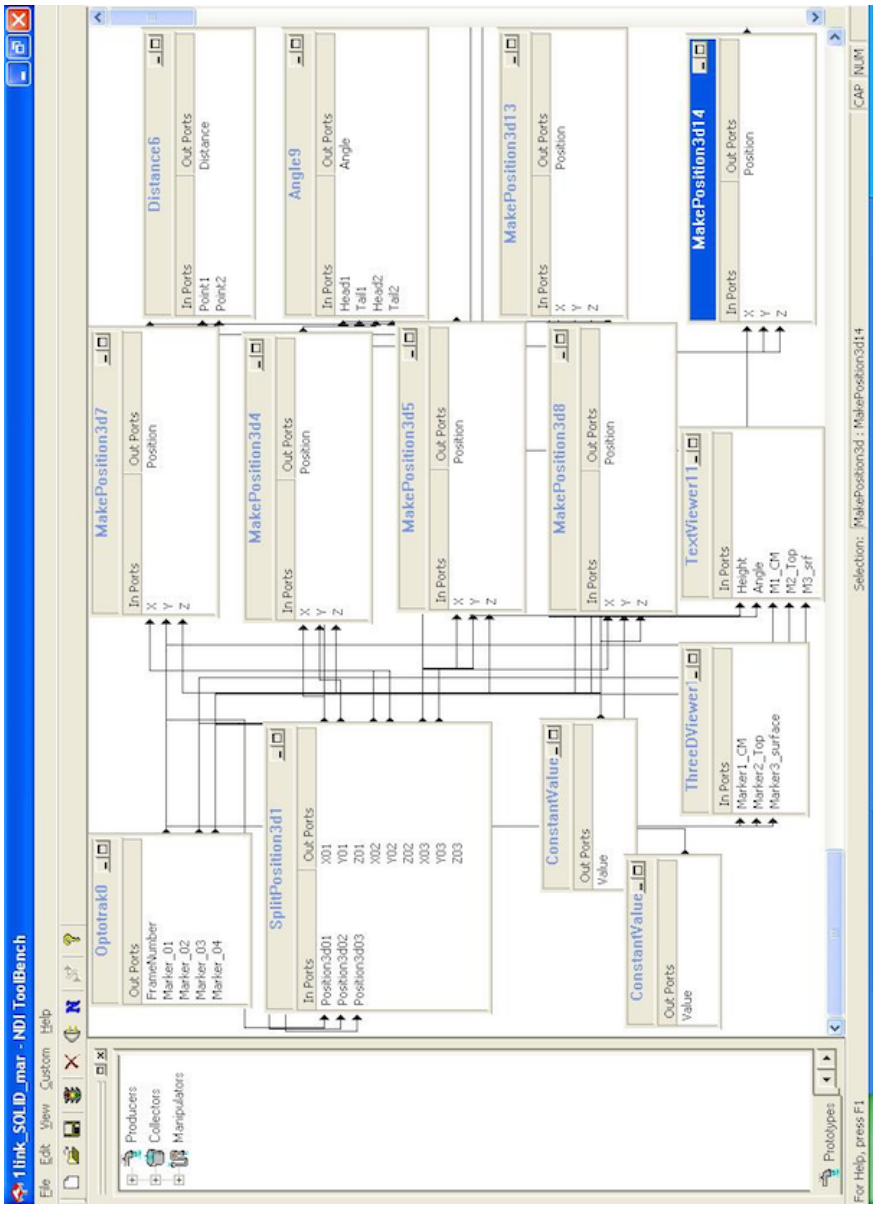

Appendix B

NDI ToolBench Two Dimensional View Of The Three Infrared Markers

The figure below shows a 2D view of the three markers used in the free link fall experiment. The angle that the two markers on the link create with the horizontal is approximatively zero.

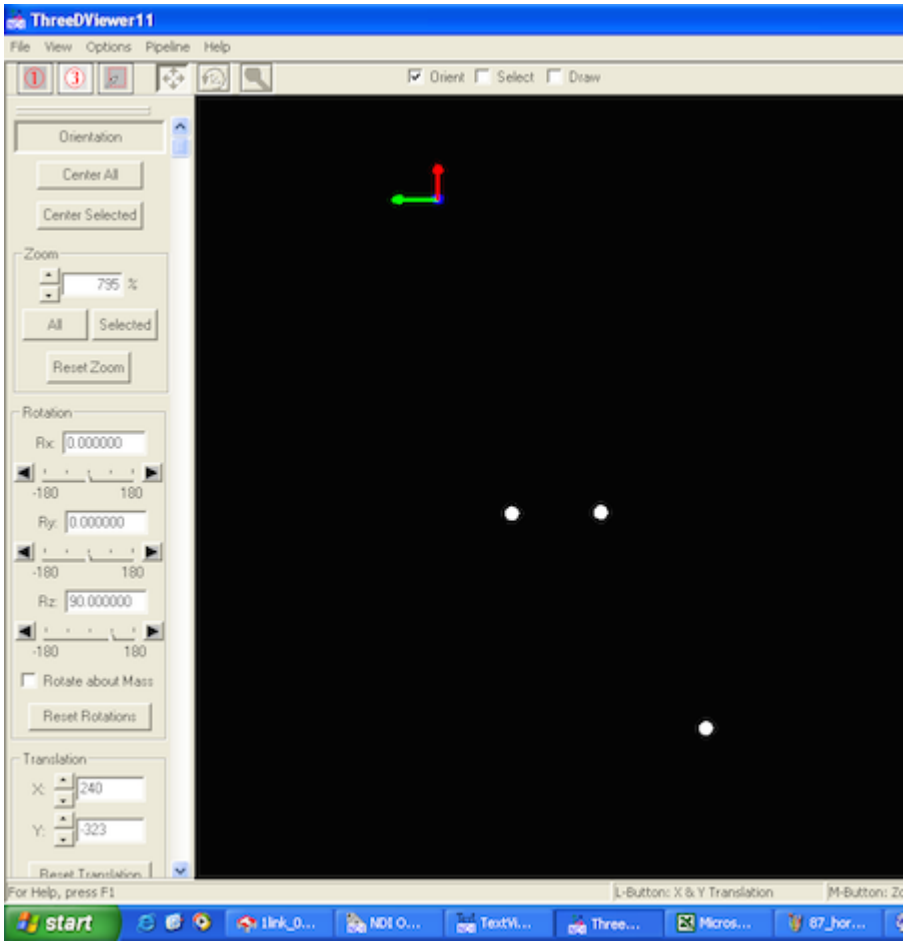

Appendix C

The Expressions of the Resistance Force Components in SolidWorks

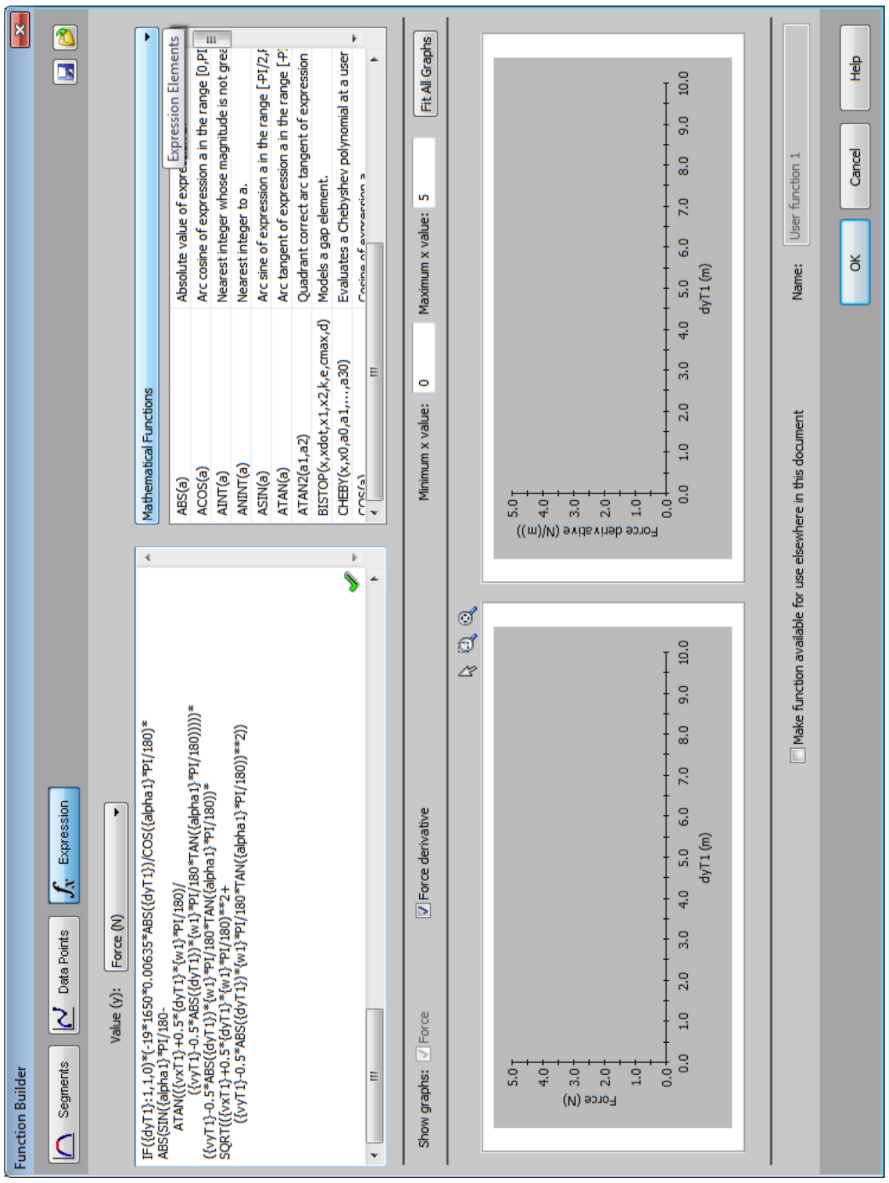

Figure C.1: Force builder screen

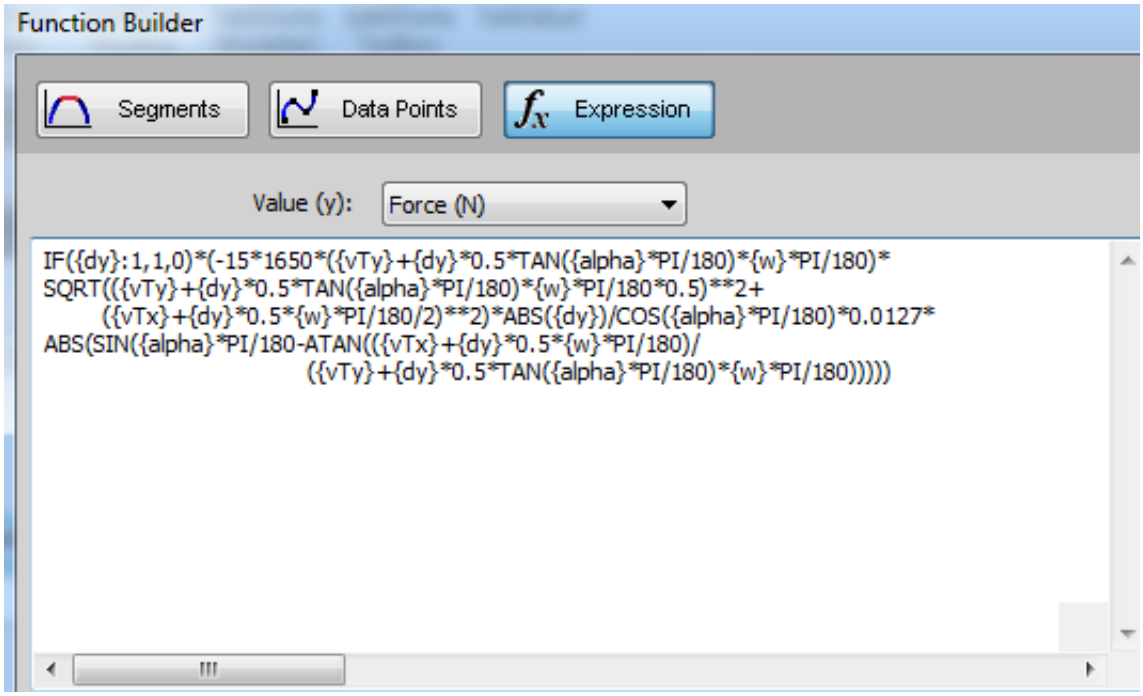

Figure C.2: Dynamic force on vertical

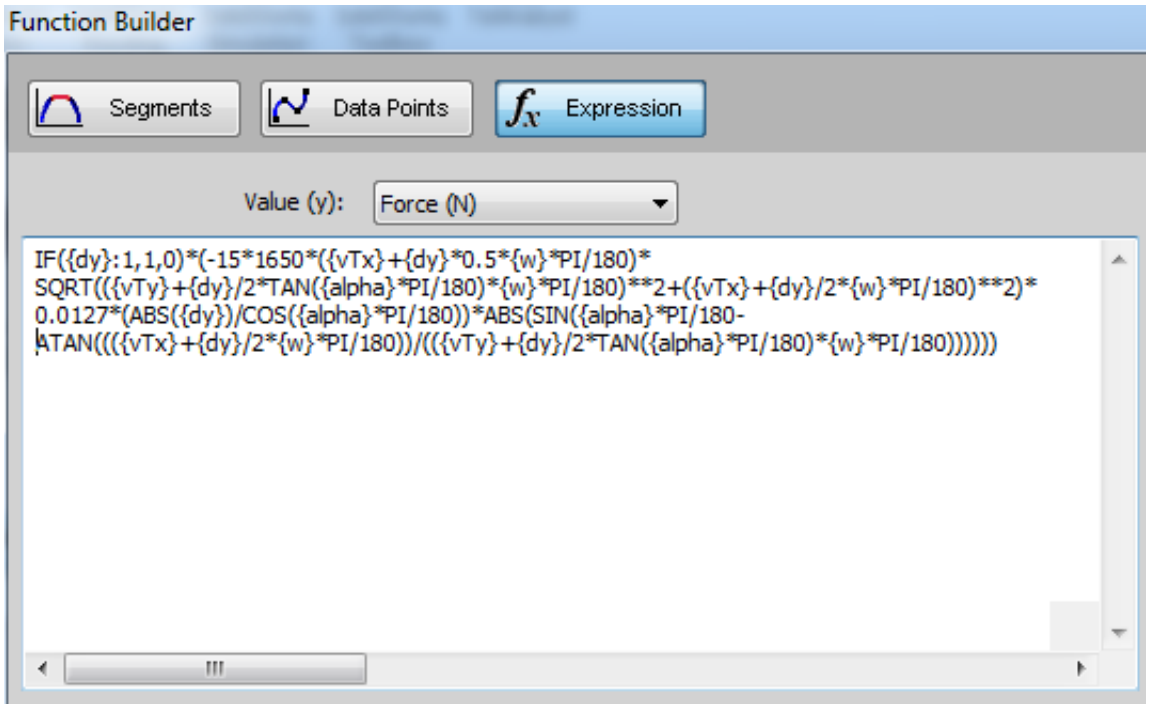

Figure C.3: Dynamic force on horizontal

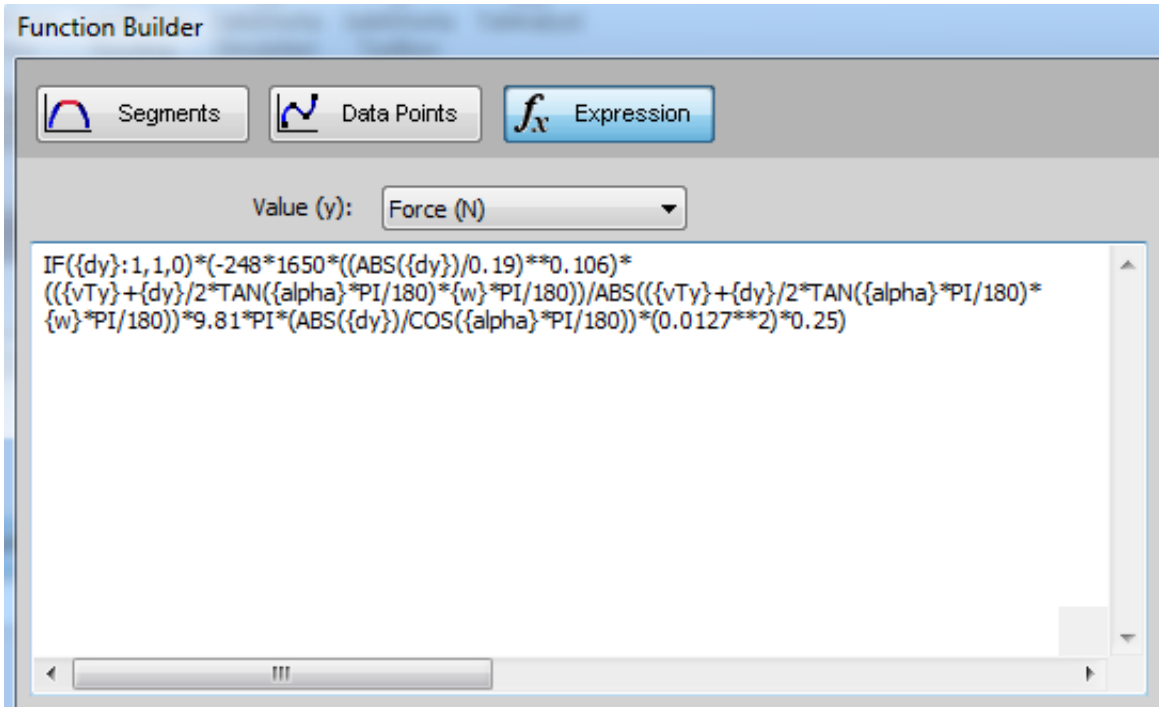

Figure C.4: Static force on vertical

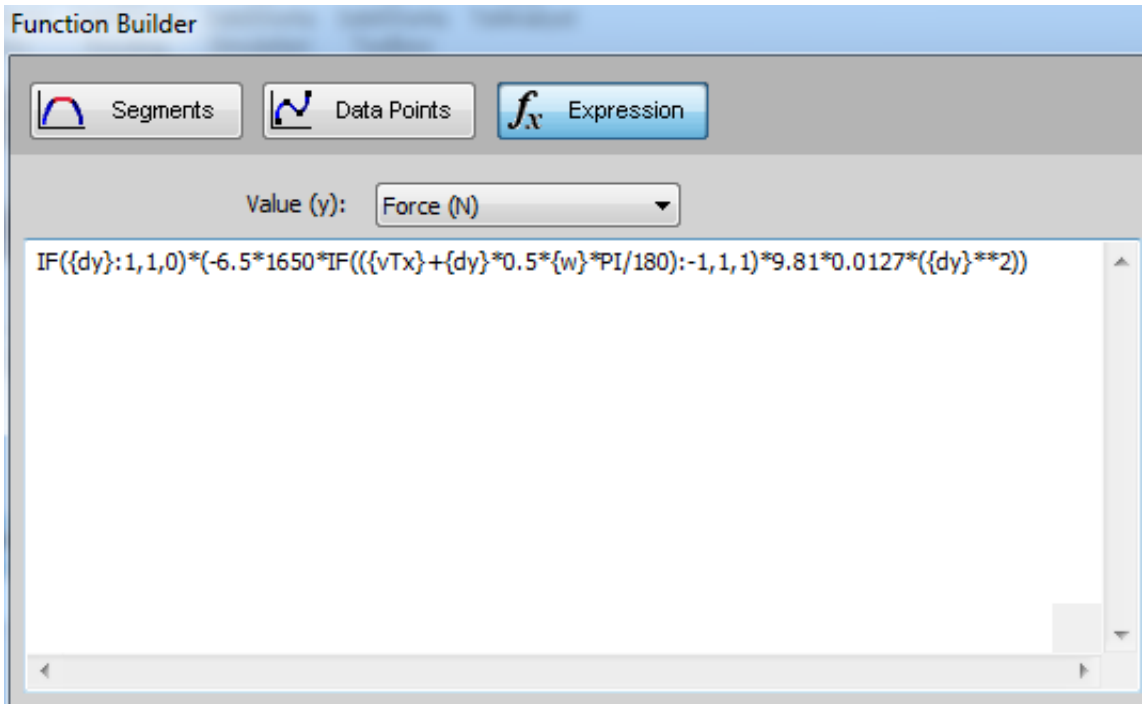

Figure C.5: Static force on horizontal

Appendix D

The Resistive Force Components In SolidWorks

D.1 Force Components for q = 0^o

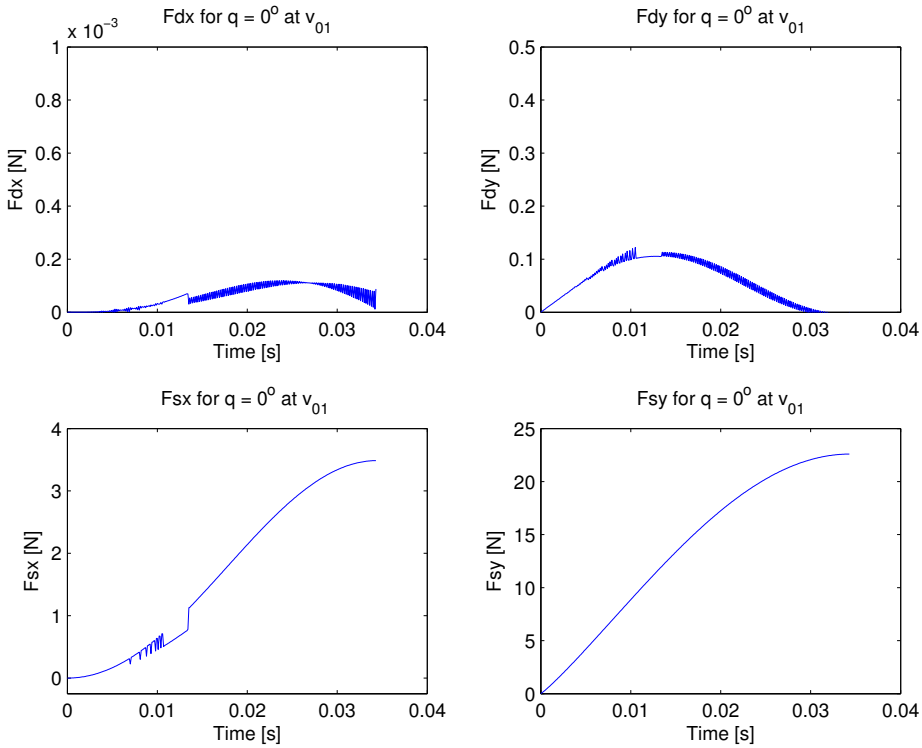

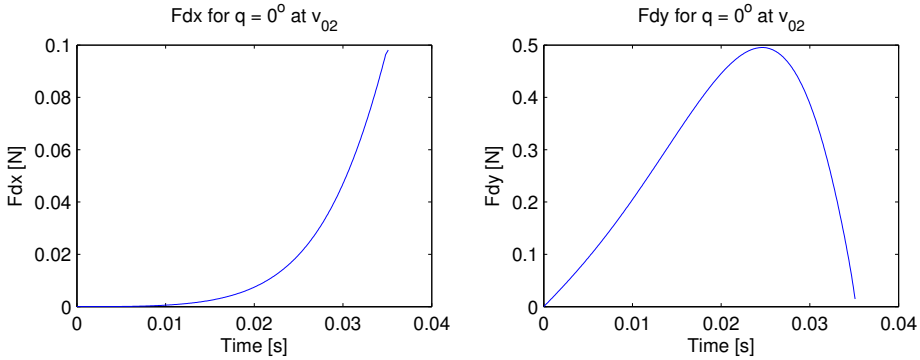
Fdx for q = 0° at v02
Fdx [N]
Time [s]
0
0.02
0.04
0.06
0.08
0.1
0.01
0.03

Fdy for q = 0° at v02
Fdy [N]
Time [s]
0
0.1
0.2
0.3
0.4
0.5
0.01
0.02
0.03
0.04

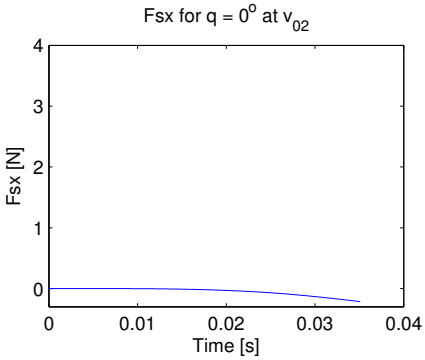
Fsx for q = 0° at v02
Fsx [N]
Time [s]
0
1
2
3
4
0.01
0.02
0.03
0.04

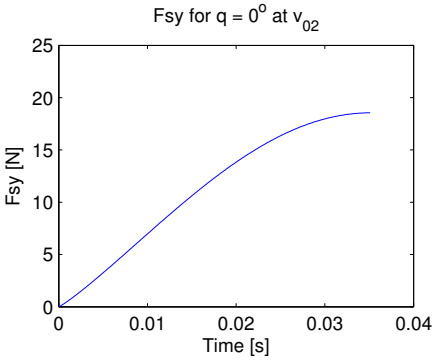
Fsy for q = 0° at v02
Fsy [N]
Time [s]
0
5
10
15
20
25
0.01
0.02
0.03
0.04

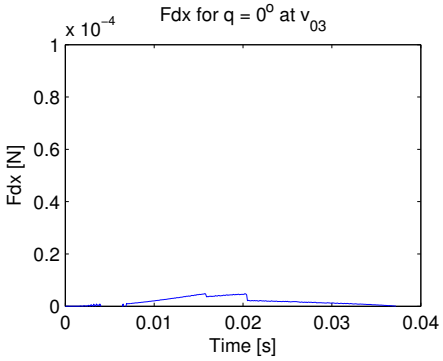
Fdx for q = 0° at v03
x 10−4
Fdx [N]
Time [s]
0
0.2
0.4
0.6
0.8
1
0.01
0.02
0.03
0.04

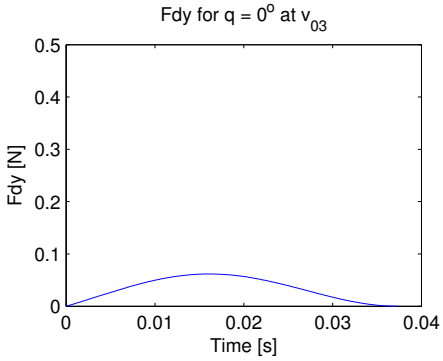
Fdy for q = 0° at v03
Fdy [N]
Time [s]
0
0.1
0.2
0.3
0.4
0.5
0.01
0.02
0.03
0.04

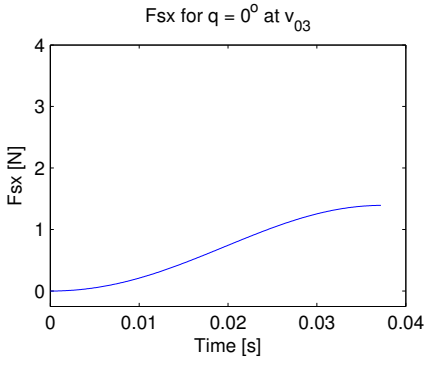
Fsx for q = 0° at v03
Fsx [N]
Time [s]
0
1
2
3
4
0.01
0.02
0.03
0.04

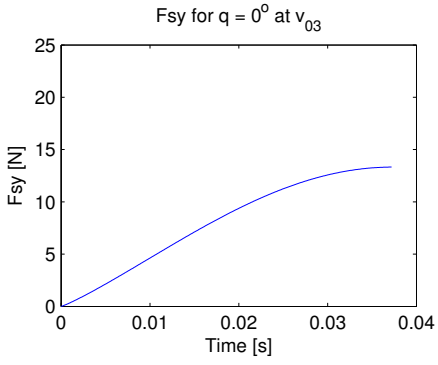
Fsy for q = 0° at v03
Fsy [N]
Time [s]
0
5
10
15
20
25
0.01
0.02
0.03
0.04

D.2 Force Components for q = 5^o

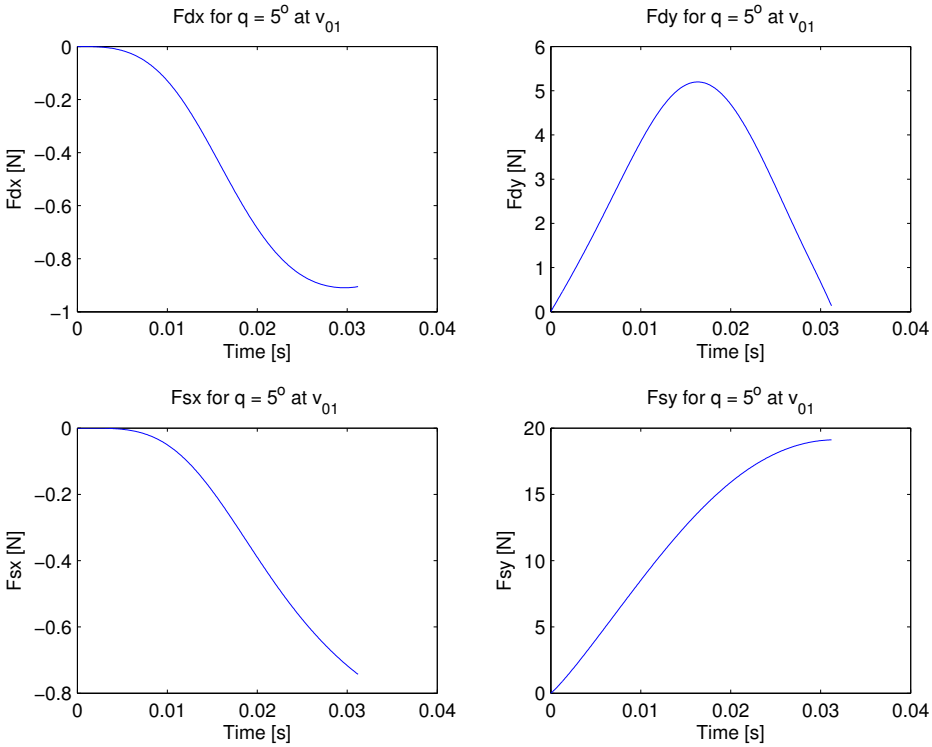

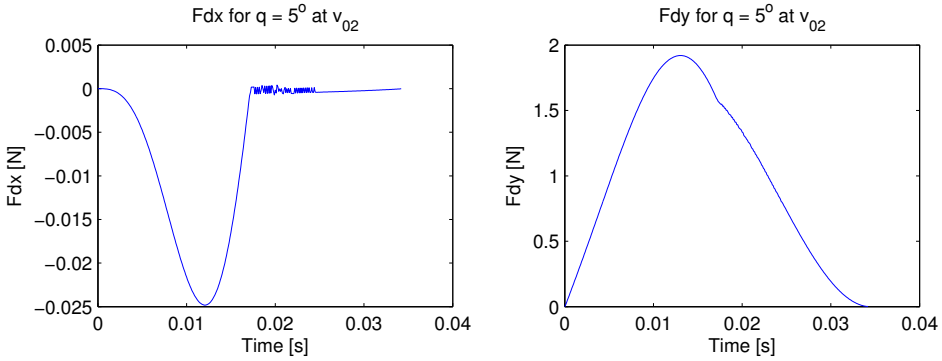
Fdx for q = 5° at v02
Fdx [N]
Time [s]
0.005
0
−0.005
−0.01
−0.015
−0.02
−0.025
0
0.01
0.02
0.03
0.04

Fdy for q = 5° at v02
Fdy [N]
Time [s]
2
1.5
1
0.5
0
0
0.01
0.02
0.03
0.04

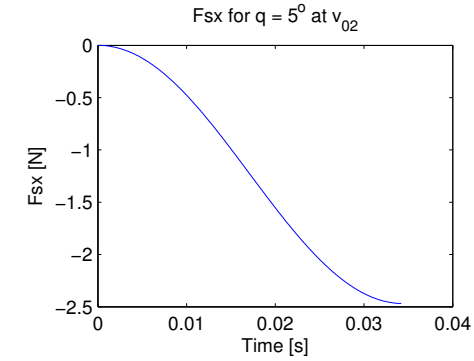
Fsx for q = 5° at v02
Fsx [N]
Time [s]
0
−0.5
−1
−1.5
−2
−2.5
0
0.01
0.02
0.03
0.04

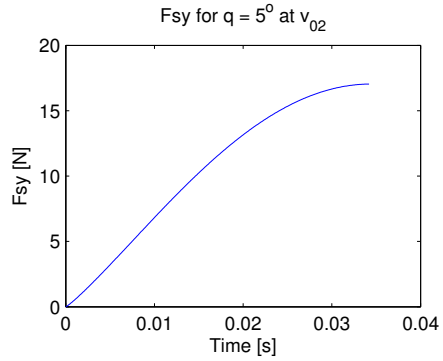
Fsy for q = 5° at v02
Fsy [N]
Time [s]
20
15
10
5
0
0
0.01
0.02
0.03
0.04

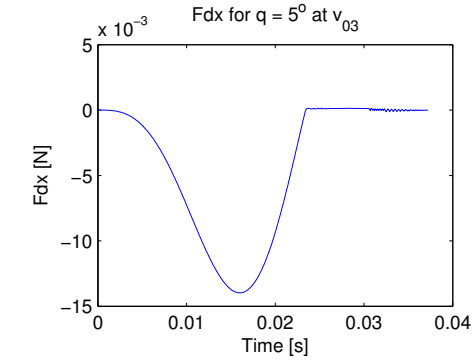
Fdx for q = 5° at v03
x 10−3
Fdx [N]
Time [s]
5
0
−5
−10
−15
0
0.01
0.02
0.03
0.04

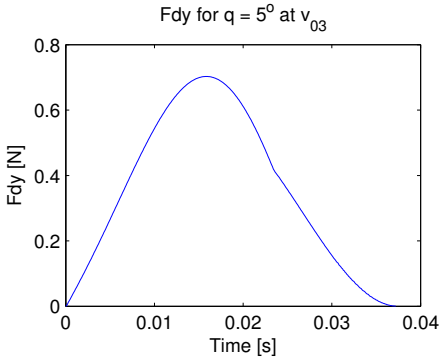
Fdy for q = 5° at v03
Fdy [N]
Time [s]
0.8
0.6
0.4
0.2
0
0
0.01
0.02
0.03
0.04

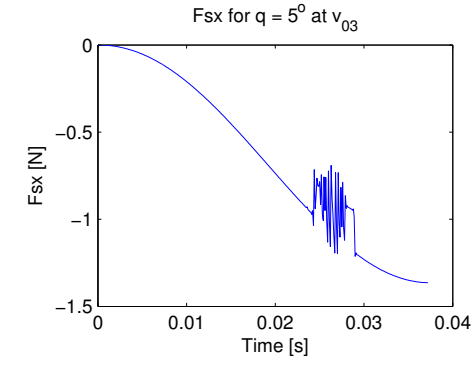
Fsx for q = 5° at v03
Fsx [N]
Time [s]
0
−0.5
−1
−1.5
0
0.01
0.02
0.03
0.04

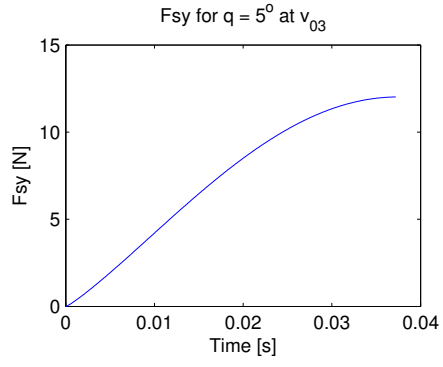
Fsy for q = 5° at v03
Fsy [N]
Time [s]
15
10
5
0
0
0.01
0.02
0.03
0.04

D.3 Force Components for q = 15^o

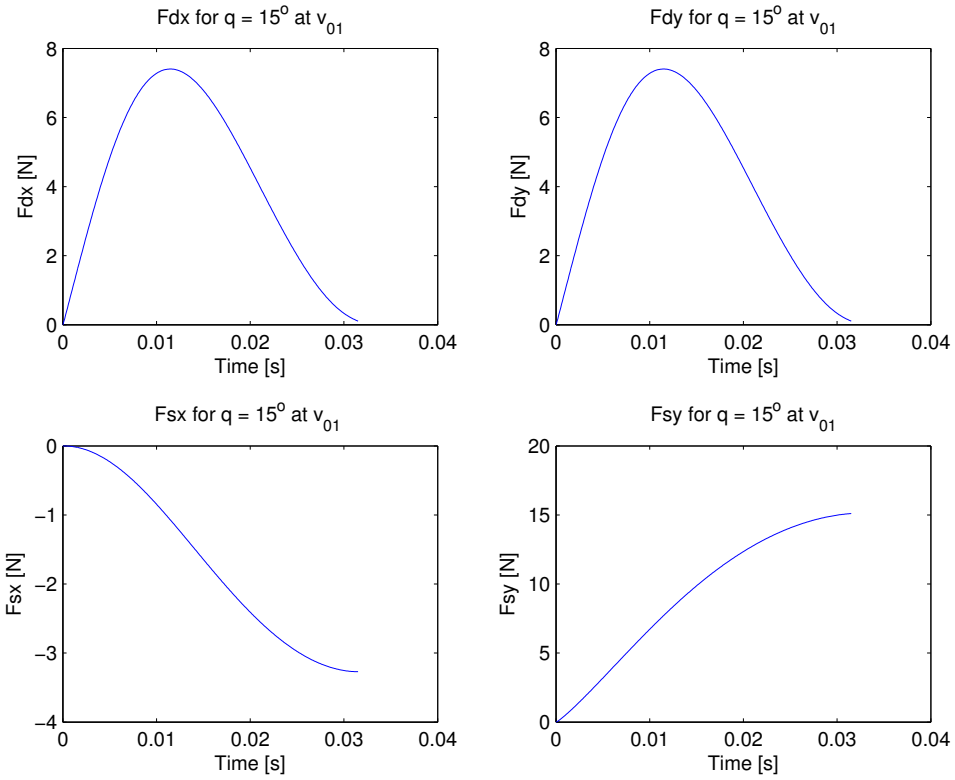

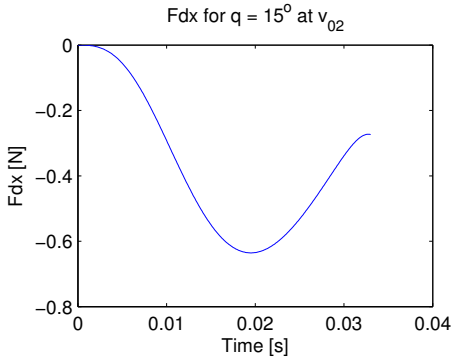
Fdx for q = 15° at v02
Fdx [N]
Time [s]
0
−0.2
−0.4
−0.6
−0.8
0
0.01
0.02
0.03
0.04

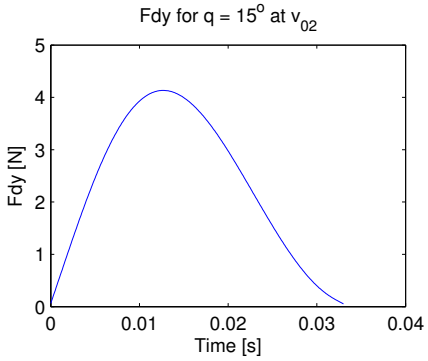
Fdy for q = 15° at v02
Fdy [N]
Time [s]
5
4
3
2
1
0
0
0.01
0.02
0.03
0.04

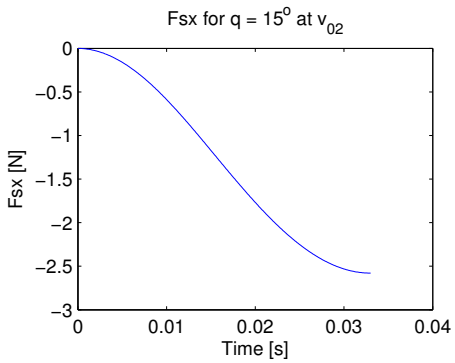
Fsx for q = 15° at v02
Fsx [N]
Time [s]
0
−0.5
−1
−1.5
−2
−2.5
−3
0
0.01
0.02
0.03
0.04

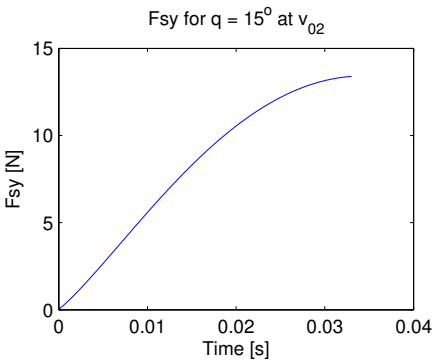
Fsy for q = 15° at v02
Fsy [N]
Time [s]
15
10
5
0
0
0.01
0.02
0.03
0.04

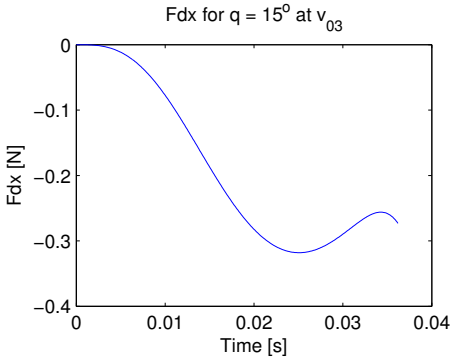
Fdx for q = 15° at v03
Fdx [N]
Time [s]
0
−0.1
−0.2
−0.3
−0.4
0
0.01
0.02
0.03
0.04

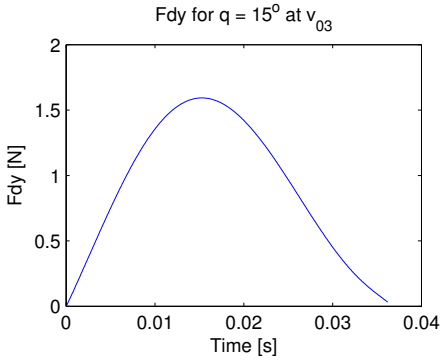
Fdy for q = 15° at v03
Fdy [N]
Time [s]
2
1.5
1
0.5
0
0
0.01
0.02
0.03
0.04

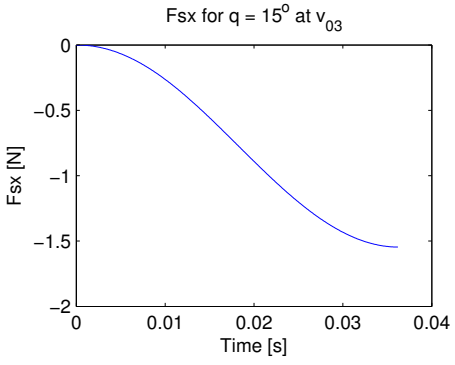
Fsx for q = 15° at v03
Fsx [N]
Time [s]
0
−0.5
−1
−1.5
−2
0
0.01
0.02
0.03
0.04

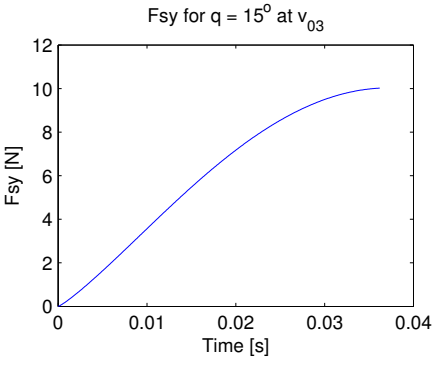
Fsy for q = 15° at v03
Fsy [N]
Time [s]
12
10
8
6
4
2
0
0
0.01
0.02
0.03
0.04

D.4 Force Components for q = 25^o

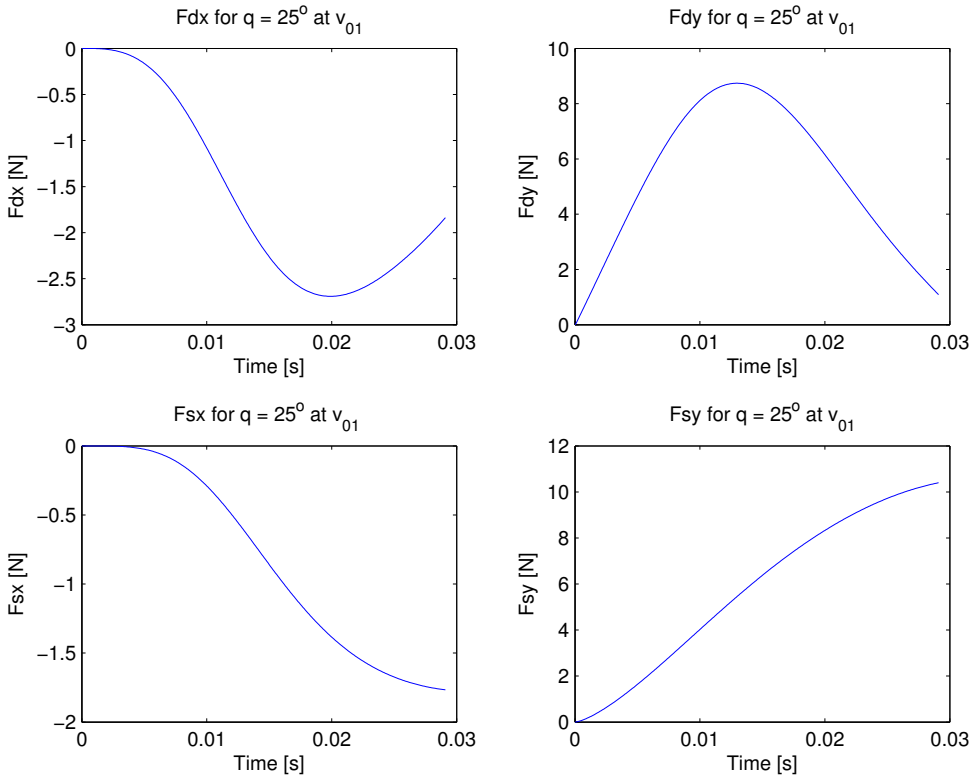

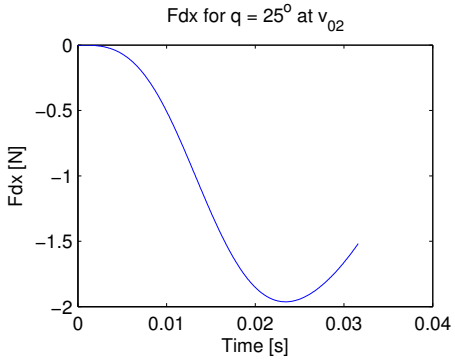
Fdx for q = 25° at v02
Fdx [N]
Time [s]
0
−0.5
−1
−1.5
−2
0.01
0.02
0.03
0.04

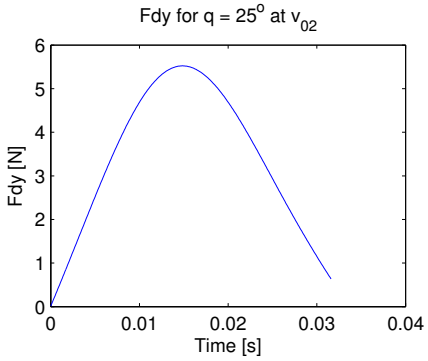
Fdy for q = 25° at v02
Fdy [N]
Time [s]
6
5
4
3
2
1
0
0.01
0.02
0.03
0.04

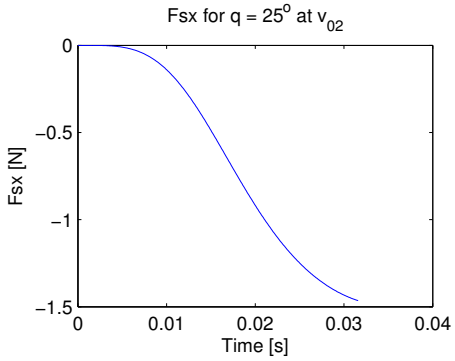
Fsx for q = 25° at v02
Fsx [N]
Time [s]
0
−0.5
−1
−1.5
0.01
0.02
0.03
0.04

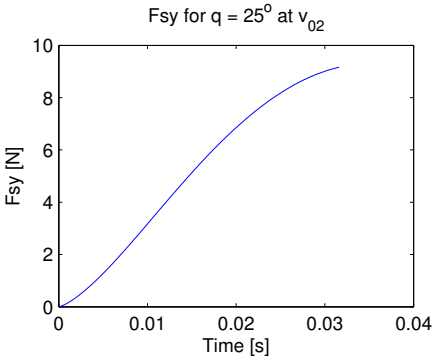
Fsy for q = 25° at v02
Fsy [N]
Time [s]
10
8
6
4
2
0
0.01
0.02
0.03
0.04

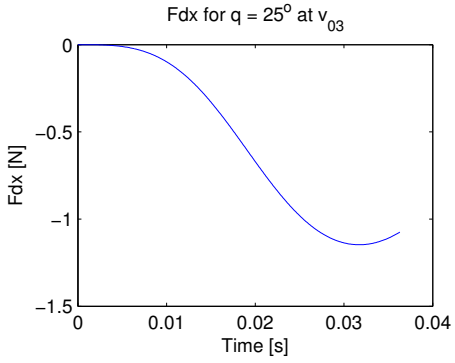
Fdx for q = 25° at v03
Fdx [N]
Time [s]
0
−0.5
−1
−1.5
0.01
0.02
0.03
0.04

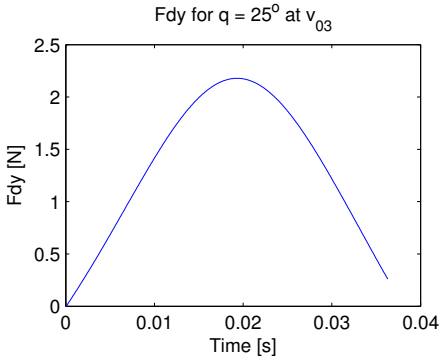
Fdy for q = 25° at v03
Fdy [N]
Time [s]
2.5
2
1.5
1
0.5
0
0.01
0.02
0.03
0.04

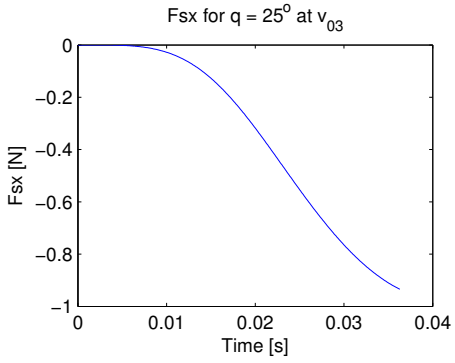
Fsx for q = 25° at v03
Fsx [N]
Time [s]
0
−0.2
−0.4
−0.6
−0.8
−1
0.01
0.02
0.03
0.04

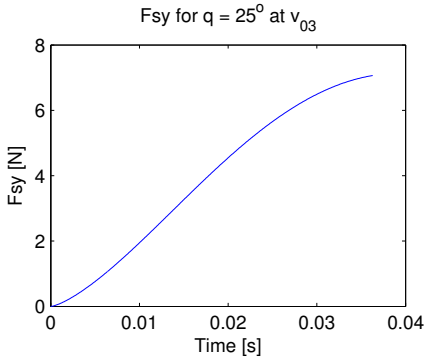
Fsy for q = 25° at v03
Fsy [N]
Time [s]
8
6
4
2
0
0.01
0.02
0.03
0.04

D.5 Force Components for q = 35^o

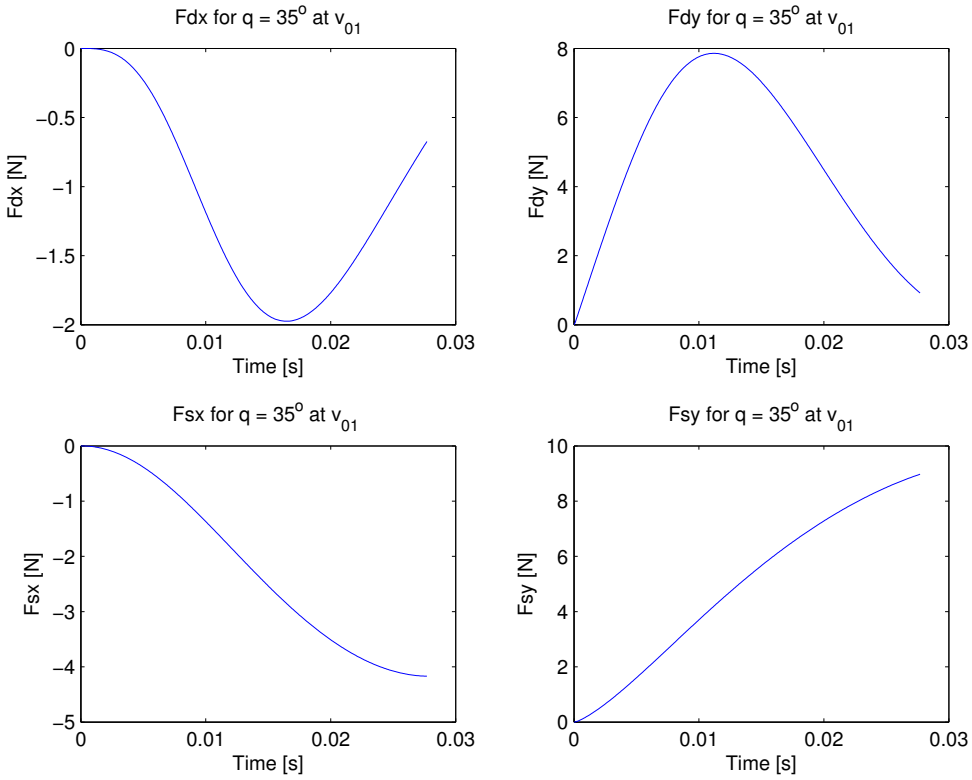

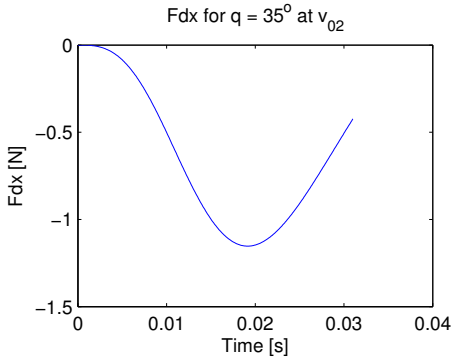
Fdx for q = 35° at v02
Fdx [N]
Time [s]
0
−0.5
−1
−1.5
0
0.01
0.02
0.03
0.04

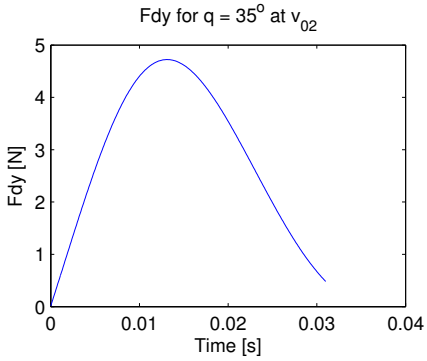
Fdy for q = 35° at v02
Fdy [N]
Time [s]
5
4
3
2
1
0
0
0.01
0.02
0.03
0.04

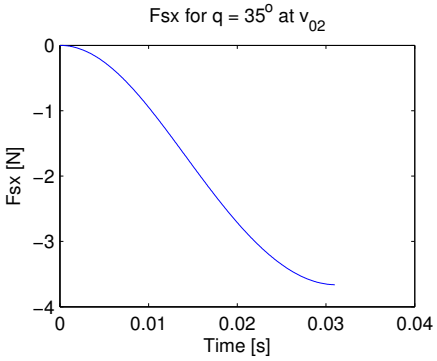
Fsx for q = 35° at v02
Fsx [N]
Time [s]
0
−1
−2
−3
−4
0
0.01
0.02
0.03
0.04

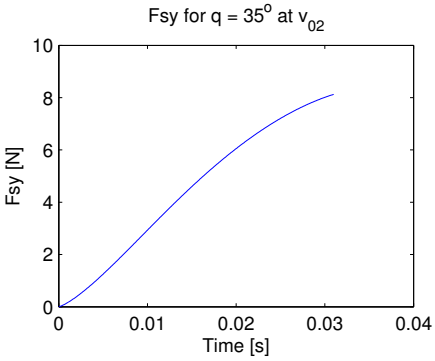
Fsy for q = 35° at v02
Fsy [N]
Time [s]
10
8
6
4
2
0
0
0.01
0.02
0.03
0.04

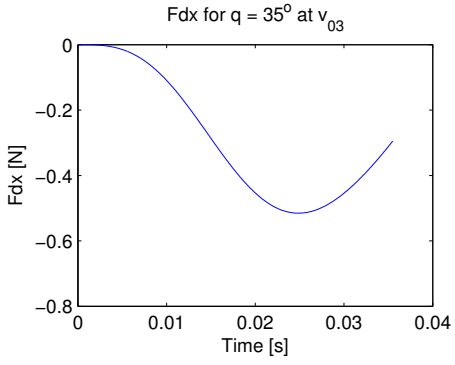
Fdx for q = 35° at v03
Fdx [N]
Time [s]
0
−0.2
−0.4
−0.6
−0.8
0
0.01
0.02
0.03
0.04

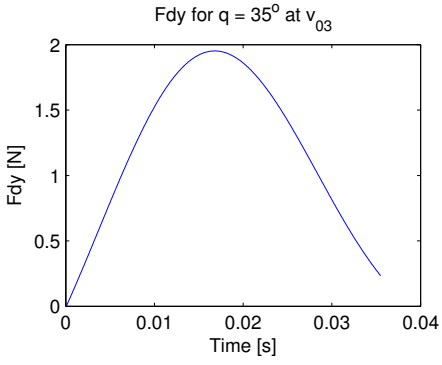
Fdy for q = 35° at v03
Fdy [N]
Time [s]
2
1.5
1
0.5
0
0
0.01
0.02
0.03
0.04

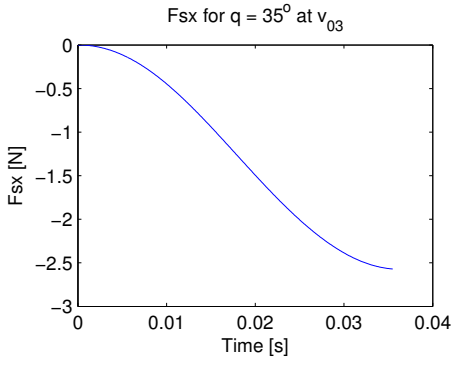
Fsx for q = 35° at v03
Fsx [N]
Time [s]
0
−0.5
−1
−1.5
−2
−2.5
−3
0
0.01
0.02
0.03
0.04

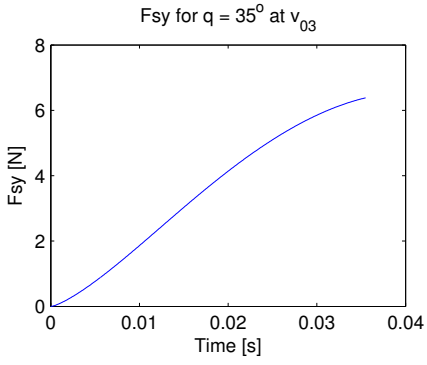
Fsy for q = 35° at v03
Fsy [N]
Time [s]
8
6
4
2
0
0
0.01
0.02
0.03
0.04

D.6 Force Components for q = 45^o

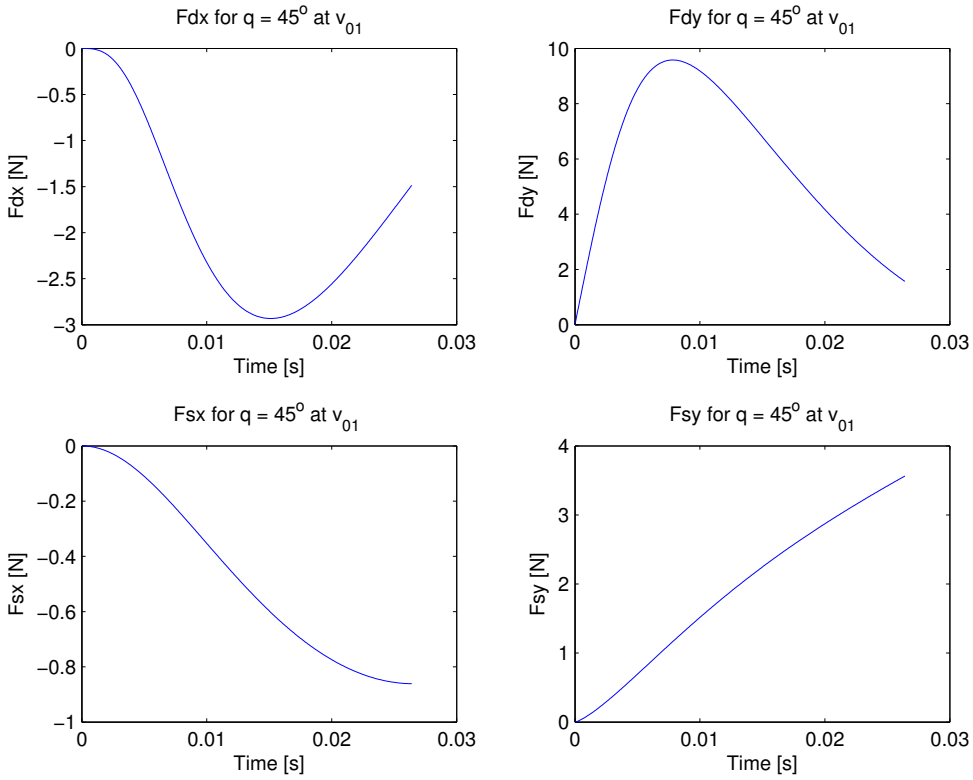

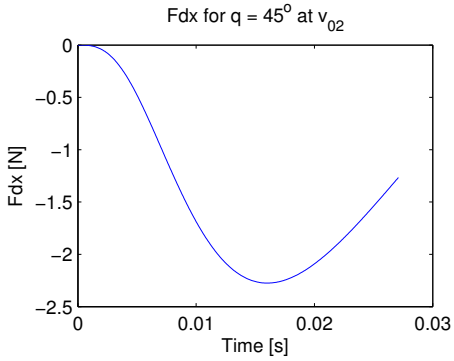
Fdx for q = 45° at v02
Fdx [N]
Time [s]
0
−0.5
−1
−1.5
−2
−2.5
0
0.01
0.02
0.03

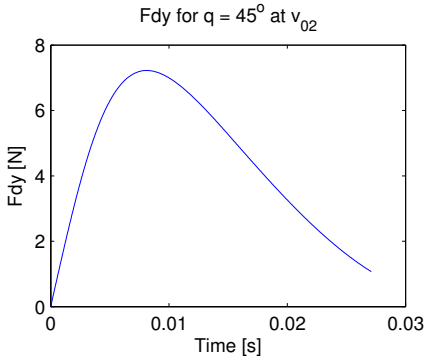
Fdy for q = 45° at v02
Fdy [N]
Time [s]
8
6
4
2
0
0
0.01
0.02
0.03

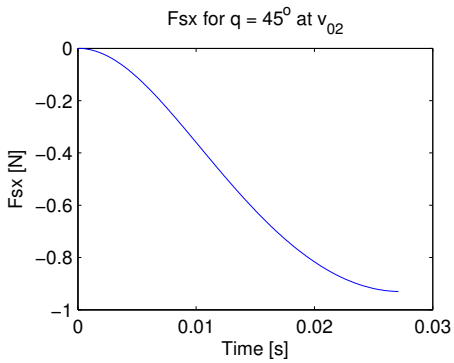
Fsx for q = 45° at v02
Fsx [N]
Time [s]
0
−0.2
−0.4
−0.6
−0.8
−1
0
0.01
0.02
0.03

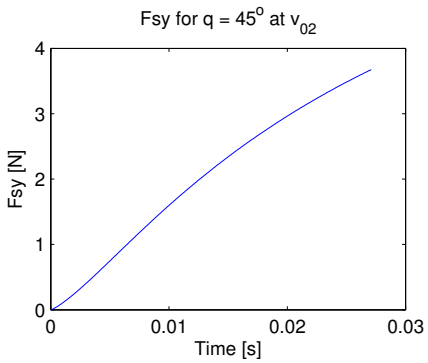
Fsy for q = 45° at v02
Fsy [N]
Time [s]
4
3
2
1
0
0
0.01
0.02
0.03

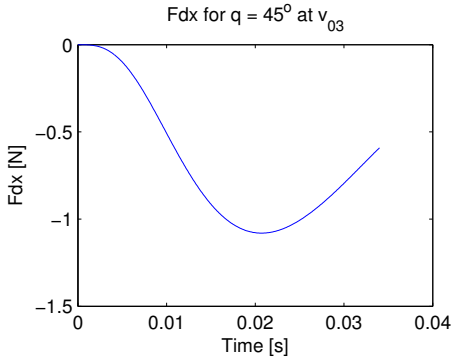
Fdx for q = 45° at v03
Fdx [N]
Time [s]
0
−0.5
−1
−1.5
0
0.01
0.02
0.03
0.04

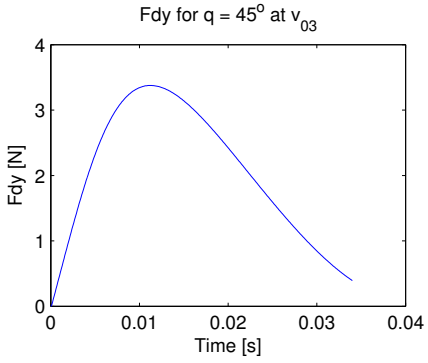
Fdy for q = 45° at v03
Fdy [N]
Time [s]
4
3
2
1
0
0
0.01
0.02
0.03
0.04

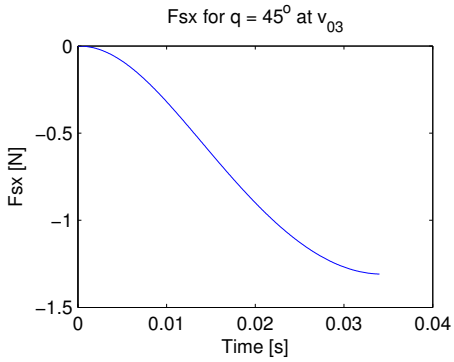
Fsx for q = 45° at v03
Fsx [N]
Time [s]
0
−0.5
−1
−1.5
0
0.01
0.02
0.03
0.04

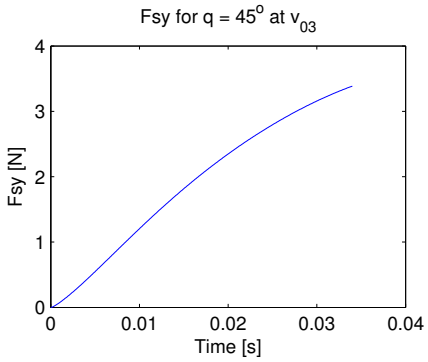
Fsy for q = 45° at v03
Fsy [N]
Time [s]
4
3
2
1
0
0
0.01
0.02
0.03
0.04

D.7 Force Components for q = 55^o

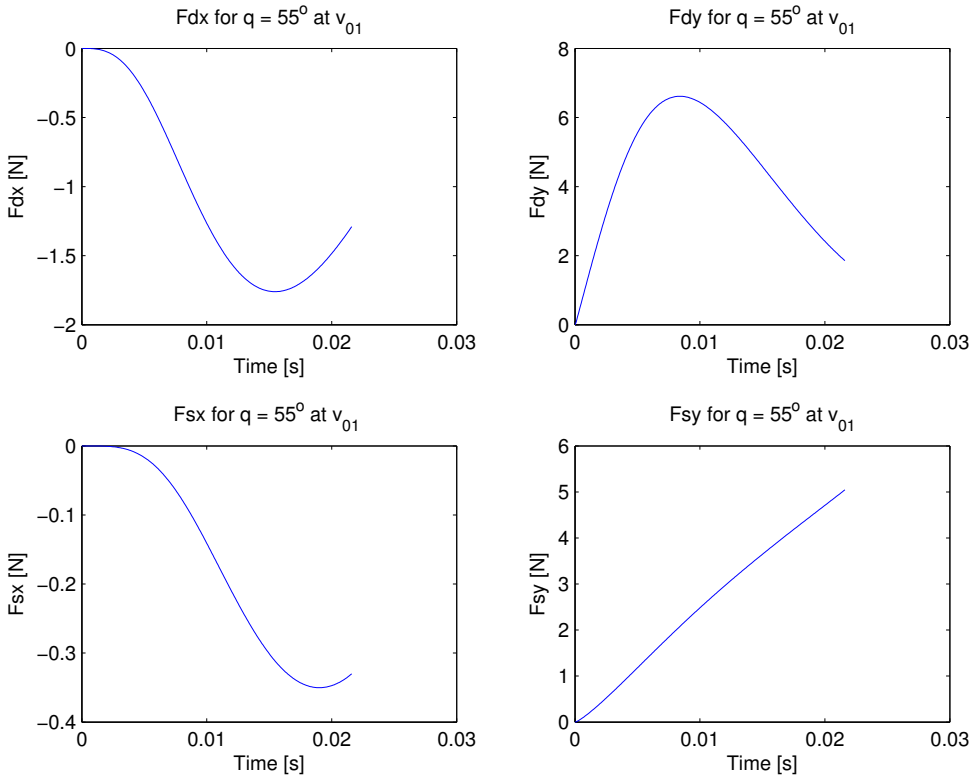

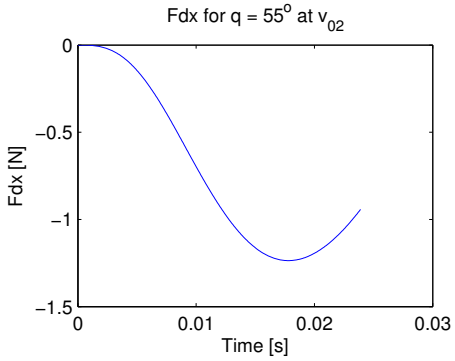
Fdx for q = 55° at v02
Fdx [N]
Time [s]
0
−0.5
−1
−1.5
0
0.01
0.02
0.03

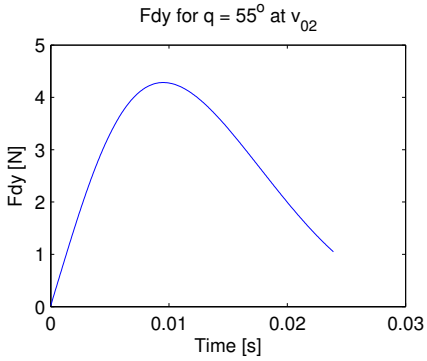
Fdy for q = 55° at v02
Fdy [N]
Time [s]
5
4
3
2
1
0
0
0.01
0.02
0.03

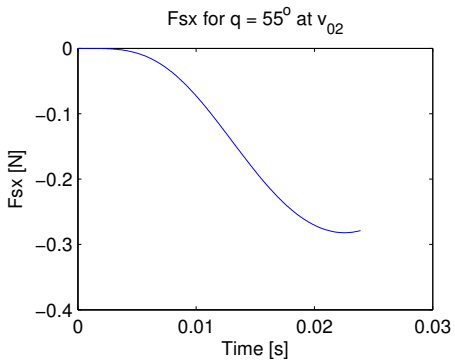
Fsx for q = 55° at v02
Fsx [N]
Time [s]
0
−0.1
−0.2
−0.3
−0.4
0
0.01
0.02
0.03

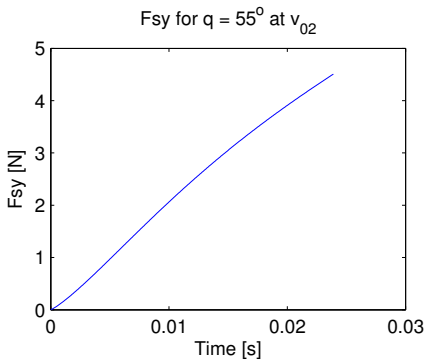
Fsy for q = 55° at v02
Fsy [N]
Time [s]
5
4
3
2
1
0
0
0.01
0.02
0.03

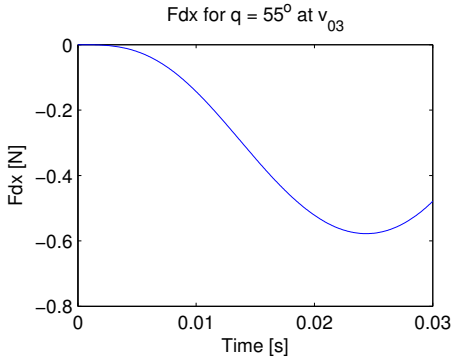
Fdx for q = 55° at v03
Fdx [N]
Time [s]
0
−0.2
−0.4
−0.6
−0.8
0
0.01
0.02
0.03

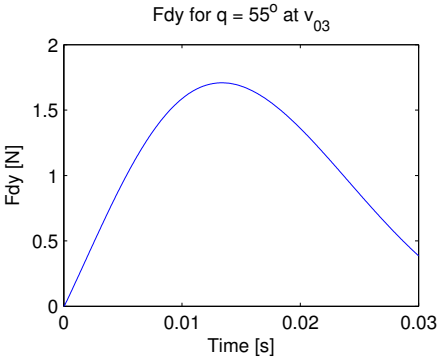
Fdy for q = 55° at v03
Fdy [N]
Time [s]
2
1.5
1
0.5
0
0
0.01
0.02
0.03

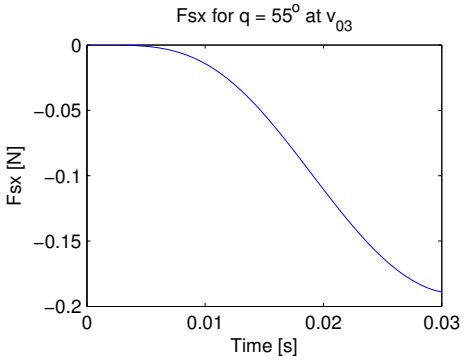
Fsx for q = 55° at v03
Fsx [N]
Time [s]
0
−0.05
−0.1
−0.15
−0.2
0
0.01
0.02
0.03

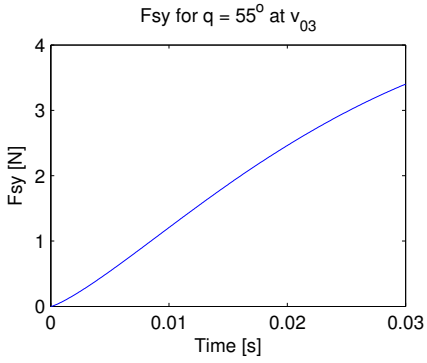
Fsy for q = 55° at v03
Fsy [N]
Time [s]
4
3
2
1
0
0
0.01
0.02
0.03

D.8 Force Components for q = 65^o

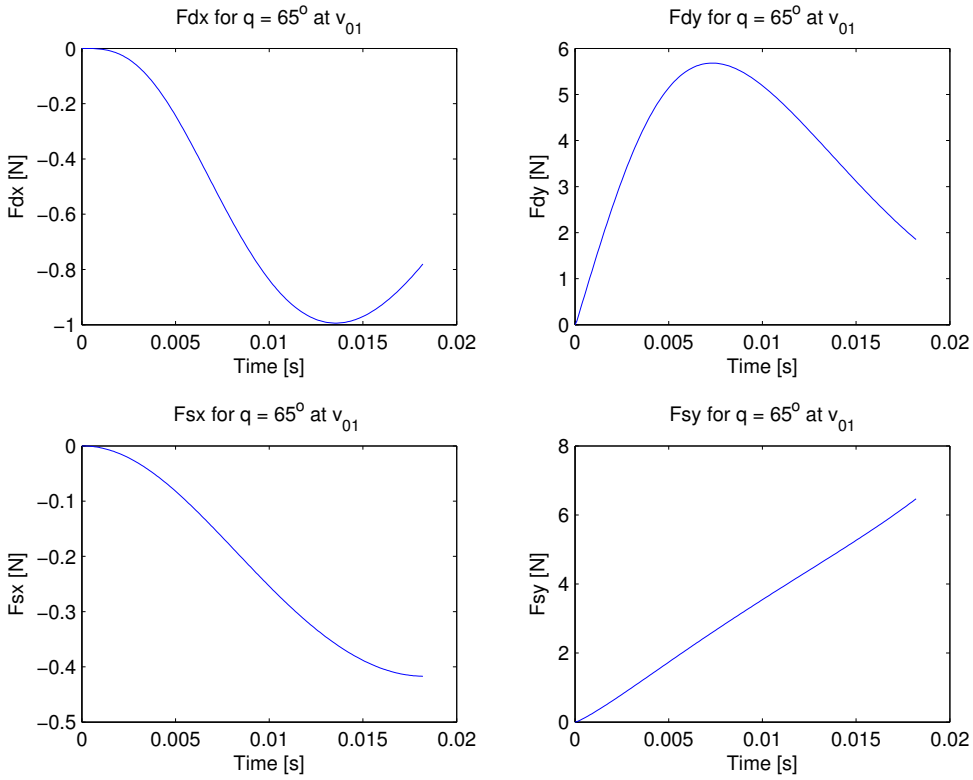

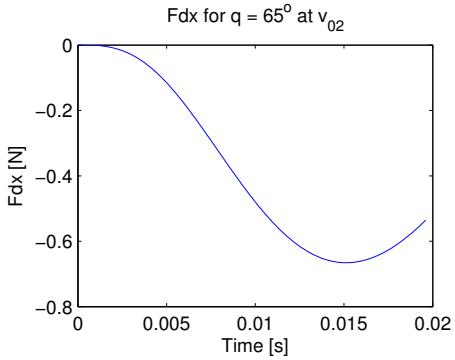
Fdx for q = 65° at v02
Fdx [N]
Time [s]
0
−0.2
−0.4
−0.6
−0.8
0.005
0.01
0.015
0.02

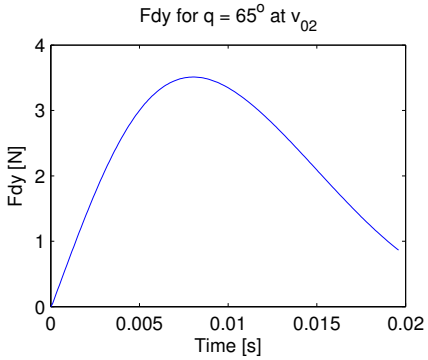
Fdy for q = 65° at v02
Fdy [N]
Time [s]
4
3
2
1
0
0.005
0.01
0.015
0.02

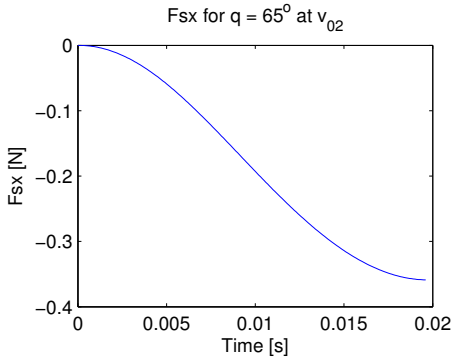
Fsx for q = 65° at v02
Fsx [N]
Time [s]
0
−0.1
−0.2
−0.3
−0.4
0.005
0.01
0.015
0.02

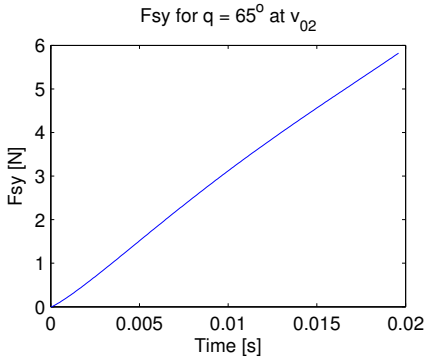
Fsy for q = 65° at v02
Fsy [N]
Time [s]
6
5
4
3
2
1
0
0.005
0.01
0.015
0.02

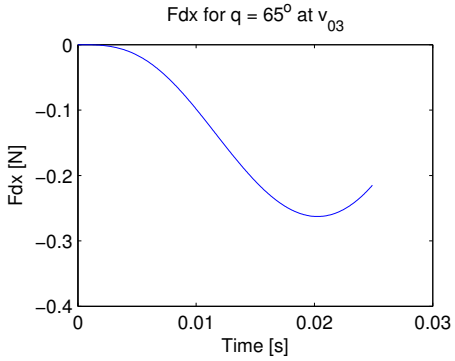
Fdx for q = 65° at v03
Fdx [N]
Time [s]
0
−0.1
−0.2
−0.3
−0.4
0.01
0.02
0.03

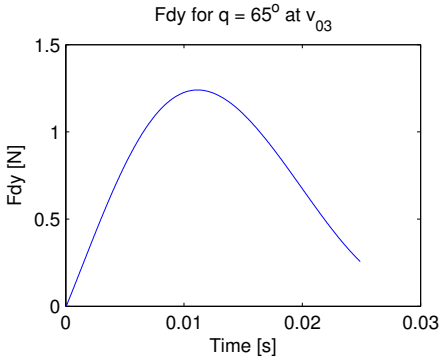
Fdy for q = 65° at v03
Fdy [N]
Time [s]
1.5
1
0.5
0
0.01
0.02
0.03

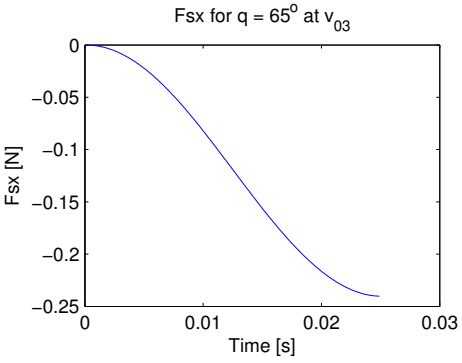
Fsx for q = 65° at v03
Fsx [N]
Time [s]
0
−0.05
−0.1
−0.15
−0.2
−0.25
0.01
0.02
0.03

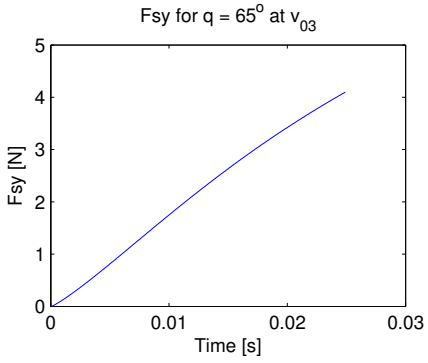
Fsy for q = 65° at v03
Fsy [N]
Time [s]
5
4
3
2
1
0
0.01
0.02
0.03

D.9 Force Components for q = 75^o

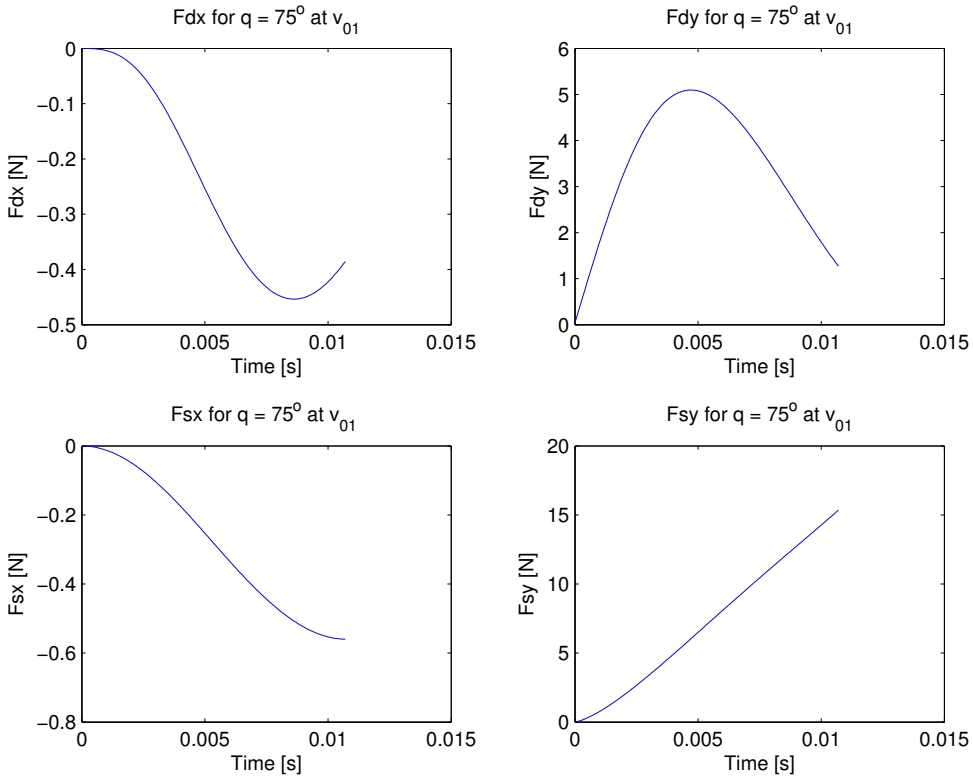

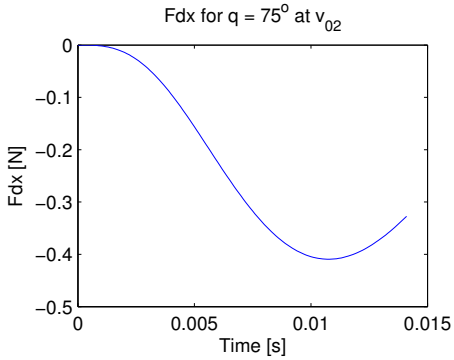
Fdx for q = 75° at v02
Fdx [N]
Time [s]
0
−0.1
−0.2
−0.3
−0.4
−0.5
0.005
0.01
0.015

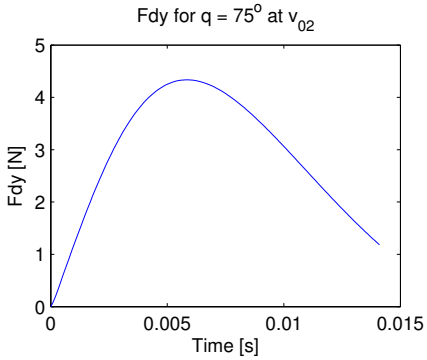
Fdy for q = 75° at v02
Fdy [N]
Time [s]
5
4
3
2
1
0
0.005
0.01
0.015

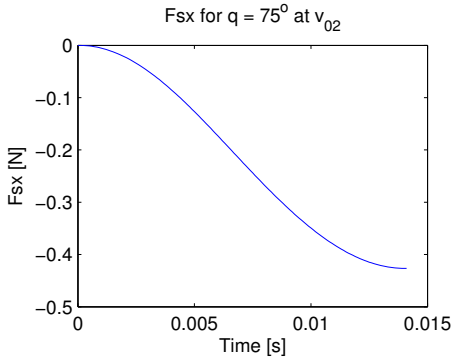
Fsx for q = 75° at v02
Fsx [N]
Time [s]
0
−0.1
−0.2
−0.3
−0.4
−0.5
0.005
0.01
0.015

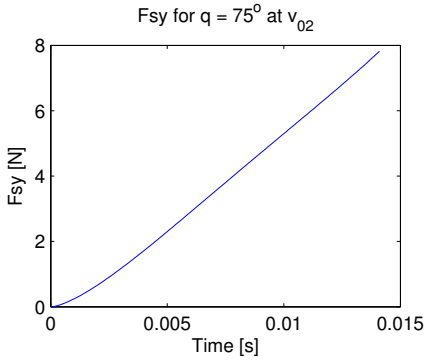
Fsy for q = 75° at v02
Fsy [N]
Time [s]
8
6
4
2
0
0.005
0.01
0.015

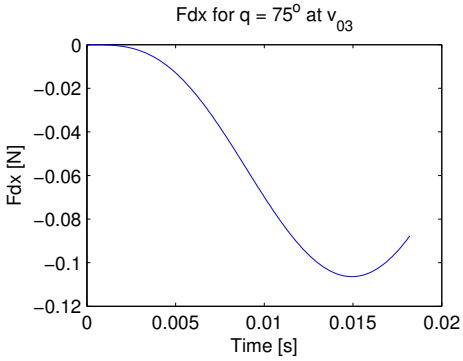
Fdx for q = 75° at v03
Fdx [N]
Time [s]
0
−0.02
−0.04
−0.06
−0.08
−0.1
−0.12
0.005
0.01
0.015
0.02

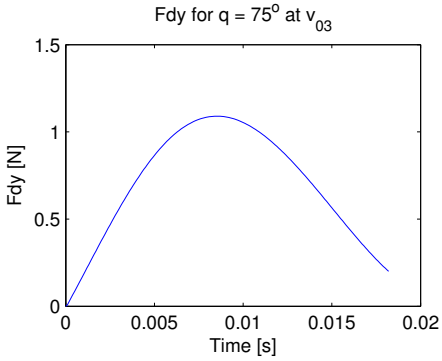
Fdy for q = 75° at v03
Fdy [N]
Time [s]
1.5
1
0.5
0
0.005
0.01
0.015
0.02

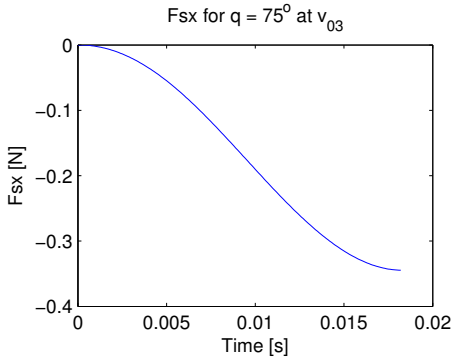
Fsx for q = 75° at v03
Fsx [N]
Time [s]
0
−0.1
−0.2
−0.3
−0.4
0.005
0.01
0.015
0.02

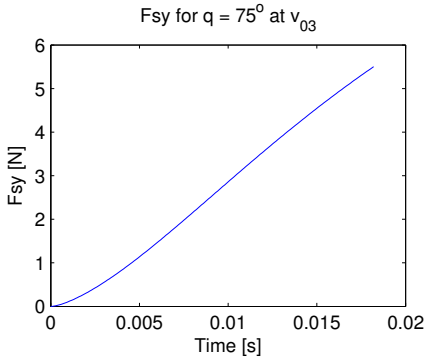
Fsy for q = 75° at v03
Fsy [N]
Time [s]
6
5
4
3
2
1
0
0.005
0.01
0.015
0.02

D.10 Force Components for q = 85^o

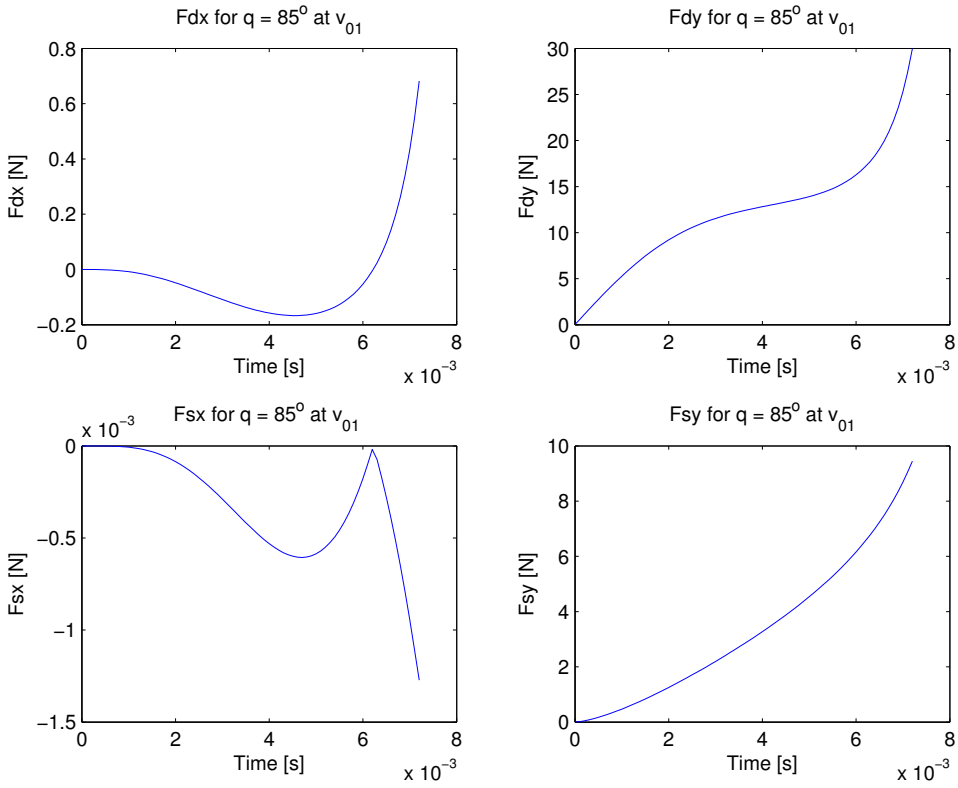

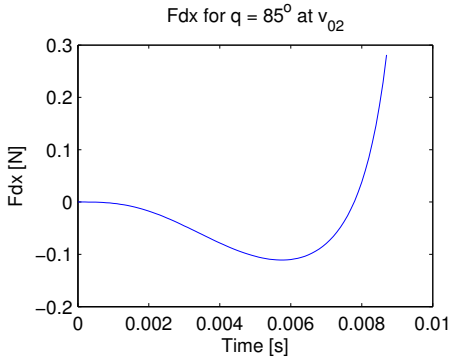
Fdx for q = 85° at v02
Fdx [N]
Time [s]
0.3
0.2
0.1
0
−0.1
−0.2
0
0.002
0.004
0.006
0.008
0.01

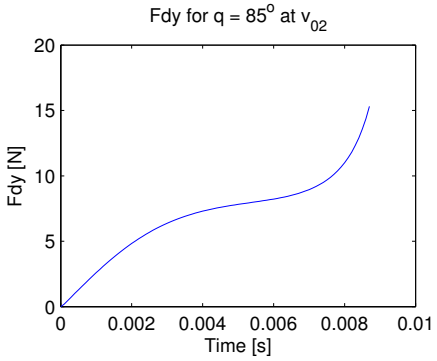
Fdy for q = 85° at v02
Fdy [N]
Time [s]
20
15
10
5
0
0
0.002
0.004
0.006
0.008
0.01

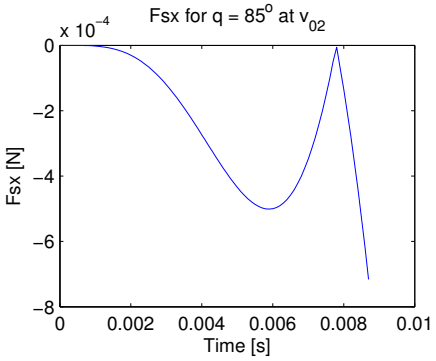
Fsx for q = 85° at v02
x 10−4
Fsx [N]
Time [s]
0
−2
−4
−6
−8
0
0.002
0.004
0.006
0.008
0.01

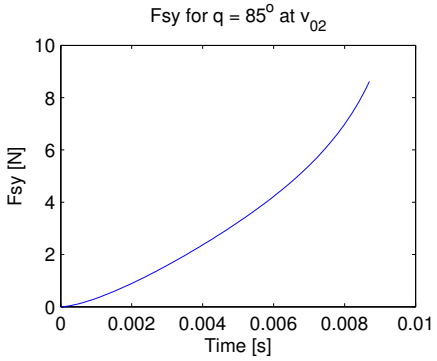
Fsy for q = 85° at v02
Fsy [N]
Time [s]
10
8
6
4
2
0
0
0.002
0.004
0.006
0.008
0.01

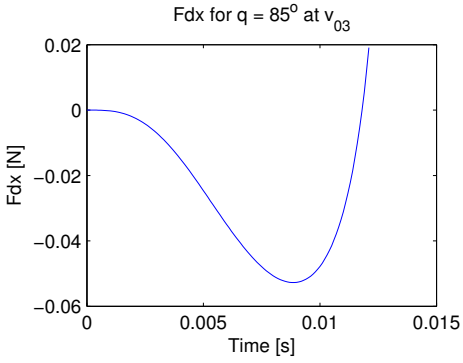
Fdx for q = 85° at v03
Fdx [N]
Time [s]
0.02
0
−0.02
−0.04
−0.06
0
0.005
0.01
0.015

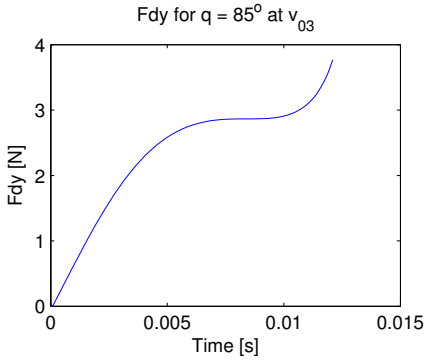
Fdy for q = 85° at v03
Fdy [N]
Time [s]
4
3
2
1
0
0
0.005
0.01
0.015

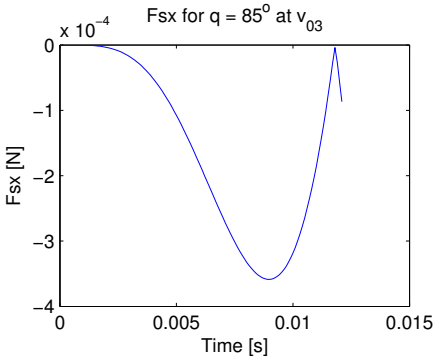
Fsx for q = 85° at v03
x 10−4
Fsx [N]
Time [s]
0
−1
−2
−3
−4
0
0.005
0.01
0.015

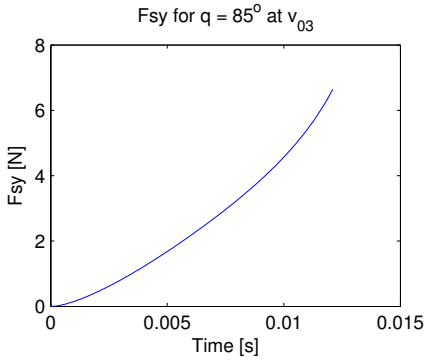
Fsy for q = 85° at v03
Fsy [N]
Time [s]
8
6
4
2
0
0
0.005
0.01
0.015

Appendix E

NDI ToolBench Pipeline

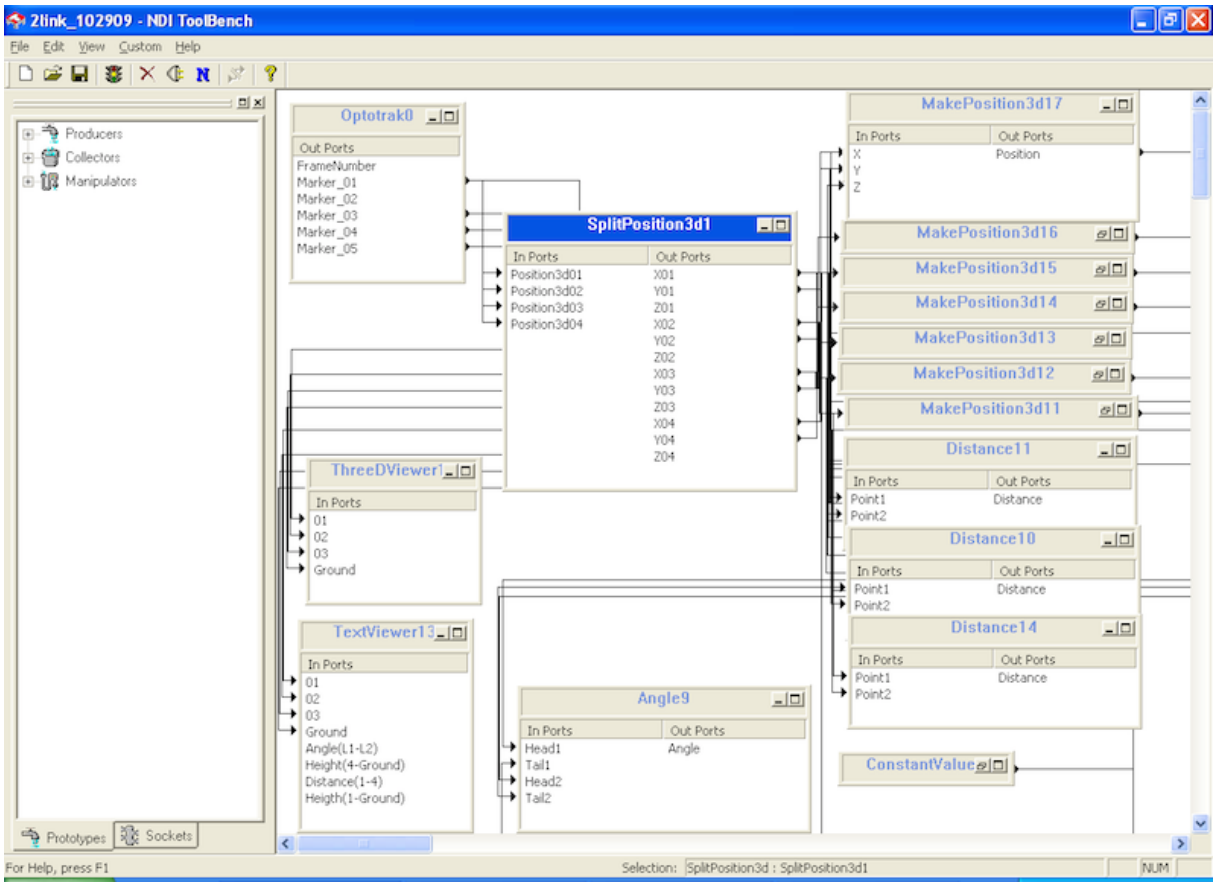

Appendix F

NDI ToolBench 2D-view of the Four IR Markers

The figure below shows the view in 2D of the four markers used in the free link impact experiment.

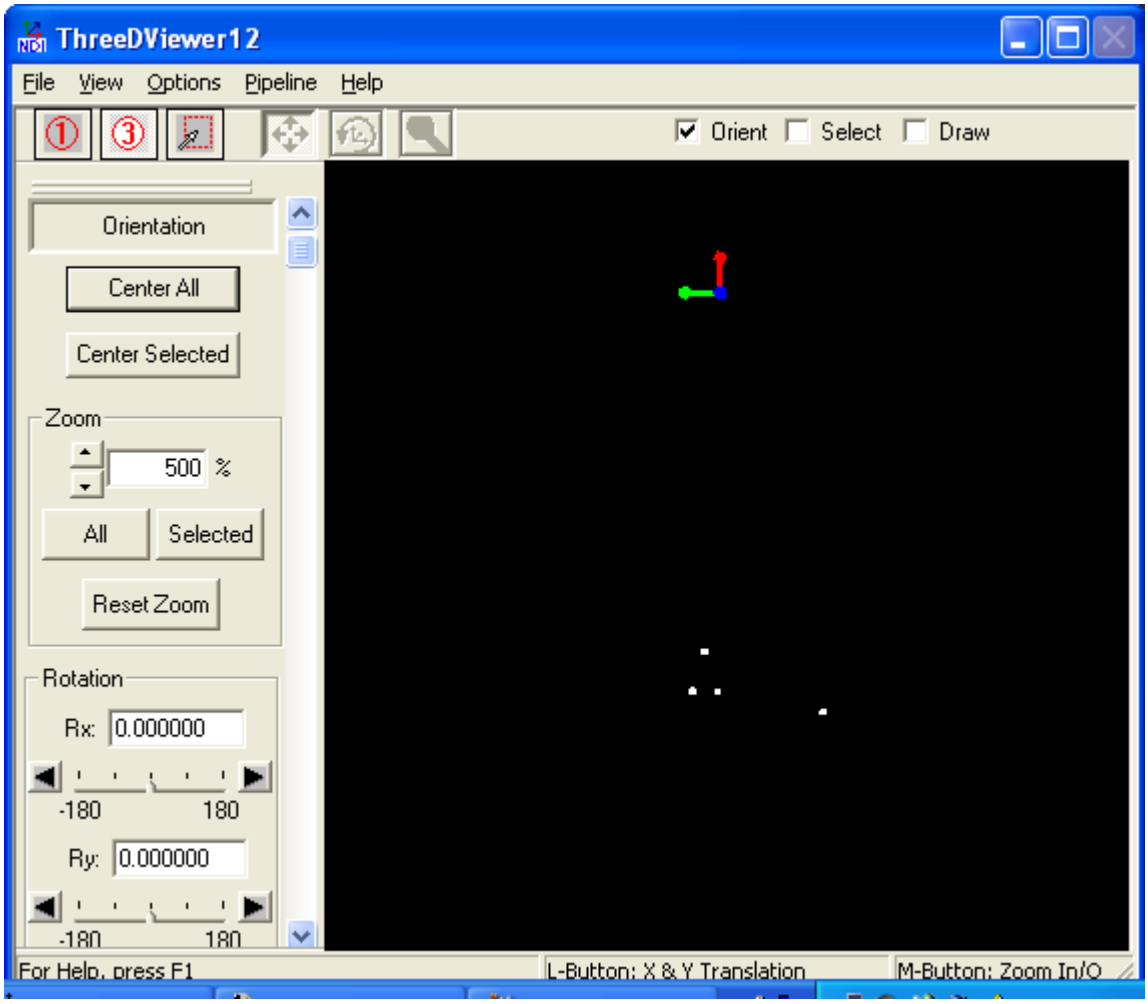

Appendix G

The Four Resistance Force Components Applied at the End Points The Two-Link Kinematic Chain

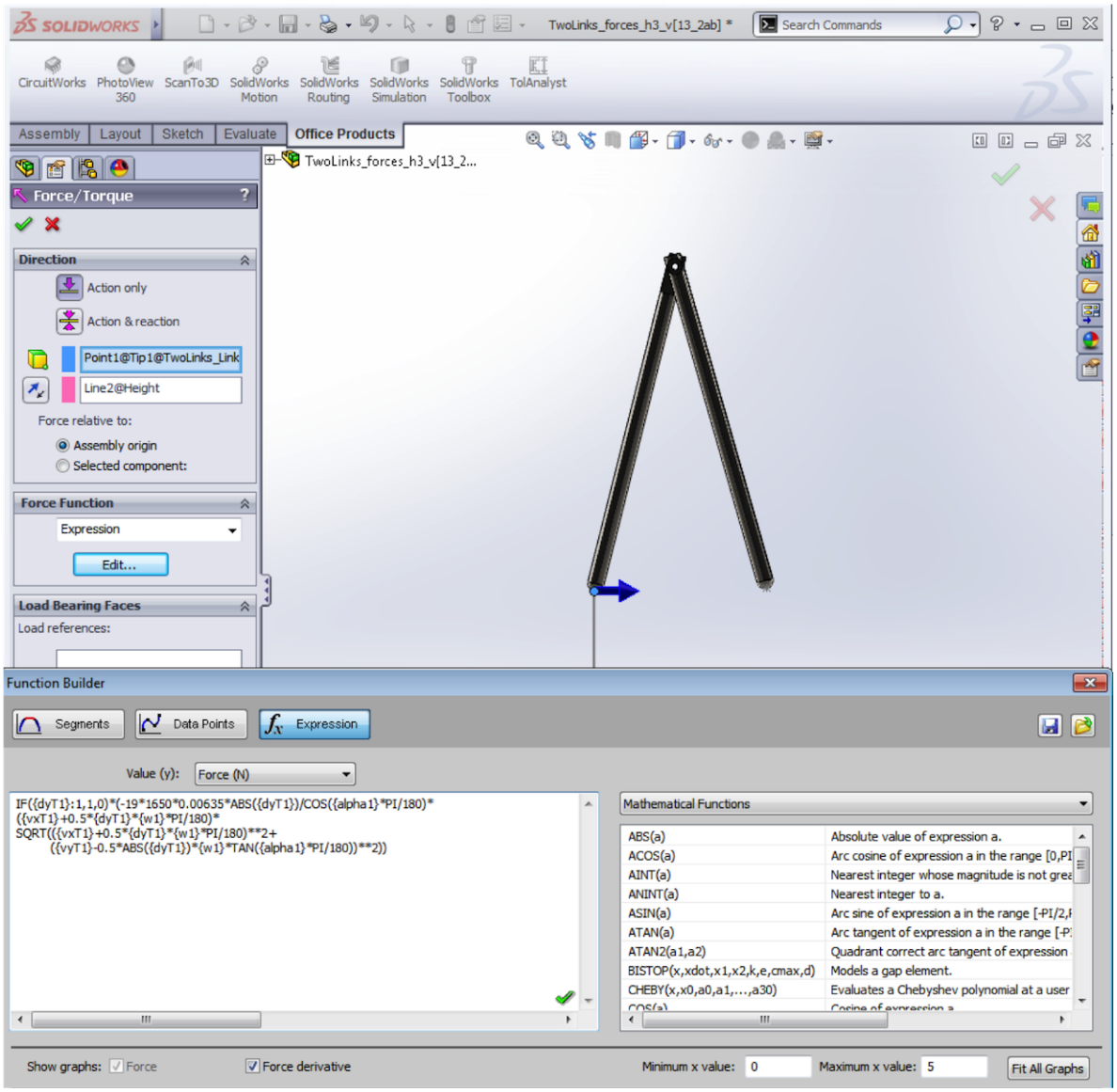

Figure G.1: The horizontal dynamic force applied on link 1

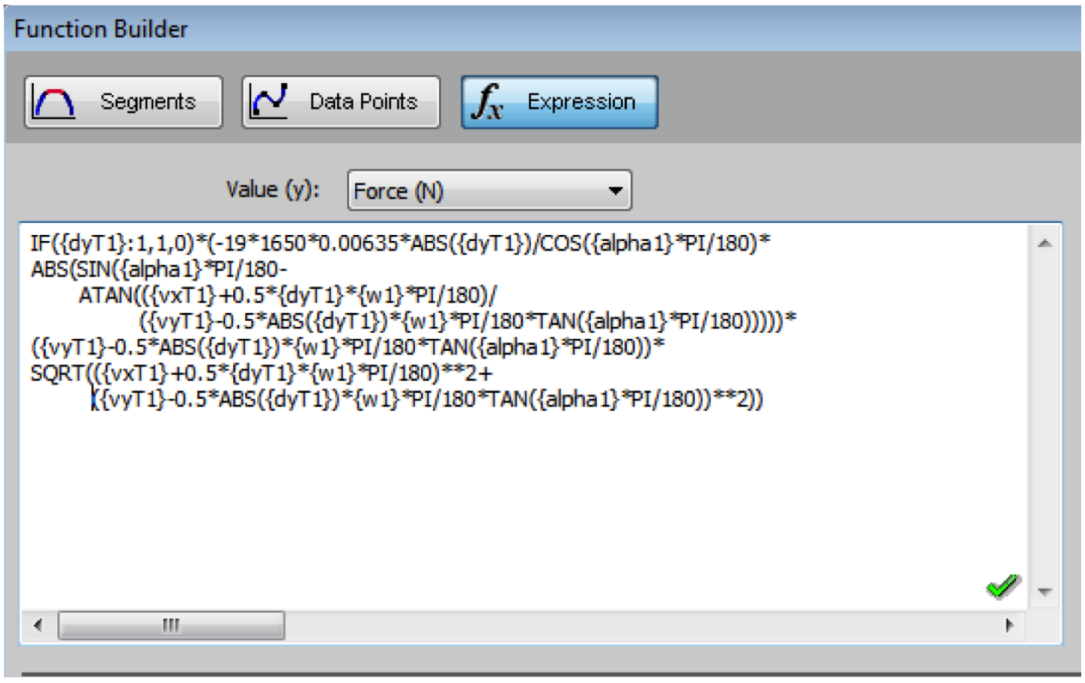

Figure G.2: The vertical dynamic force applied on link 1

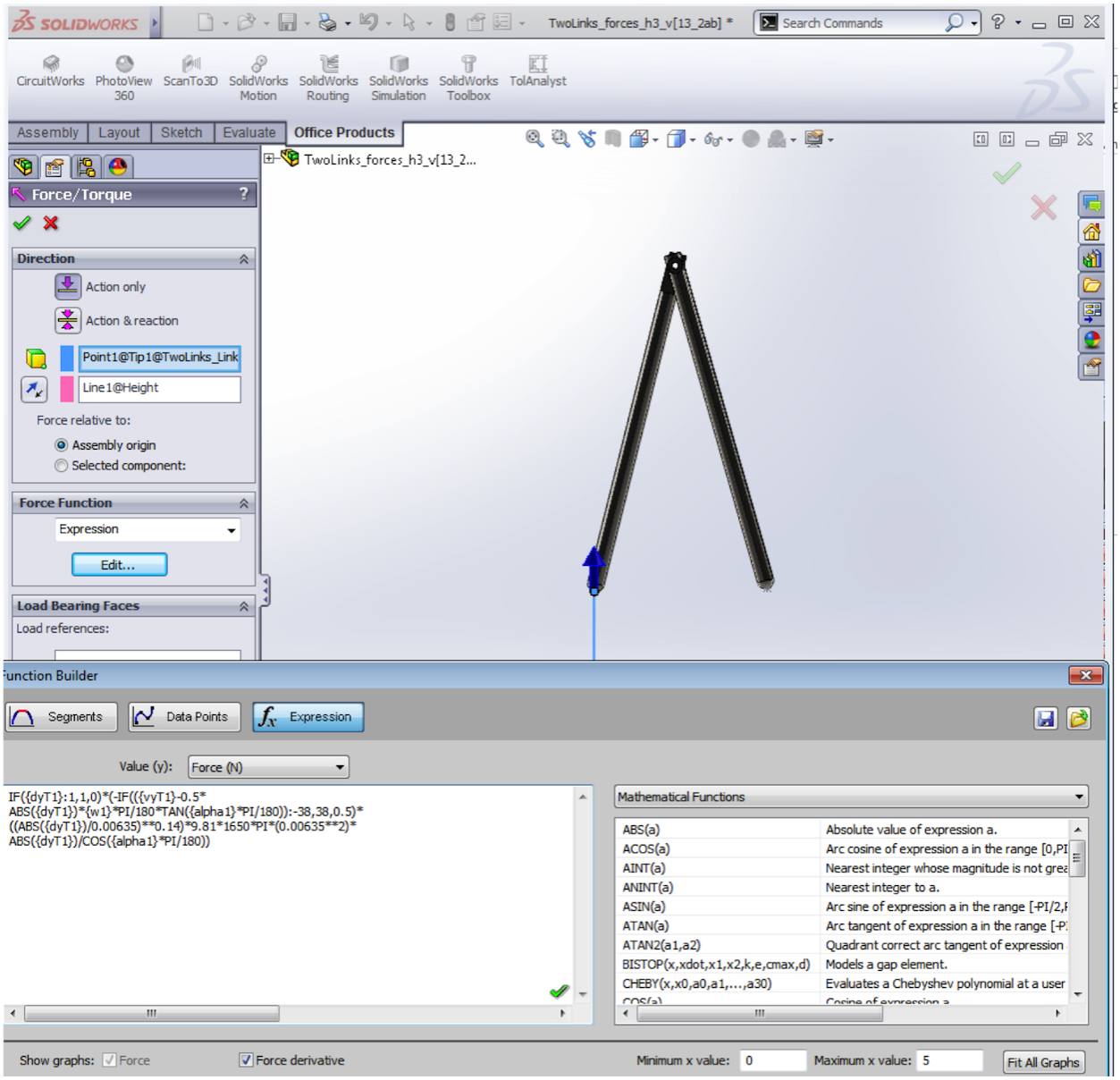

Figure G.3: The vertical static force applied on link 1

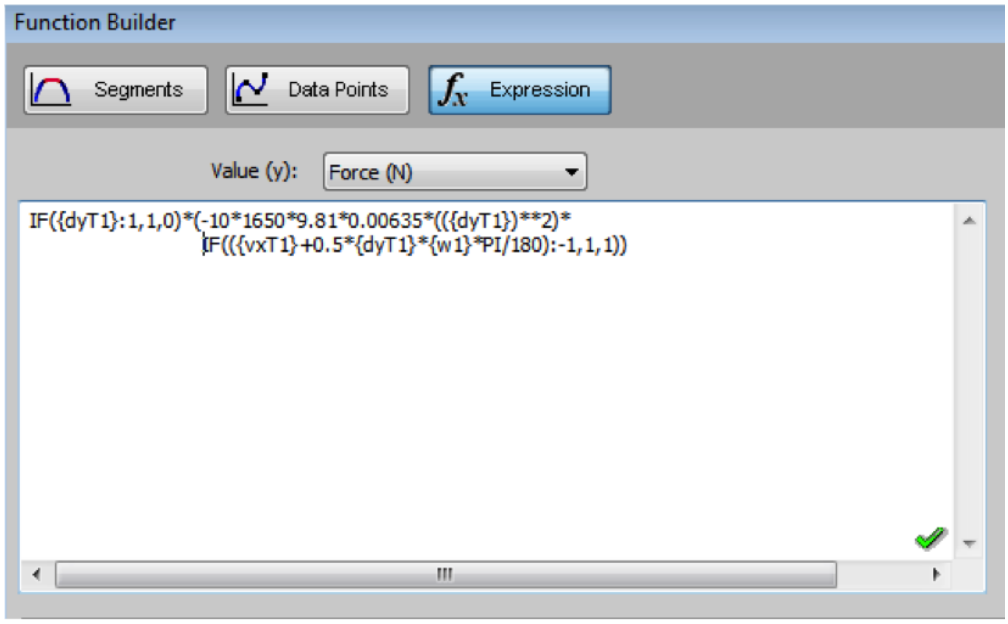

Figure G.4: The horizontal static force applied on link 1

Appendix H

The Resistive Force Components in SolidWorks for the Two Links Model

H.1 Force Components for Link 1

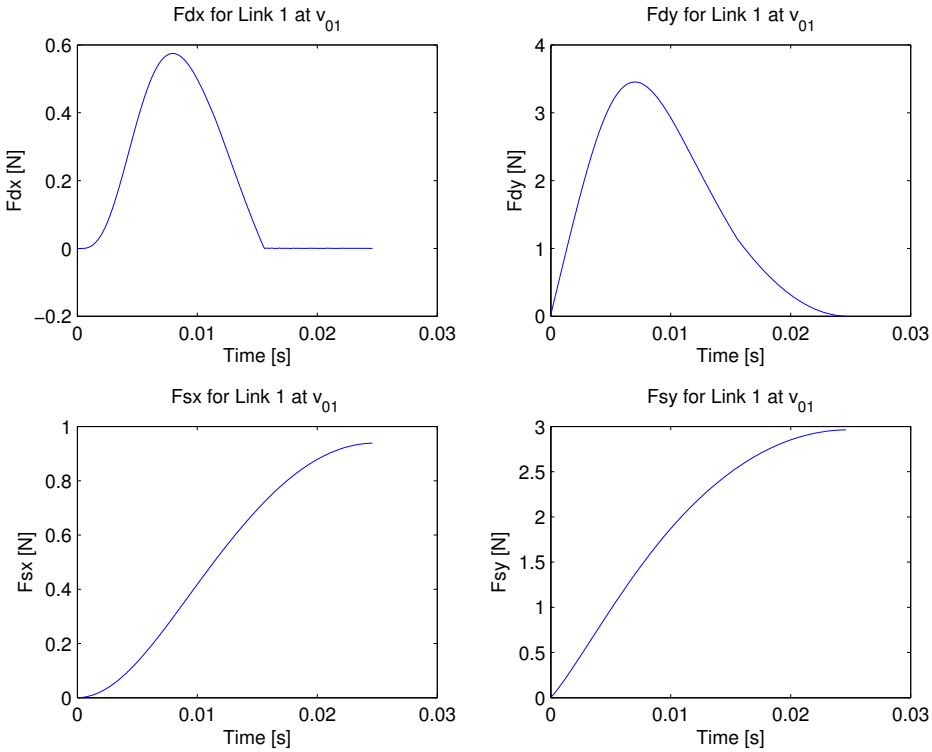

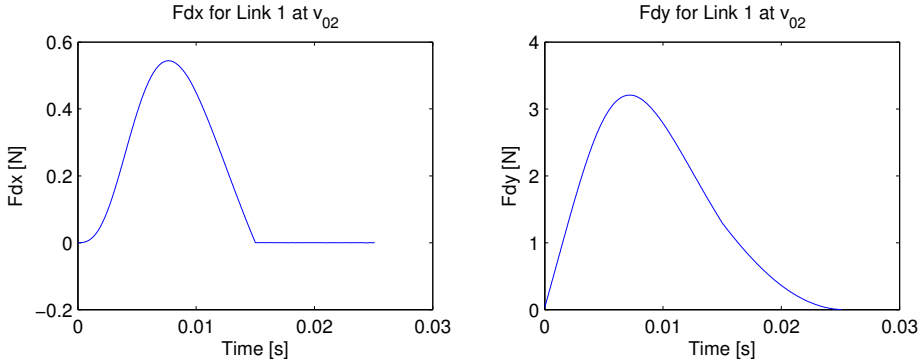
Fdx for Link 1 at v_{02}
Fdx [N]
Time [s]
0.6
0.4
0.2
0
−0.2
0
0.01
0.02
0.03

Fdy for Link 1 at v_{02}
Fdy [N]
Time [s]
4
3
2
1
0
0
0.01
0.02
0.03

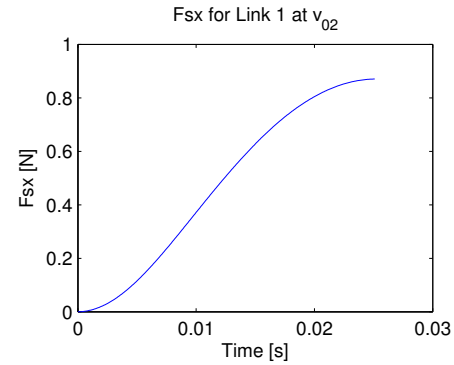
Fsx for Link 1 at v_{02}
Fsx [N]
Time [s]
1
0.8
0.6
0.4
0.2
0
0
0.01
0.02
0.03

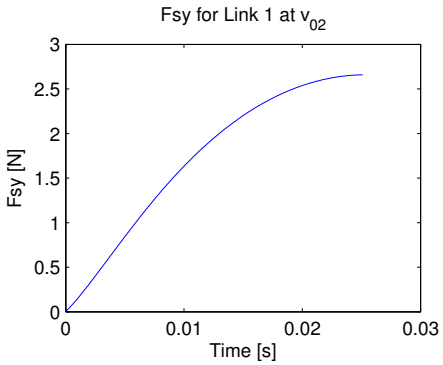
Fsy for Link 1 at v_{02}
Fsy [N]
Time [s]
3
2.5
2
1.5
1
0.5
0
0
0.01
0.02
0.03

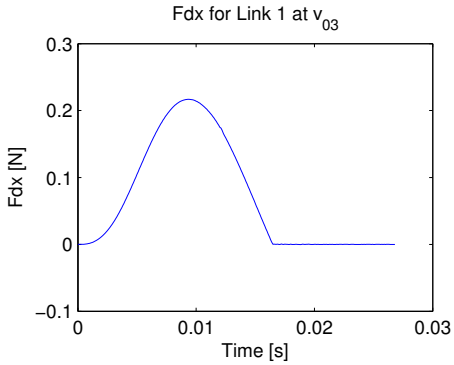
Fdx for Link 1 at v_{03}
Fdx [N]
Time [s]
0.3
0.2
0.1
0
−0.1
0
0.01
0.02
0.03

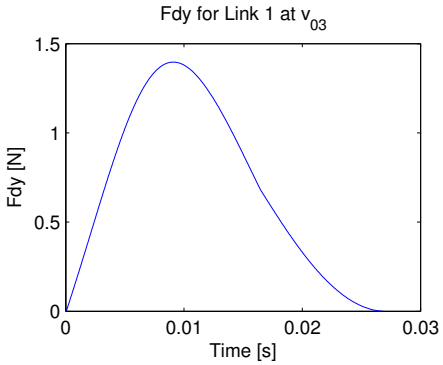
Fdy for Link 1 at v_{03}
Fdy [N]
Time [s]
1.5
1
0.5
0
0
0.01
0.02
0.03

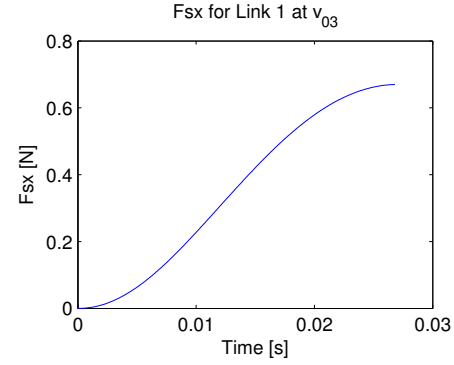
Fsx for Link 1 at v_{03}
Fsx [N]
Time [s]
0.8
0.6
0.4
0.2
0
0
0.01
0.02
0.03

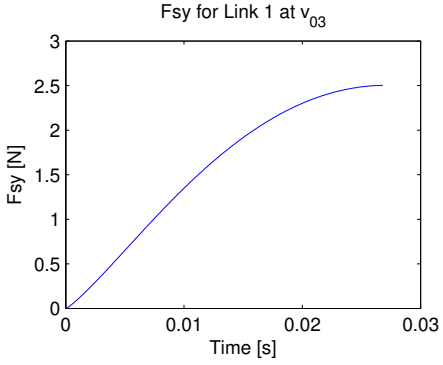
Fsy for Link 1 at v_{03}
Fsy [N]
Time [s]
3
2.5
2
1.5
1
0.5
0
0
0.01
0.02
0.03

H.2 Force Components for Link 2

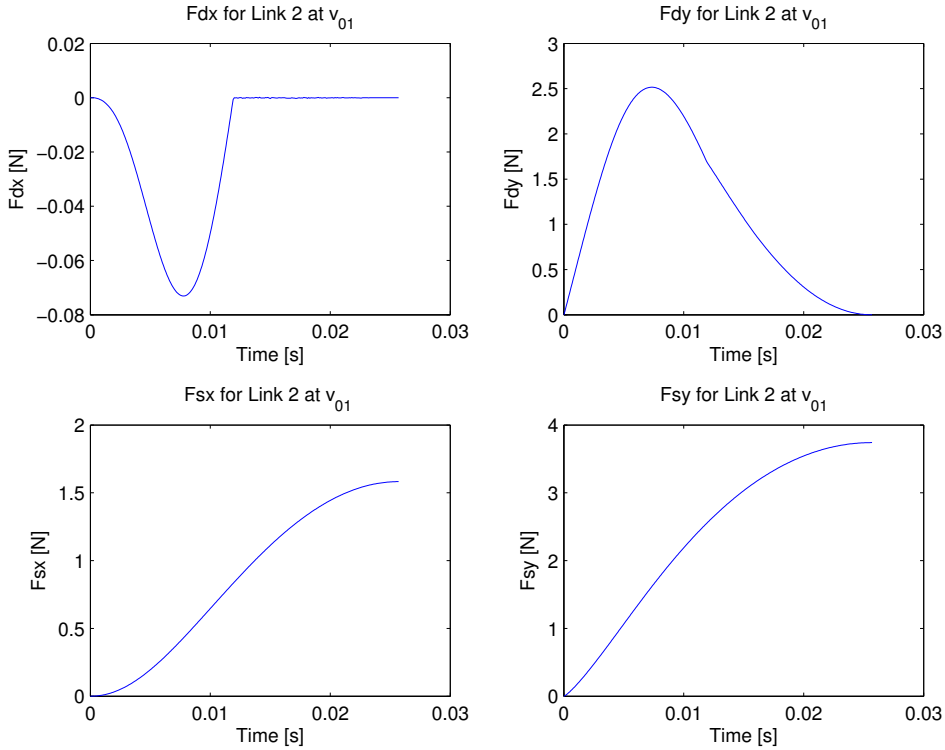

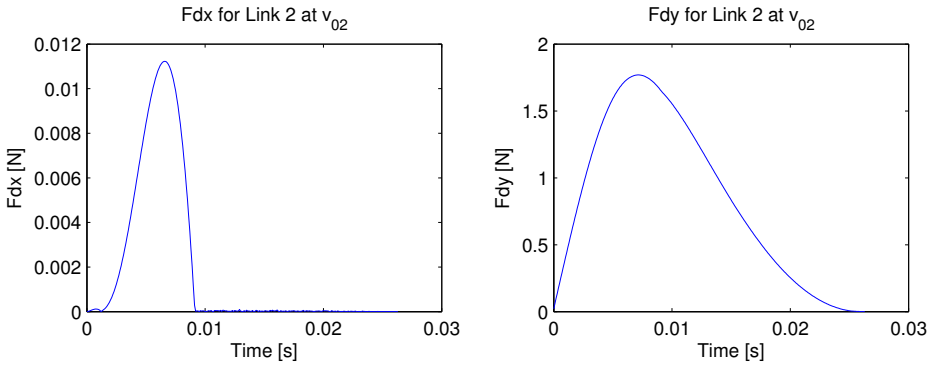
Fdx for Link 2 at v_{02}
Fdx [N]
0.012
0.01
0.008
0.006
0.004
0.002
0
0
0.01
0.02
0.03
Time [s]

Fdy for Link 2 at v_{02}
Fdy [N]
2
1.5
1
0.5
0
0
0.01
0.02
0.03
Time [s]

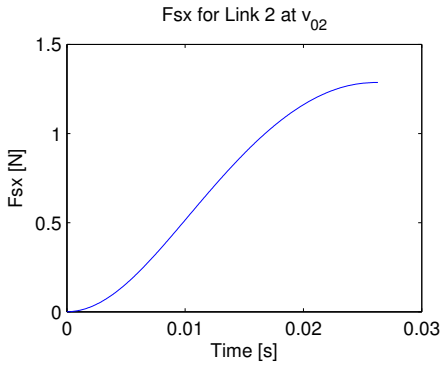
Fsx for Link 2 at v_{02}
Fsx [N]
1.5
1
0.5
0
0
0.01
0.02
0.03
Time [s]

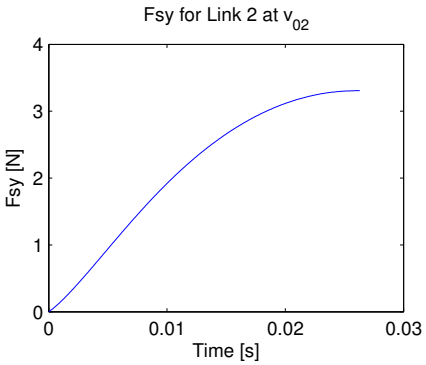
Fsy for Link 2 at v_{02}
Fsy [N]
4
3
2
1
0
0
0.01
0.02
0.03
Time [s]

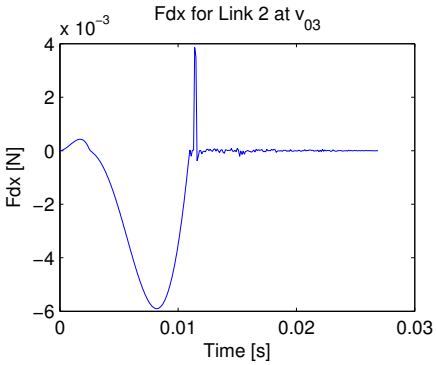
Fdx for Link 2 at v_{03}
x 10^{-3}
Fdx [N]
4
2
0
−2
−4
−6
0
0.01
0.02
0.03
Time [s]

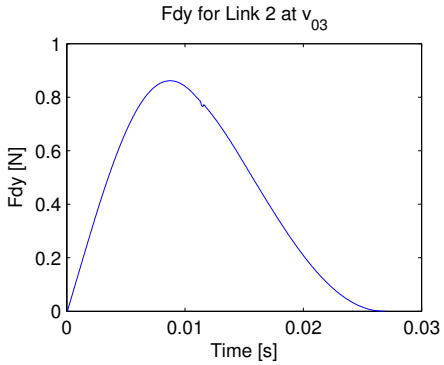
Fdy for Link 2 at v_{03}
Fdy [N]
1
0.8
0.6
0.4
0.2
0
0
0.01
0.02
0.03
Time [s]

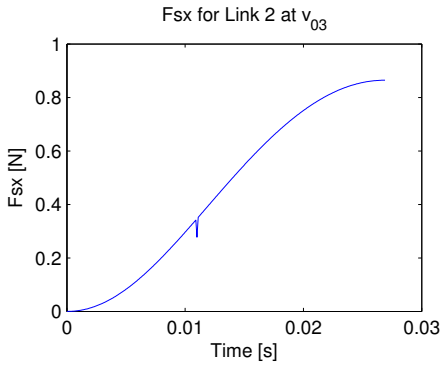
Fsx for Link 2 at v_{03}
Fsx [N]
1
0.8
0.6
0.4
0.2
0
0
0.01
0.02
0.03
Time [s]

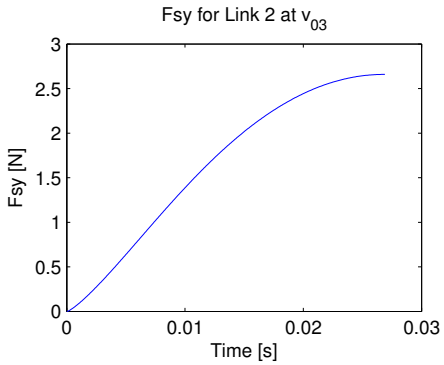
Fsy for Link 2 at v_{03}
Fsy [N]
3
2.5
2
1.5
1
0.5
0
0
0.01
0.02
0.03
Time [s]

Appendix I

Scaled Human Model for Motion Capture

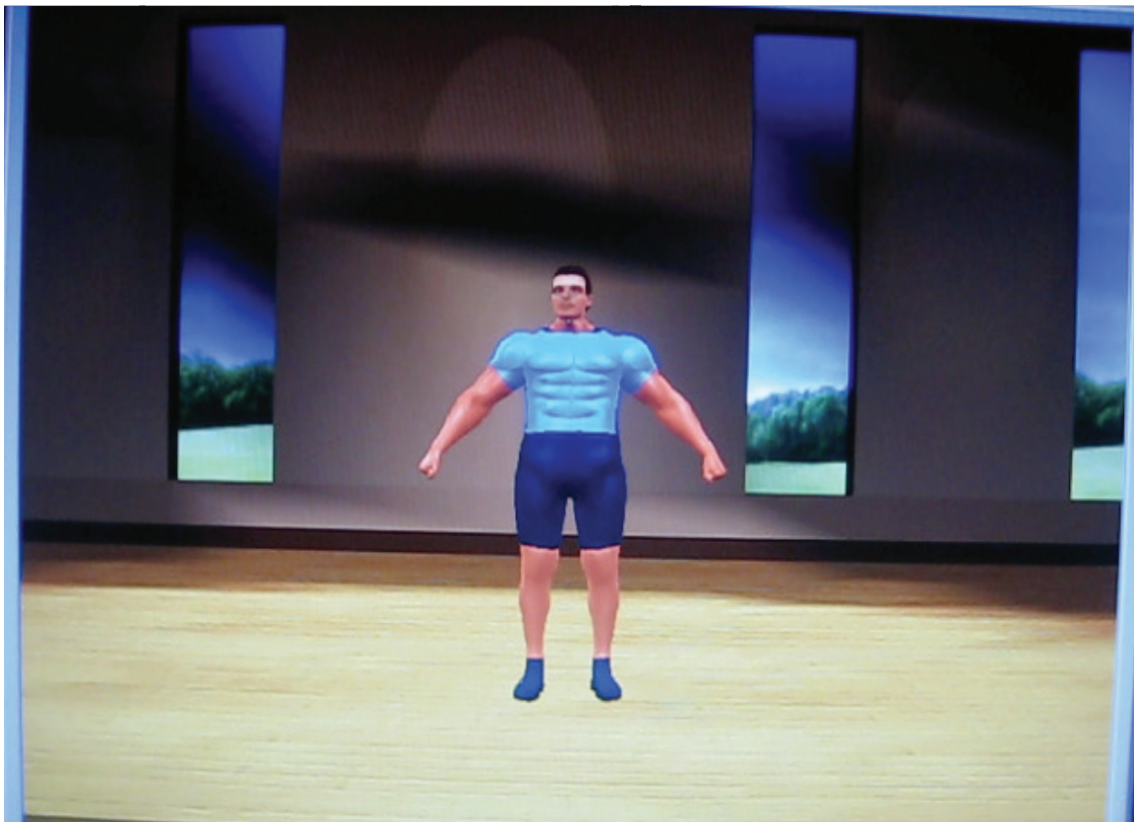

Appendix J

Experimental Results: Depth and Velocity with Time During Impact for Each Subject

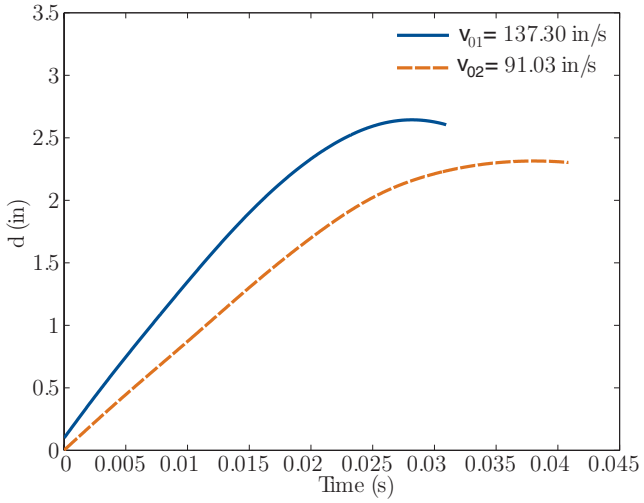

(a) Depth with time for Subject 1

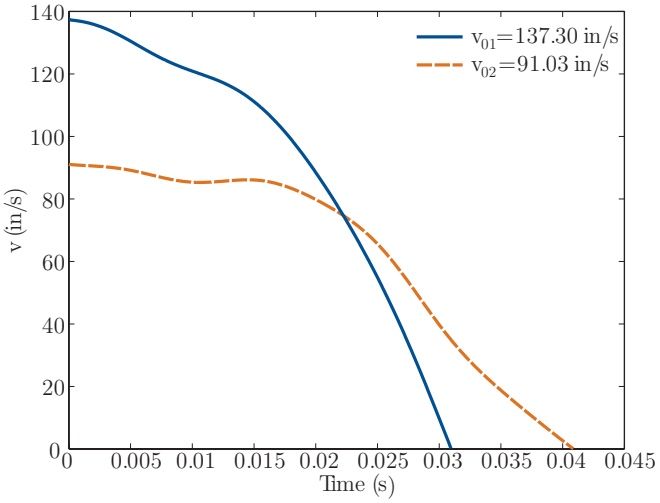

(b) Velocity with time for Subject 1

Figure J.1: The average experimental impact results for Subject 1: (a) Displacement during impact, and (b) Velocity during impact

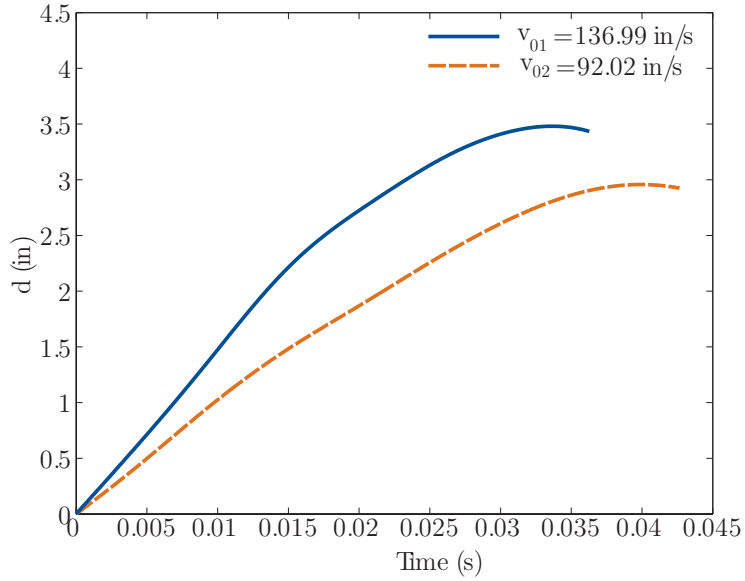

(a) Depth with time for Subject 2

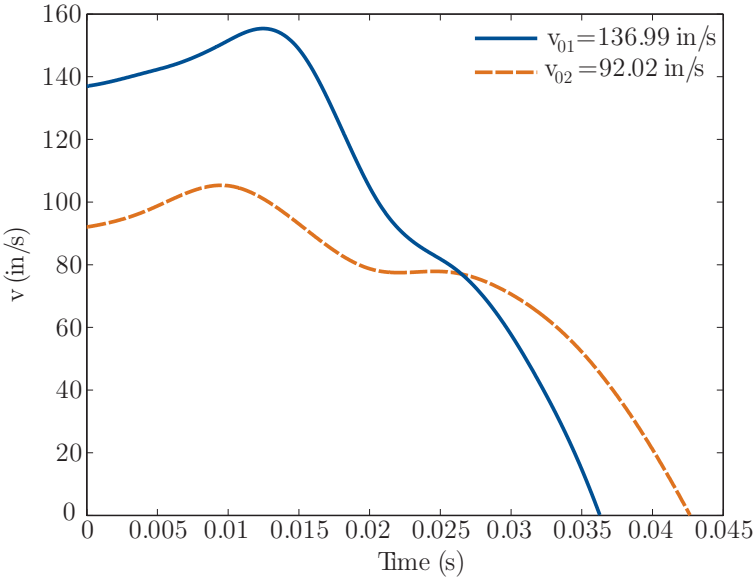

(b) Velocity with time for Subject 2

Figure J.2: The average experimental impact results for Subject 2: (a) Displacement during impact, and (b) Velocity during impact

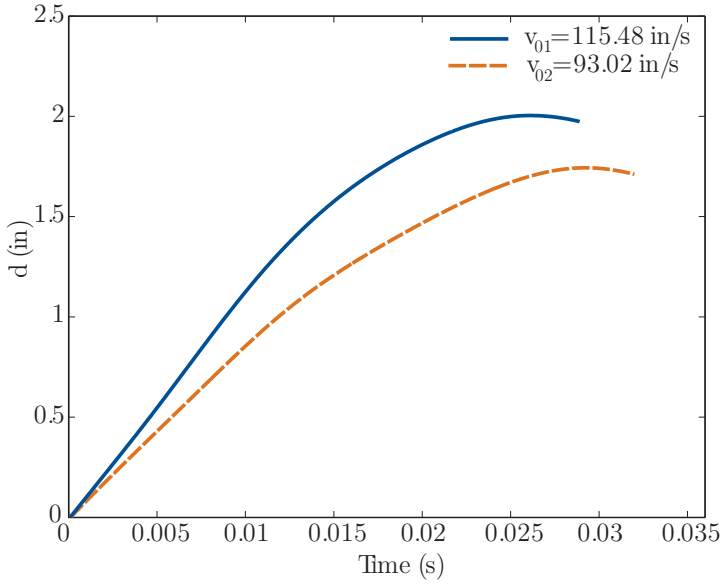

(a) Depth with time for Subject 3

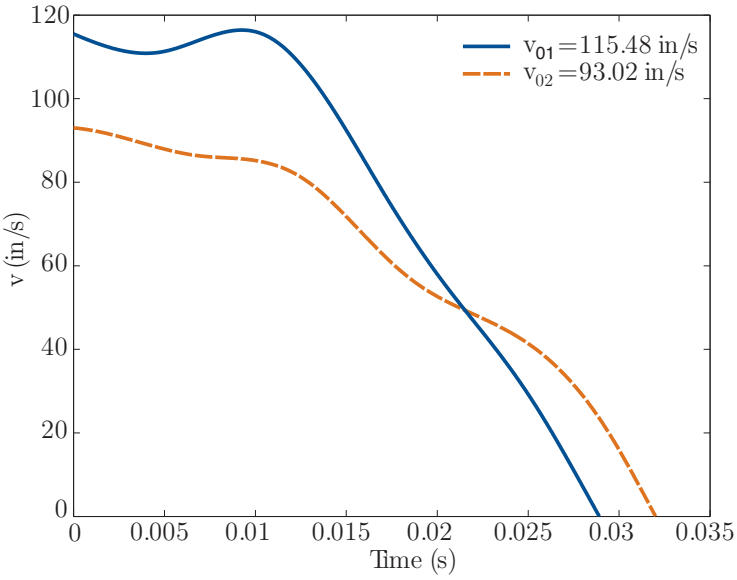

(b) Velocity with time for Subject 3

Figure J.3: The average experimental impact results for Subject 3: (a) Displacement during impact, and (b) Velocity during impact

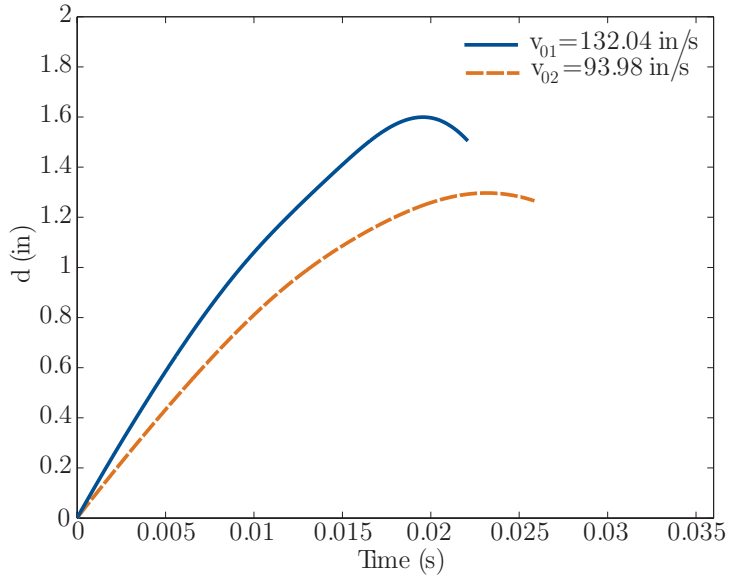

(a) Depth with time for Subject 4

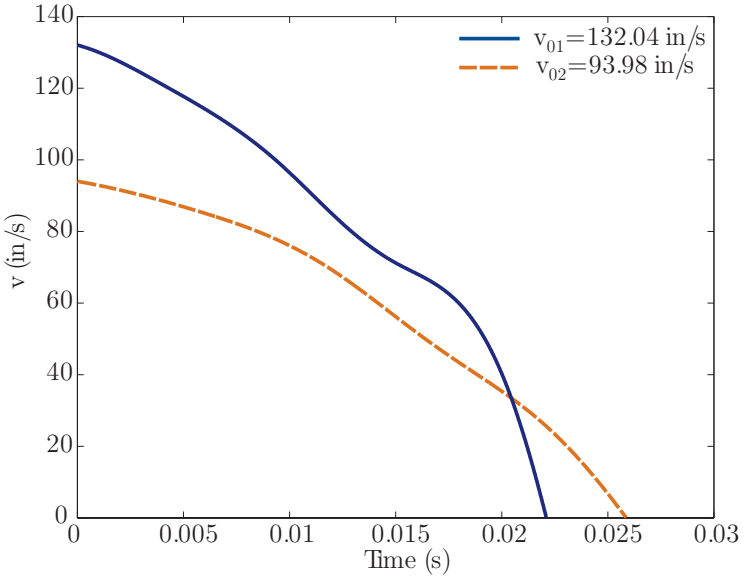

(b) Velocity with time for Subject 4

Figure J.4: The average experimental impact results for Subject 4: (a) Displacement during impact, and (b) Velocity during impact

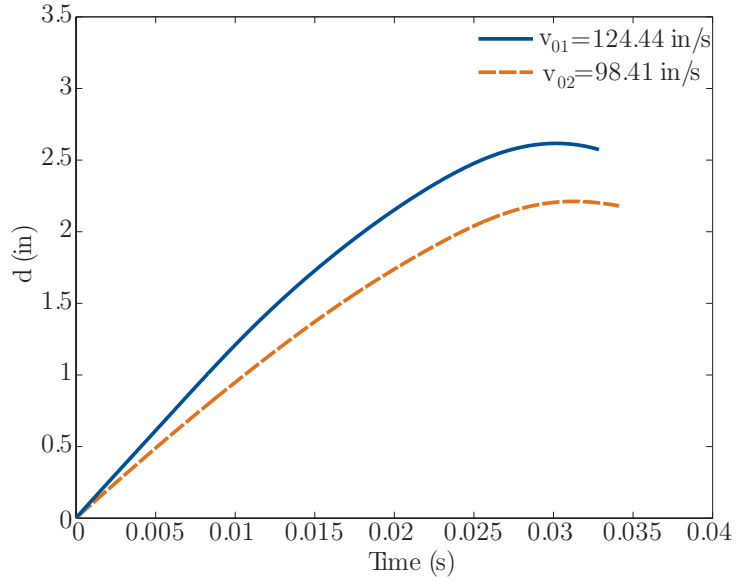

(a) Depth with time for Subject 5

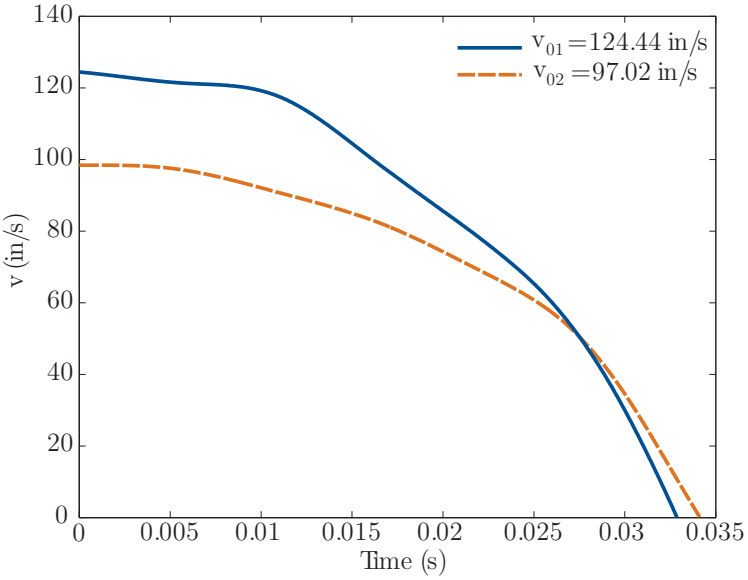

(b) Velocity with time for Subject 5

Figure J.5: The average experimental impact results for Subject 5: (a) Displacement during impact, and (b) Velocity during impact